

TABLE OF CONTENTS

	Page
INTRODUCTION	1
CHAPTER 1 SILICON PHOTONICS IN OPTICAL COMMUNICATION	3
1.1 Thesis Objective	4
1.2 Methodology	5
1.3 Thesis Contributions	6
1.4 Thesis Organization	7
CHAPTER 2 PASSIVE OPTICAL FILTERS: A LITERATURE REVIEW	9
2.1 Microring Resonators for Transceiver Applications.....	10
2.2 Microdisk Resonators for Transceiver Applications	22
2.3 Silicon nitride waveguide based Microring and Microdisk Resonators	25
CHAPTER 3 RING-REFLECTOR FOR TUNABLE LASER APPLICATION	29
3.1 Design Approach	31
3.2 Simulations and Optimization.....	33
3.2.1 Simulation of a channel waveguide	33
3.2.2 Simulation of a Directional Coupler	36
3.2.3 Simulation of a Silicon Nitride Ring Reflector.....	37
3.2.4 Simulation of a Silicon Serially Coupled 3-Ring Reflector: The Vernier Effect	41
3.3 Fabrication, Measurements and Analysis	48
3.3.1 Mask Layout Description.....	48
3.3.2 Fabrication Process Flow for Si ₃ N ₄ structures.....	49
3.3.3 Optical Test Setup.....	50
3.3.4 Measurements and Analysis	52
3.4 Summary	61
CHAPTER 4 RACETRACK RESONATOR FOR THE CHIRPED MODULATED LASER.....	63
4.1 Small 4-port add-drop racetrack resonator	66
4.1.1 Design, Simulation and Optimization.....	66
4.1.2 Fabrication, Measurements and Analysis	74
4.2 Large 4-port add-drop racetrack resonator	78
4.2.1 Design, Simulation and Optimization.....	78
4.2.2 Fabrication, Measurements and Analysis	84
4.3 Summary	87
CONCLUSIONS AND FUTURE WORK.....	89

APPENDIX I Derivation for power equations of racetrack resonator.....	91
APPENDIX II Derivation of 3 rd order ring filter	95
APPENDIX III Derivation of relation between effective refractive index $n(r,\phi)$ and field function (ψ).....	97
APPENDIX IV MATLAB script for computing optical response of ring-resonator	99
APPENDIX V MATLAB script for computing of cut-off thickness	101
BIBLIOGRAPHY	103

LIST OF TABLES

	Page
Table 3.1	Parameters of different RRs (based on Si waveguide) integrated with Y-splitters41
Table 3.2	Attributes obtained for Si waveguide based three different ring reflectors43
Table 3.3	Optimized design parameters for Si waveguide based three different single ring reflectors45
Table 3.4	Performance parameters for the optimized single Si ring reflectors46
Table 3.5	Important attributes illustrating fabricated device performance54
Table 3.6	Cut-off thickness for the waveguide structure59
Table 4.1	Design parameters for two different racetrack-resonators72
Table 4.2	Performance attributes for two different racetrack-resonators74

LIST OF FIGURES

	Page
Figure 1.1	Performance of the top 500 supercomputers in the world3
Figure 1.2	Research cycle.....5
Figure 2.1	Field propagation along a directional coupler. Modes calculated using the waveguide mode solver and the modes are propagated using the eigenmode expansion method.....12
Figure 2.2	Model of a (a) single ring resonator with one waveguide, which forms a ‘notch filter’ and (b) the basic add-drop ring resonator filter13
Figure 2.3	Model of a serially coupled three-ring add-drop filter showing the coupling coefficients and the loss coefficients for each ring18
Figure 2.4	A general schematic of an external cavity semiconductor laser20
Figure 2.5	a) Schematic of the ring with integrated DBR. The DBR is realized by modulating the top half of the ring waveguide. b) SEM image of the fabricated device prior to top cladding deposition21
Figure 3.1	A general schematic of a wavelength tunable laser electromechanically tuned using a MEMS actuator.....29
Figure 3.2	Schematic of the proposed 3-ring reflector filter having racetrack-resonator serially coupled and integrated with two Y-branch splitters showing propagation of the reflected and the transmitted light within the filter.....31
Figure 3.3	(a) Perspective view of Si_3N_4 channel waveguide with insets showing the cross-section waveguide geometry and TE mode distribution; (b) Wavelength dependent effective index (c) Wavelength dependent group index34
Figure 3.4	(a) Perspective view of Si channel waveguide with insets showing the cross-section waveguide geometry and TE mode distribution; (b) Wavelength dependent effective index; (c) Wavelength dependent group index35

Figure 3.5	The effect of waveguide width variation over n_{eff} and n_g at 1550 nm for (a) Silicon nitride waveguide (thickness of 435 nm), (b) Silicon waveguide (thickness of 220 nm).....	35
Figure 3.6	Symmetric and Antisymmetric modes dependence over the coupling gap at 1550 nm for (a) Si_3N_4 waveguide (b) Si waveguide;with insets showing supermodes electric field distribution	36
Figure 3.7	Field coupling coefficient ‘k’ versus coupling gap at 1550 nm for (a) Silicon nitride waveguide having dimensions 435 nm x 435 nm ($L=20 \mu\text{m}$), and (b) Silicon waveguide having dimensions 440 nm x 220 nm ($L=20 \mu\text{m}$).....	36
Figure 3.8	General schematic of a single ring reflector based on Si_3N_4 waveguide with dimensions 435 nm x 435 nm	38
Figure 3.9	Waveguide bend loss versus radius for 435 nm wide Si_3N_4 waveguide (in dB scale)	38
Figure 3.10	Effect of field coupling coefficient κ on the drop port peak intensity of an add-drop ring resonator	39
Figure 3.11	(a) Simulated spectral response of a silicon nitride single ring reflector, (b) zoom in of the resonance peak of the reflection/drop port response.....	40
Figure 3.12	FSRs for three different ring reflectors, each of them showing a common central wavelength around $\sim 1492 \text{ nm}$	42
Figure 3.13	The reflection response of a serially coupled 3-ring reflector in a 2.5D-FDTD showing resonance peak splitting.....	43
Figure 3.14	The effect of the coupling coefficient ‘ κ ’ on the drop port peak intensity of Si waveguide based single ring resonator of radius (a) $3.6 \mu\text{m}$ (b) $4.3 \mu\text{m}$ and (c) $10 \mu\text{m}$	45
Figure 3.15	Reflection spectra obtained from 2.5D-FDTD for three different Si ring reflectors showing their corresponding FSRs	46
Figure 3.16	Reflection spectra for a serially coupled Si 3-ring filter illustrating the Vernier effect and showing the dominant resonant peak without peak splitting	47
Figure 3.17	A generalised process flow for the fabrication of the Si_3N_4 waveguide structures.....	50

Figure 3.18	Optical Test Measurement Setup (1) (a) Single mode input fibre (b) Single mode output fibre (2) Device chip (3) Chip holding stage (4) Chip stage controller (5) Three axis stage controller for (a) input fibre (b) output fibre (6) Polarization rotator (7) Microscope.....	51
Figure 3.19	The through port transmission response for (a) Device 6, (b) Device 8 & (c) Device 9	53
Figure 3.20	Comparison of the through port transmission response for 3 devices	55
Figure 3.21	(a) Theoretical vs Experimental through port response for devices 6, 8 and 9 (b) Zoomed in response of plot (a).....	56
Figure 3.22	SEM image of the (a) fabricated waveguides forming the coupling region and (b) the cross section of the waveguide	57
Figure 3.23	Normalized curve showing theoretical vs experimental response for varying widths (a) Device 6 (435 nm) (b) Device 8 (445 nm) (c) Device 9 (455 nm).....	59
Figure 3.24	The effect on the n_{eff} of the fundamental TE and TM mode for the (a) Fabricated waveguide width (386 μm top x 427 bottom) vs. the varying waveguide thickness and (b) Fabricated waveguide thickness of 453 μm vs. the varying waveguide width	60
Figure 4.1	(a) Electrical signal at the input, and a distorted (b) optical signal at the output, of a DML due to chirp.....	64
Figure 4.2	Change of instantaneous frequency ω_{inst} with time showing blue and red shift.....	65
Figure 4.3	(a) Perspective view of a Si_3N_4 channel waveguide with insets showing the cross-section waveguide geometry and fundamental TE & TM mode distribution; (b) Wavelength dependent effective index for TE mode (c) Wavelength dependent group index for TE mode (d) Wavelength dependent effective index for TM mode (e) Wavelength dependent group index for TM mode	68
Figure 4.4	The fabrication tolerance showing the change in the n_{eff} of fundamental TE and TM mode at 1550 nm due to (a) variation in the width (fixed thickness at 400 nm) (b) variation in the thickness (fixed width at 400 nm).....	68
Figure 4.5	Field coupling coefficient ' κ ' vs gap, $\lambda=1550$ nm, coupler length $L=5$ μm , $L=10$ μm , $L=15$ μm and $L=20$ μm , 400 nm x 400 nm	

	waveguide, calculated using the waveguide mode solver with a 10 nm mesh size	69
Figure 4.6	The n_{eff} of symmetric and antisymmetric modes versus the coupling gap, $\lambda=1550$ nm, 400 nm x 400 nm Si ₃ N ₄ waveguide.	70
Figure 4.7	Waveguide bend loss vs. radius for 400 nm wide SiN waveguide (in dB scale), bend angle of 90°	71
Figure 4.8	The schematic design of two different racetrack resonators (a) Type A, (b) Type B	72
Figure 4.9	Simulated optical response for type A racetrack-resonator.....	73
Figure 4.10	Simulated optical response for type B racetrack-resonator.....	73
Figure 4.11	The intensity profile of the light propagating inside the racetrack resonator obtained using 2.5D-FDTD simulations in Lumerical MODE	74
Figure 4.12	Transmission spectra for a small ring filter, waveguide 400 nm x 400 nm.....	76
Figure 4.13	SEM image of (a) the fabricated RR and (b) the coupling region of RR showing variation in the gap and the waveguide widths.	77
Figure 4.14	Field coupling coefficient ' κ ' vs gap, $\lambda=1550$ nm, coupler length L=10 μm , L=15 μm , L=20 μm , L=25, L=30 μm and L=35 μm , 435 nm x 435 nm waveguide, calculated using the waveguide mode solver with a 10 nm mesh size.	79
Figure 4.15	The general schematic design of a large racetrack resonator	80
Figure 4.16	Simulated optical spectra of a large racetrack resonator showing transmission at the drop port and the through port (in dB)	81
Figure 4.17	A general schematic of the circuit simulation setup in the Lumerical Interconnect showing 4 different configurations.....	82
Figure 4.18	Plot showing ER (in dB scale) vs. detuning ($\Delta\lambda$) for configuration (3)	83
Figure 4.19	Graph showing pulse amplitude from the laser (red line) and the comparison of pulse amplitudes after the propagation through ring filter for lower ER (blue dashed line) and higher ER (black dashed line) obtained.....	83

Figure 4.20 Power spectrum as a function of frequency (THz) showing adiabatic chirp..... 84

Figure 4.21 Measured spectra showing the transmission at the through and the drop port for a large racetrack resonator 85

Figure 4.22 SEM image of a directional coupler of a fabricated large RR 86

Figure 4.23 Normalized transmission spectra (in dB) showing the simulated and the measured through port response..... 86

LIST OF ABBREVIATIONS AND ACRONYMS

2.5D	2.5 dimensional
2D	Two dimensional
3D	Three dimensional
BOX	Buried oxide
CMC	Certified management consultant
CML	Chirp managed laser
CMOS	Complementary metal-oxide semiconductor
CMT	Coupled mode theory
DBR	Distributed Bragg reflector
DC	Directional coupler
DCM	Dispersion-compensation module
DML	Directly modulated laser
DRIE	Dry-reactive ion-etching
DWDM	Dense wavelength division multiplexing
ECL	External cavity laser
ECR-CVD	Electron cyclotron resonance plasma enhanced chemical vapor deposition
EM	Electro-magnetic
EME	Eigen mode expansion
EML	Externally modulated lasers
ER	Extinction ratio
F	Fineese

FDE	Finite difference element
FDTD	Finite difference time domain
FP	Fabrey-Perot
FSR	Free spectral range
FWHM	Full width at half maximum
GaInAsP	Gallium indium arsenic phosphide
Gbps	Giga bits per second
GHz	Giga Hertz
HMDS	Hexamethyldisilazane
ICP	Inductively coupled plasma
IME	Institute of microelectronics
InP	Indium phosphide
INRS	National institute of scientific research
IR	Infra-red
ITU	International telecommunication union
LiNbO ₃	Lithium niobate
LPCVD	Low pressure chemical vapor deposition
LSCVD	Liquid source chemical vapor deposition
MDM	Mode division multiplexing
MEMS	Micro-electro-mechanical-systems
MRR	Micro ring-resonator
MZI	Mach-Zhender interferometer
NGPON2	Next generation passive optical network stage 2

OSA	Optical spectrum analyser
OSR	Optical spectrum reshaper
PDK	Process design kit
PECVD	Plasma enhanced chemical vapor deposition
PMD	Physical media dependent
PMMA	Polymethyl methacrylate
PON	Passive optical network
RIE	Reactive ion etching
RR	Racetrack resonator
RR	Ring-resonator
SHREC	Silicon photonic hybrid ring-filter external cavity
Si	Silicon
Si ₃ N ₄	Silicon nitride
SiN	Silicon nitride
SiO ₂	Silicon dioxide
SiON	Silicon oxynitride
SOI	Silicon-on-insulator
TE	Transverse electric
TM	Transverse magnetic
TWDM	Time and wavelength division multiplexing
TWR	Travelling wave resonators
UQAM	Université de Québec a Montréal

varFDTD	Variational FDTD
WDM	Wavelength division multiplexing
WGM	Whispering gallery modes

LIST OF SYMBOLS AND UNITS OF MEASUREMENT

kW	Kilowatt
Gb/s	Gigabit per second
Km	Kilometers
GHz	Giga Hertz
THz	Tera Hertz
Λ	Grating periods
λ_r	Resonant wavelength
R	Ring radius
m	Integer number
n_{eff}	Effective refractive index of the waveguide
n_g	Group index of the waveguide
n	effective index of material
C	Coupling coefficient
κ	Field coupling coefficient
π	$\pi=3.14$
n_1	effective refractive index of symmetric mode
n_2	effective refractive index of antisymmetric mode
Δn	difference between symmetric and antisymmetric mode
λ	Wavelength
β_1	Propagation constant of symmetric mode
β_2	Propagation constant of antisymmetric mode
L	Length of directional coupler

P_o	Input optical power
P_{cross}	Power coupled across the directional coupler
t	Transmission coefficient
P_{through}	Power remaining in through waveguide
L_x	Cross-over length
L_c	Coupling length
g	Gap
E_{t1}	Through port waveguide mode amplitude
E_{i2}	Drop port waveguide mode amplitude
α	Loss coefficient of the ring
$ t $	Coupling losses of the ring
ϕ_t	Phase of the coupler
θ	Phase of the ring
P_{t1}	Modal power coming out of the through waveguide
P_{i2}	Modal power coming out of the drop waveguide
P_{i2}	Circulating power inside the ring
ϕ	Phase difference variation in-between t and κ in both couplers of ring resonator
$\Delta\lambda$	Distance between the resonance peaks or FSR
$2\delta\lambda$	3-dB bandwidth
$E_{\text{IN}}(z)$	Input node
$E_{\text{T}}(Z)$	Through port node
$E_{\text{D}}(Z)$	Drop port node

H	Network function relating an input to an output port
T_i	Gain (or transmittance) of the i-th forward path from an input to an output port.
n	Total number of ports.
Δ_i	Determinant
Q	Quality factor
λ_0	Central resonant wavelength
dB	Decibel
mW	Miliwatt
°C	Degree celcius
mm	Mili meters
nm	Nano meters
μm	Micro meter
cm	Centi meter
dBm	Decibel-milliwatts
dB/cm	Decibels per centimetre
dB/m	Decibels per meter
m	Meters
Q_c	Quality factor of the coupling between the microdisk and bus waveguide.
$\chi^{(3)}$	Third order non-linear susceptibility
pm	Picometer
ω_{inst}	Instantaneous frequency
I_{th}	Threshold current

Symbols for Cascaded Ring Reflector

- L₁ Optical path length of racetrack-resonator 1
- L₂ Optical path length of racetrack-resonator 2
- L₃ Optical path length of racetrack-resonator 3
- C₁ Coupling region formed by bus waveguide and racetrack 1
- C₂ Coupling region formed by racetrack 1 and 2
- C₃ Coupling region formed by racetrack 2 and 3
- C₄ Coupling region formed by bus waveguide and racetrack 4
- FSR_{extended} Extended FSR obtained on cascading racetrack resonators
- m₁ Resonant number and co-prime integer of ring 1
- m₂ Resonant number and co-prime integer of ring 2
- m₃ Resonant number and co-prime integer of ring 3

INTRODUCTION

With the increasing demand for high data transfer rates, there is a need for high performance networks that can maximise these transfer rates. Various optical components are being used to develop wavelength selective mechanisms for lasers and add-drop multiplexers in dense-wavelength-division-multiplexing (DWDM) optical communication systems. DWDM optical access networks allow the same spectral efficiency in the last mile as found in the core networks (Yoffe, Nguyen, Heanue, & Pezeshki, 2012). In order to achieve such high data transfer systems, the key technology is to implement tunable transceivers including compact, cost-effective and efficient tunable lasers and optical filters. These efficient and compact devices can come to a reality by using optical filters such as microring resonators and microdisk resonators which are already showing an unprecedented reduction in the footprint of optical devices.(Meindl, 2003)

As advancements in the microelectronic industry increases rapidly, complementary-metal-oxide-semiconductor (CMOS) compatible photonics tends to overpower the electronic communication system, since, the data transmission via optical fibres and optical waveguides system enhances the transmission range and the bandwidth of signals. The benefits of signal transmission through an optical waveguide are low power consumption, durability and very low transmission losses in comparison to the traditional electrical transmission lines. With silicon based integrated photonics, the bandwidths of orders of magnitude larger than the electronic networks are achievable. Wavelength-division-multiplexing (WDM) enables a single waveguide to carry multiple data streams. The CMOS compatible photonics allows to create complex optical devices at the chip scale. Ring-resonators are the prime examples of compact and high Q-factor filters being widely used in tunable lasers. With this vision, we present ring-resonator passive optical filters in Chapter 3 to be used as the reflector filters in the external cavity lasers (ECLs). These have a wide free spectral range (FSR) so as to cover the entire spectrum of the gain chip, thus, finding its utility in tunable laser applications.

The International Telecommunication Union (ITU) requirements for a passive optical network (PON) systems with a nominal aggregate capacity of 40 Gb/s in the downstream direction and 10 Gb/s in the upstream direction is referred to as the next generation passive optical network stage 2 (NGPON2). The ITU-T G.989.2 recommendation describes a network supporting multiple services with bandwidth requirements running at a downstream rate of 4 x 10 Gb/s. This recommendation based on time and wavelength division multiplexing (TWDM) was proposed to address the increasing bandwidth demand (Kazovsky, Shaw, Gutierrez, Cheng, & Wong, 2007). This advancement in the technology compels the development of novel 10 Gb/s-transmitters which necessitate innovative but also cost-effective and compact solutions providing long transmission range (>60 Km) and high extinction ratio. Chirp managed laser (CML) are systems using an external filter in front of a directly modulated laser (DML) to attenuate the inherent chirp of a laser by aligning the laser wavelength to the transmission edge of the filter. This allows to significantly increase the extinction ratio and the reach of the signals by attenuating the data bits '0' and allowing only data bits '1'. Thus, in chapter 4, we discuss and demonstrate a Si₃N₄ waveguide based compact passive ring resonator, which can be used as an external filter aiding to increase the extinction ratio of tunable lasers. We present a cost-effective method to develop such a filter by using the traditional CMOS compatible fabrication process and its compactness allows the smaller footprint on the chip-scale integration as compared to other bulky etalon filters.

CHAPTER 1

SILICON PHOTONICS IN OPTICAL COMMUNICATIONS

In accordance with the more than Moore principle, several functionalities have been added at the chip scale, making them applicable in the diverse fields. The enormous amount of data storing computers and their associated components deployed within data centres consume large amount of electrical energy thereby increasing the operation cost. The future of computer technology relies on ultra-fast data transfer rates between and within the microchips (Meindl, 2003). The speed of the top 500 supercomputers has increased exponentially during the last two decades, as shown in Figure 1.1, which is soon expected to reach the Exascale (10^{18} FLOPs) by year 2020. This increase in the speed is giving rise to huge bandwidth demands, which according to leading companies such as IBM and Intel, can only be met by investing

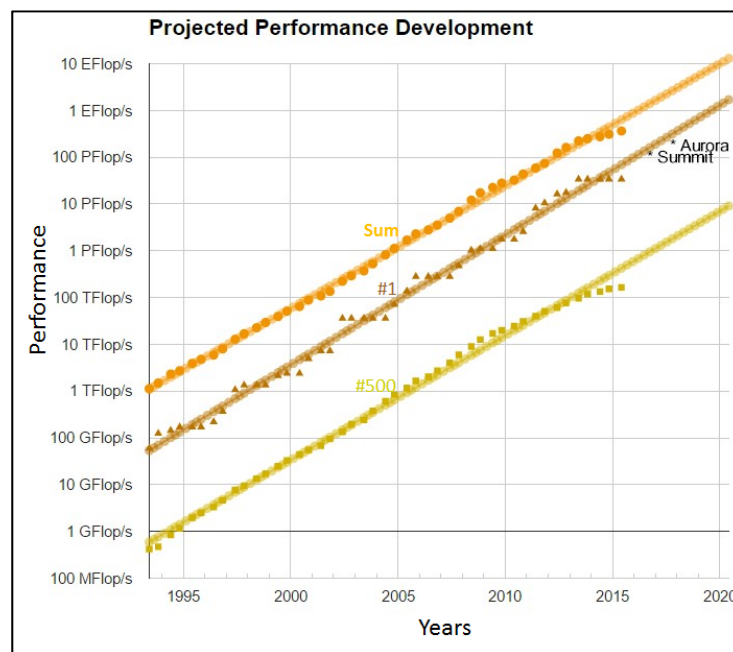


Figure 1.1 Performance of the top 500 supercomputers in the world
Taken from (<https://www.nextplatform.com/2015/07/13/top-500-supercomputer-list-reflects-shifting-state-of-global-hpc-trends/>)

heavily in the field of silicon photonics to provide much faster data transfer rates. Thus, silicon photonics helps in keeping on track with Moore's Law.

A data centre with many servers incurs high operational costs and power consumption due to increase of optical components on a small chip size. Thus, there is a tremendous need for developing highly efficient miniaturized optical components that could bring down the cost of high speed optical interconnects to 1\$/Gbps. Resolving these challenges need the development of compact and efficient tunable transceivers which can be used in dense wavelength division multiplexing (DWDM) systems. These DWDM optical communication systems provides high performance networks which are able to meet with the high data transfer rates and provide the same spectral efficiency till the last mile (end users) as it is found in the core networks. High refractive index contrast waveguides, which can be implemented with the CMOS fabrication technology, have allowed the development of photonic circuitry using electronic fabrication facilities. This has made the silicon nitride/silicon photonics one of the most promising optical integration platforms over the last few years leading to the possibility of developing highly efficient miniaturized optical components and tunable lasers that could bring down the cost of optical interconnects.

1.1 Thesis Objective

The main objective of this thesis is to design, fabricate and characterize the silicon nitride (Si_3N_4) waveguide based integrated optical filter components with potential application for wavelength selective devices. A 3rd order Si_3N_4 ring filter in a reflector configuration will be designed to have a wide free spectral range (FSR), which can be used to develop a wavelength channel selection mechanism in a tunable external cavity laser (ECL). This small ring reflector will provide an optical feedback mechanism and allow the wavelength tuning of a laser. Also, a Si_3N_4 ring filter with an aim of developing an optical eye reshaper, will be designed having a large extinction ratio (ER) to be potentially used as a tunable transmitter in the NG-PON2 systems. This external ring filter having a FSR of 100 GHz, will be used in future along with the tunable laser to implement a CML. With this view, the optical components such as micro-

ring/racetrack resonators will be designed and optimized leading to the innovative transceivers application.

1.2 Methodology

The devices demonstrated in this thesis were fabricated using a CMOS compatible process. The research methodology is illustrated in Figure 1.2. The research methodology cycle begins with an idea emerging through the literature review, brain storming and workshops/conferences. The design model is based on the standard 8" Si wafer covered with a 4 μm thick oxide layer. Later, simulations and optimization of basic building blocks such as directional couplers, Y-splitters, and waveguide bends, are done using analytical models, further leading to the design optimization of the final devices such as racetrack resonators with

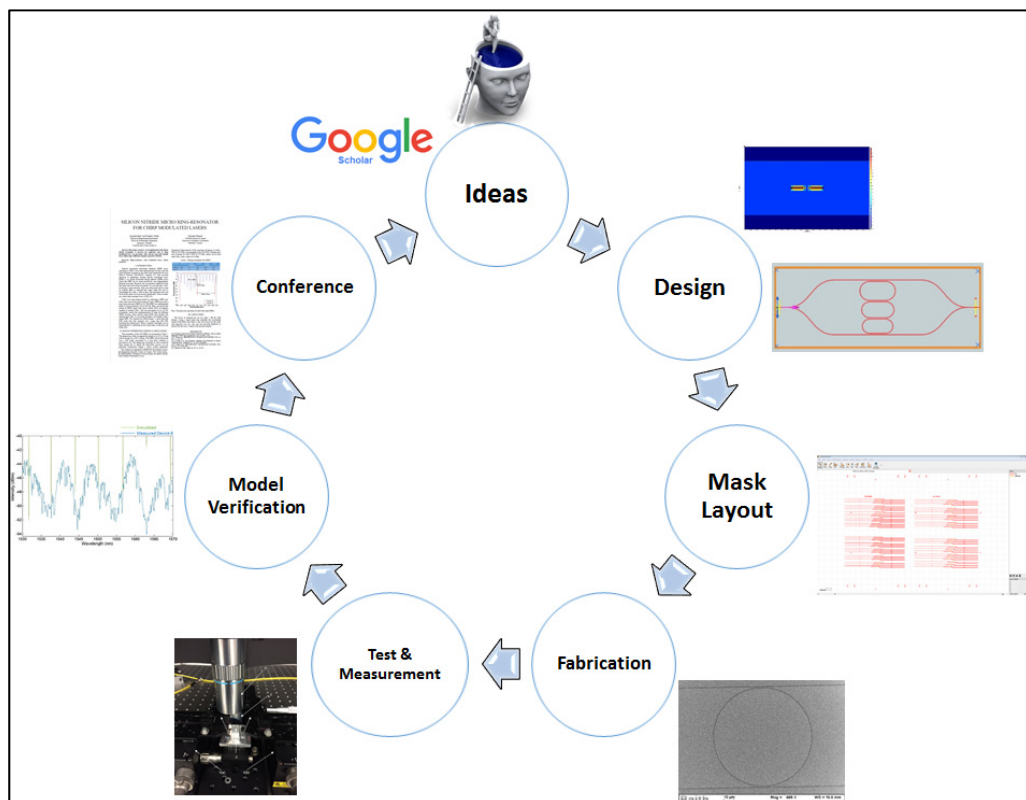


Figure 1.2 Research cycle

the aid of the numerical tools such as Eigen-mode expansion (EME) and the finite difference time domain (FDTD) solvers. Afterwards, the photolithographic mask used for fabrication is designed. In order to build our devices, we have used the fab facilities of IME*Singapore accessed via CMC Microsystems (strictly following the PDK) and several other lab facilities of universities across Montreal, Canada such as INRS, Polytechnic and McGill. The recipes associated with the microfabrication steps such as dry reactive ion-etching (DRIE), e-beam lithography, low-pressure chemical vapour deposition (LPCVD) and plasma enhanced chemical vapour deposition (PECVD) were modified to obtain an optimized process flow in collaboration with the fellow researchers and the clean room personals. Through the efficient mix and match of the lithographic techniques, a large range of dimensional issues were addressed as and when required. After receiving the fabricated chips from the fabs, optical testing and measurements are performed in the UQAM lab facilities using an advanced alignment setup to investigate the propagation and insertion losses, followed by the transmitted/reflected spectrum analysis using an optical spectrum analyser. After this, the data processing and analysis is done by comparing the simulated and the experimental results, leading to the model verification and improvement. Eventually the results obtained are presented in conference presentation. The above methodology cycle was repeated in order to build each device and some fab-variations were carried out from time-to-time in order to resolve the structural discrepancies and to solve the challenges arising while testing of the optical devices.

1.3 Thesis Contributions

In this thesis, we present ring filters in different configurations, contributing to the field of silicon/silicon nitride photonics as follows:

- 1) Racetrack resonator filters for CML: We design and demonstrate a Si_3N_4 racetrack resonator, with a FSR in close proximity to the ITU channel grid, to be used as an external filter along with a tunable laser to implement chirp managed lasers (CML).
- 2) Ring reflector filter for tunable laser: We designed a 3rd order ring filter in a reflector configuration on a Si platform giving a FSR wide enough to cover the entire C- or L-

band. Also, we demonstrate a Si_3N_4 ring reflector, providing a novel approach towards future designing of a high order ring reflector (using Si_3N_4 waveguide), for the tunable laser application.

1.4 Thesis Organization

This thesis is organized as follows:

In Chapter 2, the state-of-the-art is presented for the silicon (Si)/silicon nitride (SiN) microring resonator and micro-disk resonator optical filters depicting its advantages over other passive filters with applications in optical transceivers. In Chapter 3, we present a novel silicon ring reflector, composed of three racetrack resonators (RRs) coupled in series, in order to have a wide FSR achieved by the Vernier effect. Also, a single ring reflector based on a silicon nitride waveguide is modeled and demonstrated. The design and modelling of a single and a cascaded ring-reflector is carried out using an analytical approach and the obtained simulated results investigate the important parameters such as the FSR, quality factor, bus-resonator coupling, ER and transverse modes. Moreover, the transmission and the reflection properties obtained from the experimental results for a silicon nitride waveguide based single ring reflector validates the characteristics mentioned above and also the structural discrepancy between the fabricated and simulated designs. Chapter 4 demonstrates two designs of the SiN waveguide-based racetrack resonators, to be used in CML. Design 1 is a 4-port add-drop racetrack resonator having an optical path length corresponding to a FSR of 718.75 GHz, whereas, design 2 comprises a large optical path length for a specific application in the next generation passive optical networks (NGPON2) systems. An analytical model, starting from the directional coupler and leading to the design approach of a fully optimized 4-port add-drop ring filter is presented. Important characteristics of RRs such as propagating modes, quality factor, ER, FSR and bus-resonator coupling are investigated in experimental and numerical simulations.

CHAPTER 2

PASSIVE OPTICAL FILTERS: A LITERATURE REVIEW

Complex photonic integrated circuits are usually constructed from various fundamental photonic building blocks or components. Fibre Bragg gratings were used early in wavelength filtering mechanisms because of their flexible filtering capability, low insertion and reflection losses and low cost. Fibre Bragg gratings were first presented by (Kawasaki, Hill, Johnson, & Fujii, 1978). Later Lam and Garside in 1981 showed that the refractive index modification was related to the square of the Argon laser intensity (Lam & Garside, 1981) in the experiments performed by (Kawasaki et al., 1978). The integration of waveguide Bragg gratings in the silicon-on-insulator (SOI) platform (G. Jiang et al., 2011; X. Wang et al., 2012) has been of great interest and its compatibility with the CMOS technology (X. Wang et al., 2012) has made it even more economically viable providing an ease of fabrication. Thus, they have found numerous applications in the area of optical communication (Vargas & Vazquez, 2014), such as WDM filters (Painchaud, Paquet, & Guy, 2007), single channel-extraction filter for dense wavelength division multiplexing (DWDM) applications (Alonso-Ramos et al., 2014), dispersion engineering (Cliche et al., 2007), lasers (Rochette, Guy, LaRoche, Lauzon, & Trepanier, 1999), optical signal processing (Wang & Yao, 2013), wavelength selection mechanism and dispersion compensation (Giuntoni et al., 2010) and bio-sensing system (Jugessur, Dou, Aitchison, De La Rue, & Gnan, 2009). The issues with using Bragg gratings is that they require a large on-chip area and need an optical circulator to access the reflected Bragg wavelength signal which adds to the loss in power intensity of the signal. Depending upon the application, the number of grating periods (Λ) is selected to have an efficient optical filter. Each grating period has a length of hundreds of nanometres and depending upon application, the number of grating periods are chosen so as to have an optimum Bragg wavelength and the band rejection. This results in a large device footprint in the range of millimetres. When these large size filters have to be used in an active state such as in lasers and phase-shifted modulators, they need to be thermally or electrically tuned thereby increasing power consumption (as the whole grating or corrugated area needs to be actuated)

and fabrication cost. Therefore, with an increasing demand for optical filters in telecommunication applications, there is a tremendous need to make compact and economically viable optical devices in addition to maintaining the high quality factor and efficient wavelength filtering mechanism. This is provided by micro-ring resonator (MRR)/microdisk resonators which show a tremendous reduction in the footprint, better flexibility, less losses and minimal cost. Moreover, the wavelength tuning mechanism for the wavelength selection process will be electrostatic actuation which needs low power consumption. Thus, in this chapter, an extensive review of micro ring-resonator and micro-disk resonator filters is presented illustrating its applicability and leading edge over other filters.

2.1 Microring Resonators for Transceiver Applications

Passive silicon waveguide structures have shown an unprecedented reduction in the footprint of wavelength selective devices where microring resonator is a prime and interesting example of this. A microring is a circular waveguide excited by a bus waveguide where a fraction of input power from the bus waveguide couples into the ring. The most common coupling mechanism used is co-directional evanescent coupling between the ring and an adjacent bus waveguide. Resonance occurs within the ring cavity when the optical path length of the resonator is exactly a whole number of the wavelengths i.e. for the light whose phase change after each full trip around the ring is an integer multiple of 2π , which is of course the condition for the light in the ring to be in-phase with the incoming light from the bus and causes constructive interference. Light which does not meet this resonant condition is transmitted through the bus waveguide. The expression for the resonant wavelength is very similar to a Fabry-Perot (FP) cavity and is given by (Bogaerts et al., 2012):

$$\lambda_r = \frac{2\pi R n_{eff}}{m} \quad (2.1)$$

where, 'R' is the ring radius, 'm' is an integer and n_{eff} is the effective refractive index of the waveguide. In order to achieve an effective ring-resonator, the design of a proper coupling

region is required. In the case of a racetrack resonator, directional couplers (DC) should be studied and designed properly. A DC is the most common device to split and to combine light in a photonic system. A DC consists of two parallel waveguides where the field coupling coefficient ' κ ' is controlled by the coupler gap i.e. the spacing between the two waveguides and the coupler length. At first, the coupling coefficient ' C ' is determined using the supermodes analysis method, based on the numerical calculation of the effective indices n_1 and n_2 , of the first two eigenmodes of the coupled waveguides. These two modes are known as symmetric and antisymmetric modes, also generally known as supermodes. The Eigen mode expansion method (EME) is another method which is more accurate than the traditional coupled mode theory (CMT) method (Yariv, 2000) especially for the high-index contrast waveguides where the coupling coefficient is found using the perturbation methods. From these two supermodes, the ' C ' can be written as (Chrostowski & Hochberg, 2015):

$$C = \frac{\pi \Delta n}{\lambda} \quad (2.2)$$

where Δn is the difference between the effective indices, $n_1 - n_2$, also known as birefringence. The two modes propagating inside the waveguides have different propagation constants as given in (Chrostowski & Hochberg, 2015, p. 93):

$$\beta_1 = \frac{2\pi n_1}{\lambda} \quad (2.3)$$

$$\beta_2 = \frac{2\pi n_2}{\lambda} \quad (2.4)$$

Then a fraction of the power coupled from one waveguide to another can be expressed as shown in (Chrostowski & Hochberg, 2015, p. 92):

$$\kappa^2 = \frac{P_{cross}}{P_0} = \text{Sin}^2(C.L) \quad (2.5)$$

where P_0 is the input optical power, P_{cross} is the power coupled across the directional coupler, L is the length of the coupler and C is the coupling coefficient. Then the remaining fractional

power in the original ‘through’ waveguide (assuming a lossless coupler i.e. $\kappa^2 + t^2 = 1$) is given by (Chrostowski & Hochberg, 2015, p. 92):

$$t^2 = \frac{P_{through}}{P_0} = \text{Cos}^2(C.L) \quad (2.6)$$

As the modes propagate, the field intensity oscillates between two waveguides as shown in Figure 2.1, where if the two modes are in phase then the power is localized in the first waveguide. After a π phase shift difference between the modes, the power becomes localized in the second waveguide which occurs after a distance known as the cross-over length ‘ L_x ’ which is shown in (Chrostowski & Hochberg, 2015, p. 93):

$$\begin{aligned} \beta_1 L_x - \beta_2 L_x &= \pi \\ L_x \left[\frac{2\pi n_1}{\lambda} - \frac{2\pi n_2}{\lambda} \right] &= \pi \\ L_x &= \frac{\lambda}{2\Delta n} \end{aligned} \quad (2.7)$$

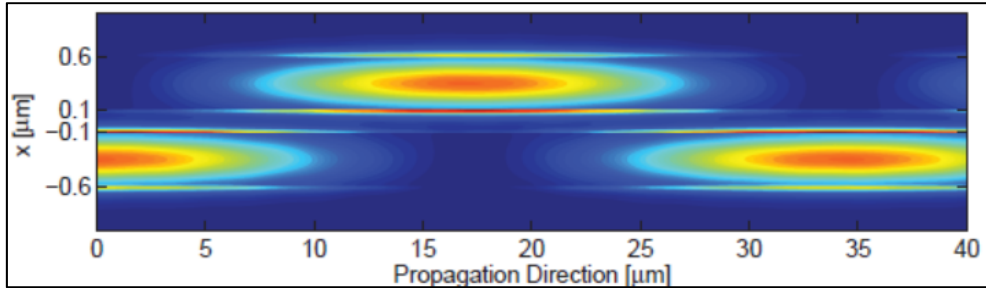


Figure 2.1 Field propagation along a directional coupler. Modes calculated using the waveguide mode solver and the modes are propagated using the eigenmode
Taken from Chrostowski & Hochberg (2015, p. 95)

The C has a dependence on the distance between the waveguide ‘ g ’ which follows an exponential behaviour given by (Chrostowski & Hochberg, 2015, p. 94):

$$C = B. e^{-A.g} \quad (2.8)$$

where A and B are dependent on the geometry of the coupler, optical wavelength, etc. Thus the field coupling coefficient ‘ κ ’ can be found for a directional coupler of any length or a gap using equation (2.5) as shown in (Chrostowski & Hochberg, 2015, p. 95):

$$\kappa = \left[\frac{P_{Coupled}}{P_0} \right]^{1/2} = \left| \sin \left(\frac{\pi \Delta n}{\lambda} \cdot L \right) \right| = \left| \sin \left(\frac{\pi}{2} \cdot \frac{z}{L_x} \right) \right| \quad (2.9)$$

Thus, deciding an optimum value of field coupling coefficient ‘ κ ’ helps in determining the important parameters such as gap and coupling length for a directional coupler which is key in designing complex passive filters. Two types of ring filter configurations are shown in Figure 2.2, where the basic coupling model of a notch filter (Figure. 2.2(a)) and 4-port add-drop filter (Figure. 2.2(b)) is presented.

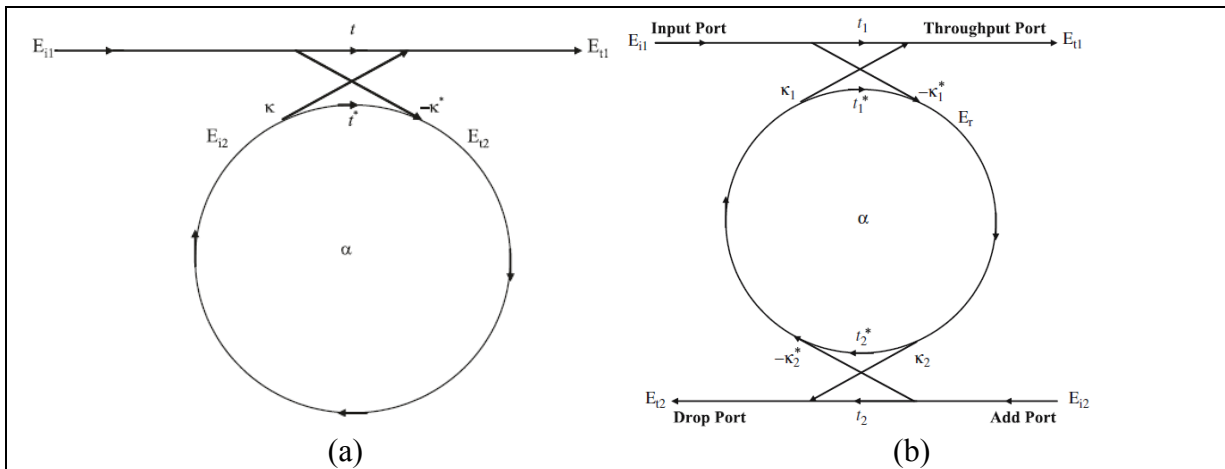


Figure 2.2 Model of a (a) single ring resonator with one waveguide, which forms a ‘notch filter’ and (b) the basic add-drop ring resonator filter
Taken from Rabus (2007, p. 4-7)

For a notch type filter, the coupling between the bus waveguide and the ring is lossless and the various kinds of losses occurring along the propagation of the light in the ring resonator filter are incorporated in the attenuation constant. Then the interaction between the bus-waveguide and the ring can be described by the matrix relation given by (Rabus, 2007):

$$\begin{pmatrix} E_{t1} \\ E_{t2} \end{pmatrix} = \begin{pmatrix} t & k \\ -k^* & t^* \end{pmatrix} \begin{pmatrix} E_{i1} \\ E_{i2} \end{pmatrix} \quad (2.10)$$

The complex mode amplitudes ‘ E ’ are normalized such that their squared magnitude corresponds to the modal power and the t and k are transmission and field coupling coefficients, respectively. The $*$ denotes the complex conjugate of t and k . The matrix is symmetric since the device under consideration is reciprocal. Therefore,

$$|k^2| + |t^2| = 1 \quad (2.11)$$

and to further simplify the model, E_{i1} is chosen to be equal to 1. Then the round trip mode amplitude is given by (Rabus, 2007, p. 4):

$$E_{i2} = \alpha \cdot e^{j\theta} E_{t2} \quad (2.12)$$

where, α is the loss coefficient of the ring and $\theta = \omega L/c$ (for further explanation, please refer to Appendix I). From (2.10) and (2.12), we obtain the other propagating mode amplitudes which are presented in (Rabus, 2007, p. 5):

$$E_{t1} = \frac{-\alpha + t \cdot e^{-j\theta}}{-\alpha t^* + e^{-j\theta}} \quad (2.13)$$

$$E_{i2} = \frac{-\alpha k^*}{-\alpha t^* + e^{-j\theta}} \quad (2.14)$$

$$E_{t2} = \frac{-k^*}{1 - \alpha t^* e^{j\theta}} \quad (2.15)$$

The corresponding circulating modal power inside the ring is then obtained by squaring the complex mode amplitudes (i.e. $P_{t1} = |E_{t1}|^2$ and $P_{i2} = |E_{i2}|^2$), which are derived in Appendix I. When the loss coefficient $\alpha = |t|$, then the internal losses are equal to the coupling losses and the transmitted power becomes zero. This condition is known as critical coupling which is caused by destructive interference. When, $\alpha > |t|$ then the ring filter is said to be over-coupled and when $\alpha < |t|$, it is considered to be under-coupled.

Now, when another bus-waveguide is included in the design to make it a 4-port add-drop filter (as shown in Fig. 2.2(b)), then the mode amplitude at the through port is given by (Rabus, 2007, p. 6):

$$E_{t1} = \frac{t_1 - t_2^* \alpha e^{j\theta}}{1 - t_1^* t_2^* \alpha e^{j\theta}} \quad (2.16)$$

Now the mode amplitude has to pass through the second coupler as can be seen from the Fig. 2.2(b) so as to become the new dropped mode amplitude E_{t2} . The relation for the dropped mode amplitude in the second waveguide is given by relation presented in (Rabus, 2007, p. 6):

$$E_{t2} = \frac{-k_1^* k_2 \alpha_{1/2} e^{j\theta_{1/2}}}{1 - t_1^* t_2^* \alpha e^{j\theta}} \quad (2.17)$$

where, $\alpha_{1/2}$ and $\theta_{1/2}$ are the half round trip loss and the phase given by $\alpha = \alpha_{1/2}^2$ and $\theta = 2\theta_{1/2}$. At the resonance, the output power at the drop port is then given by the square of complex mode amplitude $|E_{t2}|^2$ (shown in Appendix I). In the case of racetrack resonators, the coupling distance is approximately the length of the coupling sections. At a point where the curved and the straight waveguides combine, the mode changes adiabatically between the radial mode of the curved waveguide and the normal mode in the straight waveguide. Thus, in order to keep the total optical path length constant, the radius of the curved waveguides should be reduced if the waveguides are extended. It is important to consider the variation of the phase difference φ which occurs in the coupling region in both couplers between t and κ . The phase difference is length dependent and affects the output characteristics, not only in the magnitude but also in the resonant conditions. This phase difference can be introduced in equations 2.16 and 2.17 using the method described in (Lee et al., 2004) and the complete relation for mode amplitudes at the through port is then modified to (Rabus, 2007, p. 17):

$$E_{t1} = \frac{t_1 e^{j\varphi t_1} - t_2^* \alpha_{1/2}^2 e^{j\theta} (t_1 t_1^* e^{j2\varphi t_1} - \kappa_1 \kappa_1^* e^{-j2\varphi \kappa_2}) e^{j\varphi t_2}}{1 - t_1^* t_2^* \alpha_{1/2}^2 e^{j\theta} e^{j\varphi t_1} e^{j\varphi t_2}} \quad (2.18)$$

and at the drop port it changes to (Rabus, 2007, p. 17):

$$E_{t2} = \frac{-\kappa_1^* \kappa_2 \alpha_{1/2} e^{j\theta_{1/2}} e^{-j\varphi \kappa_1} e^{-j\varphi \kappa_2}}{1 - t_1^* t_2^* \alpha e^{j\theta} e^{j\varphi t_1} e^{j\varphi t_2}} \quad (2.19)$$

The resonant conditions for a racetrack resonator $(\theta + \varphi t_1 + \varphi t_2) = 2\pi m$ has changed slightly compared to the ring resonator $(\theta + \varphi t) = 2\pi m$. The drop port transmission at resonance is no longer independent of t and κ . Thus, leading to a significant performance change and confirming the importance of taking into consideration the phase difference.

One important ring resonator parameter is the distance between the resonance peaks, which is called the free spectral range (FSR) and that can be described by (Rabus, 2007, p. 8):

$$FSR = \Delta\lambda = -\frac{2\pi}{L} \left(\frac{\partial\beta}{\partial\lambda} \right)^{-1} \approx \frac{\lambda^2}{n_{eff}L} \quad (2.20)$$

If we include the wavelength dependency of the effective refractive index then the group index n_g which is defined as $n_g = n_{eff} - \lambda \frac{\partial n_{eff}}{\partial\lambda}$, can be included in the equation (2.20). Then the modified version of eqn. (2.20) given in (Rabus, 2007, p. 9) is:

$$FSR = \Delta\lambda = \frac{\lambda^2}{n_g L} \quad (2.21)$$

which can be used whenever appropriate to avoid the approximation and hence obtain more accurate values. Another important parameter is the width of the resonance which is defined as full width at half maximum (FWHM) or 3-dB bandwidth ($2\delta\lambda$) of the resonance lineshape. It is derived in Appendix I and is presented in (Rabus, 2007, p. 9) as:

$$FWHM = 2\delta\lambda = \frac{\kappa^2 \lambda^2}{\pi L n_{eff}} \quad (2.22)$$

Another parameter that can be directly calculated from the above relations is the finesse (F) of the ring resonator filter. It is defined as the ratio of the FSR to the width of a resonance for a specific wavelength (FWHM). This relation is given in (Rabus, 2007, p. 10) as follows:

$$F = \frac{FSR}{FWHM} = \frac{\Delta\lambda}{2\delta\lambda} = \pi \frac{t}{1-t^2} \approx \frac{\pi}{\kappa^2} \quad (2.23)$$

One more important parameter which is closely associated to the finesse is the quality factor (Q) of a resonator which is the measure of the sharpness of the resonant peak. It is defined as the ratio of the operation wavelength over the resonance width (Rabus, 2007, p. 10) as:

$$Q = \frac{\lambda}{2\delta\lambda} = \pi \frac{n_{eff}L}{\lambda} \frac{t}{1-t^2} = \frac{n_{eff}L}{\lambda} F \quad (2.24)$$

For our design, we have specifically selected three racetrack resonators to be serially coupled in order to have a reflector configuration. The reflectors can only be designed by choosing the odd numbers of ring-resonators (such as $n=1,3,5,7,\dots$) such as the propagating light is reflected back to the input port. The coupling of these 3-racetrack resonators will help in achieving a broad FSR. The representation of the important functional parameters such as field coupling coefficient (κ), transmission coefficient (t) and the loss coefficient (α) within the ring can be seen in Figure 2.3. These parameters are kept the same while deriving the transfer equations for the output ports of the cascaded 3-ring filter. The input node is $E_{IN}(z)$, the through port node is $E_T(z)$ and the drop port node is $E_D(z)$. Since there are three rings, there are four coupling regions in the design. On the basis of the Mason's rule (Mason, 1956), the transfer function or input-output transmittance relationship, having ' n ' number of nodes (16 nodes depicted in Figure 2.3), from node $E_1(z)$ to node $E_n(z)$ is given by (Chaichuay, Yupapin, & Saeung, 2009):

$$H = \frac{1}{\Delta} \sum_{i=1}^n T_i \Delta_i \quad (2.25)$$

Where H is the network function relating an input to an output port, T_i is the gain (or transmittance) of the i -th forward path from an input to an output port and n is the total number of forward paths from an input to an output port. Δ_i is the determinant Δ after all loops which touch the T_i path at any node have been eliminated.

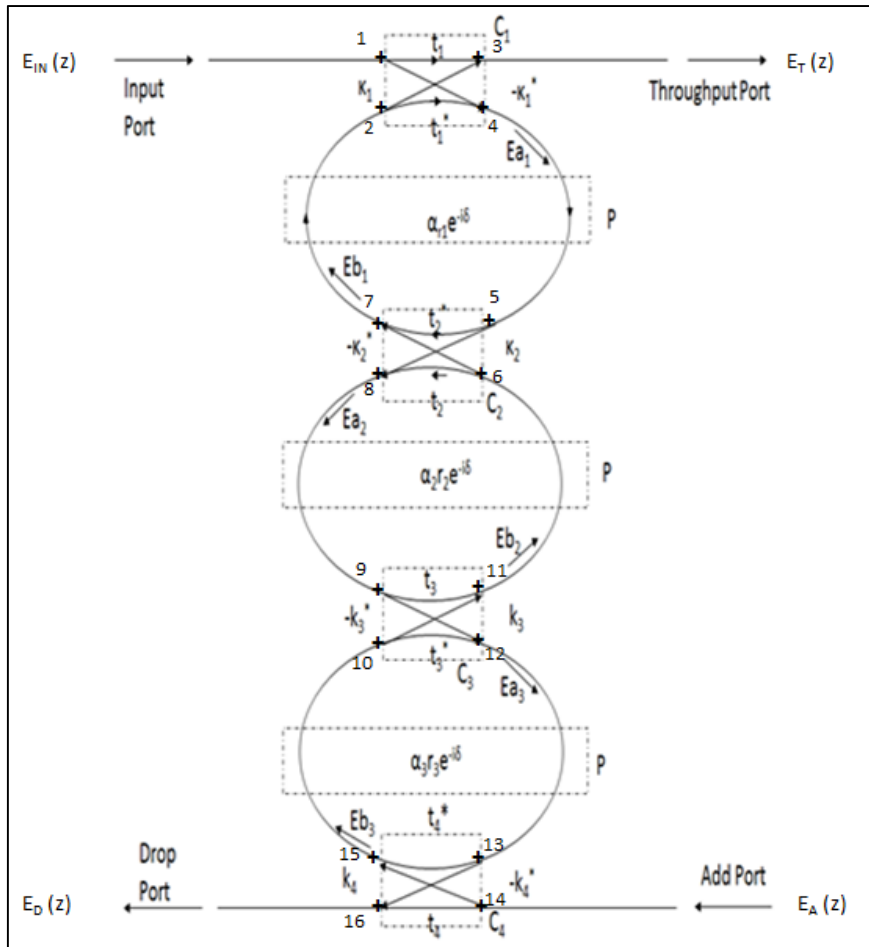


Figure 2.3 Model of a serially coupled three-ring add-drop filter showing the coupling coefficients and the loss coefficients for each ring

The forward path transmittances and its determinants from E_{IN} to node E_T and E_{IN} to node E_D are shown in Appendix II, leading to the transfer function for the through port as follows (Chaichuay et al., 2009):

$$\frac{E_T(z)}{E_{IN}(z)} = H_t^3 = \frac{t_1 - t_2 \alpha z^{-1} - t_1 t_2 t_3 \alpha z^{-1} + t_3 (\alpha z^{-1})^2 - t_1 t_3 t_4 \alpha z^{-1} + t_2 t_3 t_4 (\alpha z^{-1})^2 + t_1 t_2 t_4 (\alpha z^{-1})^2 - t_4 (\alpha z^{-1})^3}{1 - t_1 t_2 \alpha z^{-1} - t_2 t_3 \alpha z^{-1} - t_3 t_4 \alpha z^{-1} + t_1 t_3 (\alpha z^{-1})^2 + t_2 t_4 (\alpha z^{-1})^2 - t_1 t_4 (\alpha z^{-1})^3 + t_1 t_2 t_3 t_4 (\alpha z^{-1})^2} \quad (2.26)$$

Similarly, the transfer function for the drop port is given by (Chaichuay et al., 2009):

$$\frac{E_D(z)}{E_{IN}(z)} = H_d^3 = \frac{\kappa_1 \kappa_2 \kappa_3 \kappa_4 (\alpha z^{-1})^{3/2}}{1 - t_1 t_2 \alpha z^{-1} - t_2 t_3 \alpha z^{-1} - t_3 t_4 \alpha z^{-1} + t_1 t_3 (\alpha z^{-1})^2 + t_2 t_4 (\alpha z^{-1})^2 - t_1 t_4 (\alpha z^{-1})^3 + t_1 t_2 t_3 t_4 (\alpha z^{-1})^2} \quad (2.27)$$

In early years, before Si photonics became a path-breaking technology for integrated electro-optical systems, researchers mainly focused on III-V semiconductors and other glass materials. The first guided optical ring-resonator was demonstrated by (Weber & Ulrich, 1971) which was used for a laser application where they presented a device consisting of a 5-mm diameter glass rod ($n=1.47$) coated with a rhodamine 6G doped polyurethane film. This coated glass rod forms a ring like structure, placed in front of the pumping source, providing a positive feedback. The active medium is provided by the spiral resonator which has a circumference of 31.4 mm. The next relevant demonstration of a low-loss channel waveguides in a ring-resonator configuration was done by (Haavisto & Pajer, 1980) using a bus-waveguide made of a doped polymethyl methacrylate (PMMA) film on quartz substrate. Later, the first demonstration of tunable ring resonator on LiNbO_3 with Ti diffused waveguides was made by (Tietgen, 1984) where they used two 3-dB couplers forming a waveguide loop instead of a circular ring. This loop has a circumference of 24 mm operating at 790 nm wavelength. The first ever electro-optically tuned GaInAsP-InP microring notch filter was reported by (Grover et al., 2004).

Over the past decades, microring resonators have been widely used for implementing a variety of wavelength-selective reflectors such as reflective notch filters (H. Sun, Chen, & Dalton, 2009) (Shi, Vafaei, Torres, Jaeger, & Chrostowski, 2010) (Chae & Skafidas, 2013) and reflective band-pass filters (Chung, Kim, & Dagli, 2006) (Paloczi, Scheuer, & Yariv, 2005) (Poon, Scheuer, & Yariv, 2004). These filters are very promising for applications such as remote sensing (Shi et al., 2010) (H. Sun et al., 2009), tunable lasers (Sato et al., 2015) (Tao

Chu, Fujioka, & Ishizaka, 2009), optical modulators (Xu, Schmidt, Pradhan, & Lipson, 2005), optical switches (Mokhtari & Baghban, 2015) and WDM add-drop filters (Van, 2007) (W. Wang et al., 2012) (De Heyn et al., 2013). Over the past two decades, tunable lasers have been successfully demonstrated on the Si platform since the optical filters made of Si waveguides provides well confined light propagation. These filters provide a feedback to the laser gain chip forming a lasing cavity. A general schematic of an external cavity semiconductor laser for wavelength tuning in telecommunications can be seen in Figure 2.4, where a feedback on one side of the semiconductor gain element is provided by an optical filter (blazed grating here). The DBR laser demonstrated by (Y. Liu et al., 2006) is one such example, which has many attractive performances and is now available for commercial use in optical network systems. However, for advanced multi-level modulation formats they are hard to use because of their wider linewidth resulting from their long cavity length.

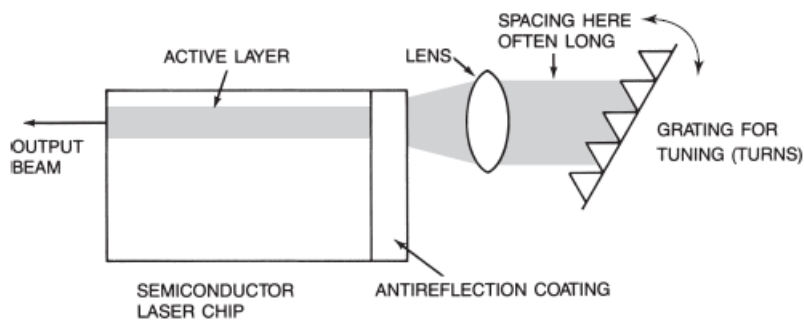


Figure 2.4 A general schematic of an external cavity semiconductor laser.

This grating has been replaced by compact ring resonators in different configurations such as a SiON waveguide based serially coupled triple ring-resonator (Matsumoto et al., 2010) in a loop configuration, in a Littman configuration (Jeon et al., 2008), one with a phase shifter inside the cavity (Kita, Nemoto, & Yamada, 2014), another with two ring-resonators in series (R Boeck, Shi, Chrostowski, & Jaeger, 2013) (Ishizaka & Yamazaki, 2006), a polymer waveguide based single ring reflector using Y-splitters (Paloczi et al., 2005) and in a loop configuration with an asymmetric Mach-Zhender Interferometer (MZI) (Kita et al., 2014). Serially coupled two or three ring resonator filters uses the Vernier effect in order to achieve a wide FSR so as to cover the entire communication C-band. In these configuration, the lasing

wavelength corresponds to the simultaneously resonant component with the two/three ring resonators and is tuned by shifting the resonant wavelengths either by heating one, both (T Chu, Fujioka, Tokushima, Nakamura, & Ishizaka, 2010) (Ren et al., 2016) or all three ring resonators (Matsumoto et al., 2010). Other research groups have reported interesting configurations such as the combination of a microring with a contra directional-coupler (contra-DCs) (Robert Boeck, Caverley, Chrostowski, & Jaeger, 2015) and integrating a distributed Bragg reflector (DBR) inside the microring (Arbabi, Kang, Lu, Chow, & Goddard, 2011). This integration was done in order to eliminate the FSR so as to achieve low-threshold and narrow linewidth single mode laser diodes. This miniaturized half-ring DBR, shown in Figure 2.5, acts as a narrowband on-chip mirror which is way more attractive than conventional



Figure 2.5 a) Schematic of the ring with integrated DBR. The DBR is realized by modulating the top half of the ring waveguide. b) SEM image of the fabricated device prior to top cladding deposition
Taken from Arbabi et al. (2011)

DBR because of their small sizes and smooth narrowband high reflective peak at a single wavelength. In comparison to these configurations, where they have used a waveguide loop as a reflector within the optical coupling section, we present a novel serially coupled three ring filter in a reflector configuration where the 3rd order ring filter is integrated with the Y-splitters and combiners. Moreover, the tuning mechanism used in above mentioned configurations is thermal (using heaters) which sometimes produces excess heat thereby, degrading the device performance. In addition to this drawback, they have high power consumption due to thermal tuning which can be mitigated by adopting an electro-mechanical tuning. Therefore, with the vision of reducing the power consumption, the ring reflectors presented in this thesis will be tuned electro-mechanically using micro-electro-mechanical-systems (MEMS) in the future.

Another challenge with the silicon waveguide optical filters is the large propagation losses that degrade the transmission characteristics of the tunable ring resonators. The waveguide propagation losses reported by (Bogaerts et al., 2012) for silicon waveguides with air cladding in the IMEC foundry (Selvaraja et al., 2009) was around 2.7 dB/cm resulting in a Q-factor for an add-drop resonator of 1.36×10^5 for a total length of 13 mm. This was drastically brought down to around 0.5 dB/cm by (Sato et al., 2015). They reported the best ever output power with more than 100 mW (20 dBm) at 25⁰C for a silicon photonic hybrid ring-filter external cavity (SHREC) wavelength tunable laser. This power was high in comparison to the previous best reported by (Wakaba et al., 2013) of around 90 mW at 70⁰C while achieving a wide tuning range of around 65 nm. The Si₃N₄ waveguide is less sensitive to fab dimensions and thus show low propagation losses as compared to the Si waveguide. Therefore, in this thesis, we demonstrate Si₃N₄ waveguide based ring-resonators to be used for different applications. A novel single ring reflector (similar to (Paloczi et al., 2005)) based on a Si₃N₄ waveguide and a Si 3rd order ring reflector design is presented in Chapter 3 with the goal to achieve a wide FSR with an aid of exploring the Vernier effect such that only a single channel lases within the gain bandwidth region. Thus, microring resonators are promising integrated filter components for developing compact external laser cavity allowing wide wavelength tuning range and high-Q factors at a low-cost for DWDM applications within the telecommunication bandwidth.

2.2 Microdisk Resonators for Transceiver Applications

Microdisk resonator is also a type of ring resonator, also known as travelling wave resonators (TWR), with a smaller internal radius of the inner ring (can be assumed as two concentric rings). The main advantage of TWRs over other optical filters such as Bragg gratings lies in the miniaturization of the devices. For a long time, it has been considered as a key opto-electronic filter with some of its modes giving a very high Q-factor (Levi et al., 1992). These modes, also known as whispering gallery modes (WGM), have light circulating around the circumference of the disk trapped by total internal reflection. In comparison to microrings, microdisks have smaller footprint, higher Q and wider FSRs which was shown by (Soltani, Li, Yegnanarayanan, & Adibi, 2010) by developing ultimate miniaturized microdisks and microdonuts (intermediate design between a disk and a ring shape). Microdisk have unique multi-modal and intrinsic ultra-

high Q properties (Soltani, Yegnanarayanan, & Adibi, 2007) due to which, careful coupling optimization is necessary to extract a single mode with the required Q_c (quality factor of the coupling between the microdisk resonator and bus waveguide). The energy tail of the WGM of a microdisk decays more rapidly in the radial direction and outside the disk, as compared to a microring of the same radius. This leads to a weaker coupling of the microdisk to an adjacent waveguide, compared to the microring, thereby, making it difficult to achieve a critical coupling. If microdisks have larger radii then achieving the required Q_c becomes more challenging, since the energy tail outside the disk approaches zero faster. A 100% energy transfer is possible from a bus waveguide to the resonator by an appropriate design of the waveguide-resonator coupling (Yariv, 2000). A few of the challenges faced when realizing such compact microdisk resonators are: firstly, the sidewall roughness induces scattering and absorption losses which can be reduced by developing improved fabrication techniques. Secondly, optimizing the waveguide-resonator coupling region to achieve critical coupling. These challenges were analysed by (Soltani et al., 2007) where they demonstrated a high $Q \sim 3 \times 10^6$ Si microdisk resonator. They developed two device architectures for disk-on-substrate and assessed its integration with active components evidencing the useful role of the substrate for both chip-scale device integration as well as active electronic device integration. In order to obtain a directional output, the rotational symmetry needs to be broken which can be done either by deforming the boundary which gives very low Q-factor (Gmachl et al., 1998), by inserting a linear defect (Apalkov & Raikh, 2004) or creating a hole (Wiersig & Hentschel, 2006) in a microdisk near the mode propagation region. For a microcavity with a thickness of only a fraction of mode wavelength, modes can be studied using a 2D approximation with the help of the effective refractive index $n(x, y) = n(r, \phi)$. In this approximation, the coordinate dependence of the EM field in the z-direction is omitted, resulting in the separated fields for the TM modes ($H_z=0$) and TE modes ($E_z=0$). For the TM modes the field is given by the relation (Dettmann, Morozov, Sieber, & Waalkens, 2008):

$$\frac{\partial^2 E_z}{\partial r^2} + \frac{1}{r} \frac{\partial E_z}{\partial r} + \frac{1}{r^2} \frac{\partial^2 E_z}{\partial \phi^2} + k^2 n^2(r, \phi) E_z = 0 \quad (2.28)$$

with,

$$H_r = -\frac{i}{kr} \frac{\partial E_z}{\partial \phi} \quad (2.29) \text{ a)}$$

$$H_\phi = \frac{i}{k} \frac{\partial E_z}{\partial r} \quad (2.29) \text{ b)}$$

For the TE modes with a new introduced function $h_z(r, \phi) = Hz(r, \phi)/n(r, \phi)$, we obtain (Dettmann et al., 2008):

$$\frac{\partial^2 h_z}{\partial r^2} + \frac{1}{r} \frac{\partial h_z}{\partial r} + \frac{1}{r^2} \frac{\partial^2 h_z}{\partial \phi^2} + k^2 n^2(r, \phi) h_z + \left[\frac{\nabla^2 n}{n(r, \phi)} - 2 \left(\frac{\nabla n}{n(r, \phi)} \right)^2 \right] h_z = 0 \quad (2.30)$$

with,

$$E_r = \frac{i}{kn(r, \phi)r} \left[\frac{\partial h_z}{\partial \phi} + \frac{1}{n(r, \phi)} \frac{\partial n(r, \phi)}{\partial \phi} h_z \right] \quad (2.31) \text{ a)}$$

$$E_\phi = -\frac{i}{kn(r, \phi)} \left[\frac{\partial h_z}{\partial r} + \frac{1}{n(r, \phi)} \frac{\partial n(r, \phi)}{\partial r} h_z \right] \quad (2.31) \text{ b)}$$

The relation for the effective refractive index and the field function (ψ) is derived and showed in Appendix III. Implementation of microdisks on a silicon platform has demonstrated a great potential for integration with other electronic and photonic devices. Among various micro-photonic components, microdisk resonators are being actively pursued for chip-scale silicon photonics (Srinivasan et al., 2005) (Borselli, Johnson, & Painter, 2005) (Johnson, Borselli, & Painter, 2006). Since, it is the most compact wavelength-selective reflector, it allows highly competitive tuning efficiency (in nm/W) for tunable lasers (Tao Chu et al., 2009). Due to their large tuning range and compact size they are promising for other applications such as sensing (Shi et al., 2012), optical routing switches (Emelett & Soref, 2005), stop-band filters (Morand et al., 2006), opto-mechanical oscillators (W. C. Jiang, Lu, Zhang, & Lin, 2012; X. Sun, Zhang, & Tang, 2012), force-gradient-actuated cavity opto-mechanics (X. Jiang, Lin, Rosenberg, Vahala, & Painter, 2009) (G. Li et al., 2015) and optical modulators (Zhou & Poon, 2006). These micro resonators have a very long photon life time and a strong electric field enhancement because of the small mode volumes and a high Q-factor that is achievable at such scale. This makes them a suitable candidate for the enhancement of light-matter interactions (Barclay, Srinivasan, Painter, Lev, & Mabuchi, 2006). These optical interconnects tends to revolutionize the computing technology with a minimal loss and high bandwidths.

2.3 Silicon nitride waveguide based Microring and Microdisk Resonators

Over the past decade, we have observed a tremendous development of photonic integrated circuits over silicon-on-insulator (SOI). The merits of using Si-photonics platform are large-area substrates, CMOS compatible high yield fabrication, availability of sophisticated assembly processes and enabling the manufacturing of densely integrated electro-optic components at low costs and high volumes (Soref, 2006) (Baehr-Jones et al., 2012) (Lim et al., 2014). Si-photonics is befitting for large complex photonic circuits, optical interconnect networks and optical switching networks, but, due to the losses, crosstalk and the fabrication tolerance of the conventional Si photonic platforms, its implementation is sometimes limited. Recently, low loss Si_3N_4 waveguide has been considered as a potential candidate for an integrated photonic platform. Its superior passive optical properties to Si (Henry, Kazarinov, Lee, Orlovsky, & Katz, 1987), a moderate refractive index (in-between oxide and Si) and low propagation losses in comparison to Si makes it a suitable material for realizing optical components for transceiver applications. Si_3N_4 has other advantages over Si such as it does not suffer from two photons and free carrier absorption over the telecommunication wavelength ranges which are preferred for parametric oscillation applications. Moreover, its third order non-linear susceptibility ($\chi^{(3)}$) is about 20 times smaller than that of the silicon (Dinu, Quochi, & Garcia, 2003) (Ikeda, Saperstein, Alic, & Fainman, 2008). The lower index contrast of a silicon nitride (Si_3N_4 , $n \approx 2$) to silica (SiO_2 , $n \approx 1.45$) compared to silicon (Si, $n \approx 3.48$) reduces waveguide losses due to sidewall roughness scattering. It is less sensitive to fabrication variations as compared to Si. Photonic components made of Si_3N_4 are also less temperature sensitive owing to a thermo-optic coefficient that is about five times smaller than that of Si (Amatya et al., 2007) (Cocorullo, Della Corte, & Rendina, 1999). Due to the above mentioned optical properties, many research groups are currently working and have recently demonstrated the integration of Si_3N_4 waveguides onto the SOI platform (Chen, Doerr, Buhl, Baeyens, & Aroca, 2011) (Jones et al., 2013) (Sodagar, Pourabolghasem, Eftekhari, & Adibi, 2014) and with hybrid III/V silicon platform (Piels, Bauters, Davenport, Heck, & Bowers, 2014), so as to combine active and passive optical functionalities in the Si-based integrated photonics.

Silicon nitride based waveguides are very promising in an integrated photonics research due to their CMOS-compatibility (Moss, Morandotti, Gaeta, & Lipson, 2013). Stoichiometric silicon nitride (Si_3N_4) deposited using low pressure chemical vapour deposition (LPCVD) (Epping et al., 2015) offers extremely low intrinsic losses and high reproducibility. It also provides a broad transparency range from the visible to the mid-infrared region which includes all the telecommunication bands. The other techniques to deposit Si_3N_4 are using electron cyclotron resonance plasma enhanced chemical vapor deposition (ECR-CVD) (do Nascimento et al., 2014), liquid source chemical vapor deposition (LSCVD) (Cheng, Hong, Spring, & Yokoyama, 2017) and PECVD (Sacher, Huang, Lo, & Poon, 2015). Some researchers have demonstrated a very thin ~ 40 nm Si_3N_4 waveguides, with weak mode confinement, but providing ultra-low propagation losses in the C-band of around 0.32 dB/m (Spencer, Bauters, Heck, & Bowers, 2014). However, this low confinement of the modes has the drawback of increased bending losses and as a result it limits the density of devices in the integrated circuits. Ultra-low propagation loss of 0.1 dB/m for low confined Si_3N_4 waveguides (Bauters et al., 2011) in comparison to 0.3 dB/m for Si waveguides (Kohtoku, Kominato, Nasu, & Shibata, 2005) have been reported. For highly confined waveguides, the lowest reported loss is around 4.2 dB/m (Luke, Dutt, Poitras, & Lipson, 2013) where scattering losses due to sidewall roughness are reduced by increasing the thickness of the SiN layer which is low compared to 2-3 dB/cm reported for the standard Si channel waveguide (Lim et al., 2014). The silicon nitride deposition technique used in our process flow is PECVD (discussed in Chapter 3) which aids in achieving less lossy waveguide structures.

Thus, silicon nitride waveguides are considered to be a good replacement to silicon waveguides to fabricate optical devices using a CMOS compatible process. Different optical filters have been designed but the micro ring-resonator/disk-resonator due to their wide range applicability are of profound interest. They are being widely used in the telecommunication field for (mode division multiplexing) MDM-compatible WDM (wavelength division multiplexing) applications (Yang, Li, Huang, & Poon, 2014), in semiconductor ECL (Oldenbeuving et al., 2012) (Fan et al., 2014) and as optical add-drop filters (Tien et al., 2011) for channel selection

mechanism (Dai, Bauters, & Bowers, 2012). Silicon nitride ring resonators have other applications in biosensors (Goykhman, Desiatov, & Levy, 2010), in optical coherence tomography (Yurtsever et al., 2014) in microwave photonics (Marpaung et al., 2013), for lab-on-a-chip devices due to its compatibility with microfluidic channels (Cai & Poon, 2012) (Ymeti et al., 2005), for optical parametric oscillator (Levy et al., 2010) and in the visible wavelength range (Hosseini, Yegnanarayanan, Atabaki, Soltani, & Adibi, 2009) (Stutius & Streifer, 1977).

MEMS based tunable ring resonators are excellent candidates for wavelength selection in reconfigurable optical networks due to their static low power consumption and high Q. They have found application as an optical add-drop filters in reconfigurable optical networks (Errando-Herranz, Niklaus, Stemme, & Gylfason, 2015), in external cavity tunable lasers (Ren et al., 2016) and DWDM applications. Different MEMS actuation techniques have been proposed to perturb the evanescent field of the ring and to extract the resonant wavelength such as depositing bimorph cantilever on top of ring resonator (Abdulla et al., 2011), by obtaining a cantilever through etch slots and etch holes (Errando-Herranz et al., 2015), by using comb-drive actuators (Hah, Bordelon, & Zhang, 2011) (Hah & Bordelon, 2015) and by using micro mirrors (Brière, Beaulieu, Saidani, Nabki, & Menard, 2015) (Briere et al., 2017). The deflection of cantilever over the ring resonator resulted in a short wavelength shift of 122 pm in (Abdulla et al., 2011) as compared to 530 pm of wavelength shift in (Errando-Herranz et al., 2015). A comb-drive actuation presented in (Hah & Bordelon, 2015) is interesting since the power is required only during a transition while the resonant wavelength is changed and once the tuning is complete no more power is required to maintain the tuned state. This tuning is achieved via evanescent coupling from the resonator to a suspended waveguide (or index modulator) causing change in the effective indices of the modes propagating through the resonator. Thus, by varying the distance between the index modulator and the resonator, the resonant wavelength of the filter can be tuned in a continuous fashion.

Due to the above-mentioned properties and advantages of Si_3N_4 waveguide devices over traditional silicon waveguide devices, the passive optical filters based on the silicon nitride

waveguides are demonstrated further in this thesis. A reflective optical filter is presented in chapter 3 which will be integrated along with the MEMS actuating mirrors, as presented by our team in (Brière et al., 2015), in order to develop a wavelength channel selection mechanism to implement a tunable laser. By varying the MEMS actuation voltage, the mirror angle can be changed which helps in selecting one of the ring reflector. This changes the wavelength of the light that is reflected back inside the gain medium and hence the resonant wavelength of the laser cavity. The discrete nature of the wavelength selection process simplifies the control of the electrostatic actuator by enabling a simple feedback mechanism based on a laser output power. This tunable laser will be implemented along with the Si_3N_4 racetrack resonator, presented in chapter 4, to realize a novel tunable transceiver required for long range transmission of data signal.

CHAPTER 3

RING-REFLECTOR FOR TUNABLE LASER APPLICATION

In order to meet the rapid increase in data transfer rates, digital coherent optical communication system is superseding traditional on-off keying systems. Various optical devices have been developed for realizing digital coherent systems, such as wavelength tunable laser diode. These wavelength tunable lasers are expected to have a narrow spectral bandwidth which makes them an optimum coherent emitter. A tunable laser generally comprises of a gain medium, a lasing cavity and a wavelength tunable filter. Two types of wavelength tunable filters are presented in this thesis: a) Serially coupled three ring filter and b) Single ring filter, both in a reflector configuration which will be micro-mechanically tuned using MEMS actuator in the future. By changing the voltage, the MEMS actuator changes the mirror angle which helps in obtaining the lasing wavelength. This can be seen in Figure 3.1, which shows a general schematic of the micro-electromechanically tuned wavelength tunable laser. The light propagating from the gain medium is filtered by three ring resonators in the reflector configuration (integrated with

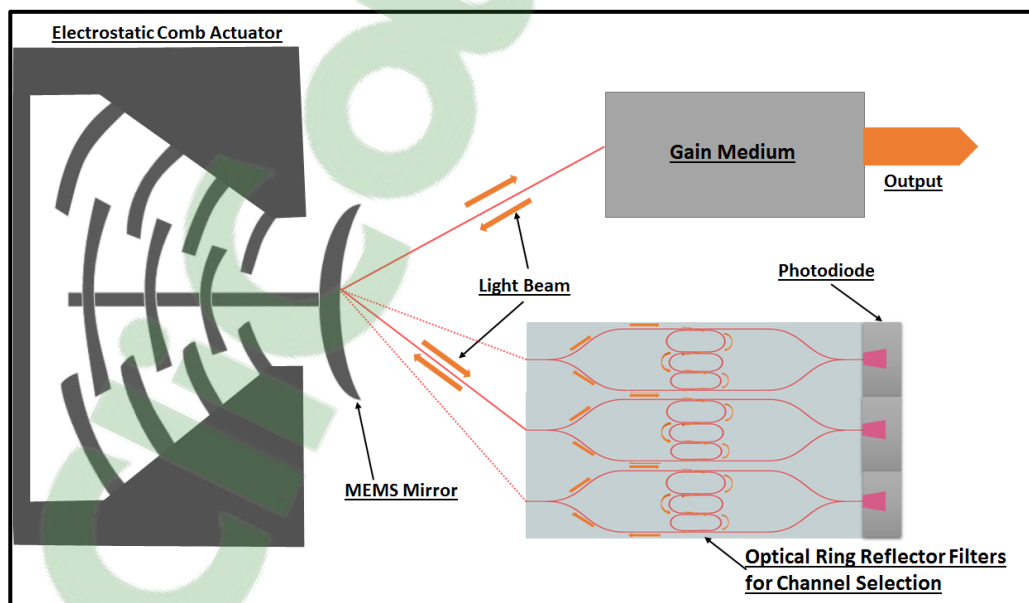


Figure 3.1 A general schematic of a wavelength tunable laser electromechanically tuned using a MEMS actuator

Y-splitter/combiner) having different FSRs and is then reflected back to the gain medium providing a feedback mechanism. These three rings provide a wide FSR by using the Vernier effect and thus the wavelength channel selection region is wide enough to cover the entire C-band. Due to the wide FSR, there is only one or two distinctive modal peaks in between the gain bandwidth region and the wavelength peak with the highest gain lases. Ring reflectors are chosen, instead of other filters such as Bragg gratings, so as to reduce the footprint of the device and keep it cost-effective.

Ring filters are the prime candidates to be used in the tunable lasers for WDM applications (Xia, Rooks, Sekaric, & Vlasov, 2007) (Dong et al., 2010) (Popovic et al., 2007). The wavelength tuning range has to be wide enough allowing more channels to be utilized in the WDM systems (R Boeck et al., 2013). Achieving a wide FSR using a single ring is challenging while maintaining bending losses to minimal and thus several rings are cascaded (Dahlem et al., 2010) (Popovic et al., 2007) (Xia et al., 2007) in order to have a wide FSR by exploring the Vernier effect. In the Vernier effect, multiple ring resonators having different optical path lengths are serially coupled (Fegadolli et al., 2012). Each ring-resonator has a different FSR corresponding to its total optical path length. When coupled in series, these FSRs gives few dominant peaks, which are higher than the rest of the peaks in spectrum, showing an alignment of the resonant wavelengths of the cascaded rings. These dominant peaks represent an extended FSR. This was shown by (Tao Chu et al., 2009) where for the first time they reported the wavelength tunable laser module developed with the micro ring-resonators followed by demonstrating the ultra-wide tuning range of 100 nm (T Chu et al., 2010) next year. They used thermal wavelength tuning mechanism which causes heat dissipation and consumes high power which was also used by (X. Li et al., 2015) demonstrating a Si single ring reflector in a Y-splitter configuration. (Timotijevic et al., 2009) and (Koonath, Indukuri, & Jalali, 2006) have also demonstrated a wide tuning range on a Si platform but they have showed low interstitial peak suppression. (Robi Boeck, Jaeger, Rouger, & Chrostowski, 2010) shows a FSR of 36.2 nm on a SOI platform which is thermally tuned, having a side mode suppression ratio larger than 11dB. They clearly demonstrated a high interstitial peak suppression of the twin peaks along with a minimal splitting of the main resonance peak. Other wavelength tuning

techniques are opto-mechanical tuning (Ren et al., 2016) and electrical tuning. Few research groups have demonstrated 3rd order ring filters using Si₃N₄ waveguide (Barwicz et al., 2006) reporting a low 3-dB drop loss with a wide FSR of 24 nm (Barwicz et al., 2004). In this chapter we present a 3rd order and a 1st order reflective ring filters based on silicon and silicon nitride waveguides, respectively, with an aim of achieving a wide FSR for a wavelength tunable laser application.

3.1 Design Approach

Our design consists of three racetrack resonators serially coupled and integrated with Y-splitter/combiner to form a reflector configuration. A schematic of a cascaded 3-ring reflector can be seen in Figure 3.2 where in all three racetrack resonators have different optical path lengths (L_1 , L_2 and L_3) so as to have different corresponding FSRs. These different FSRs, as coupled in series, will give dominant peaks showing the alignment of the resonant wavelengths of the three rings which is due to the Vernier effect. Thus, resulting in an extension of the FSR that should be large enough to cover the entire C or L band (>40 nm).

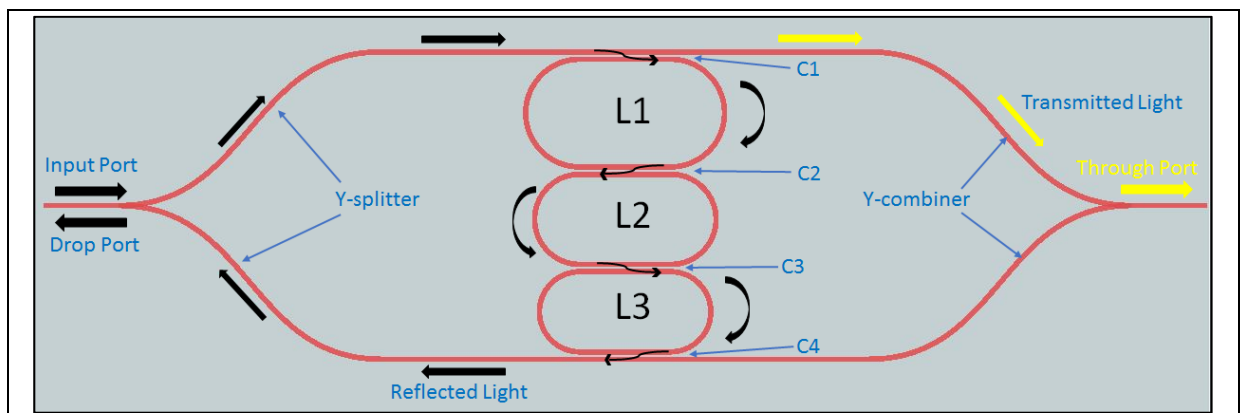


Figure 3.2 Schematic of the proposed 3-ring reflector filter having racetrack-resonator serially coupled and integrated with two Y-branch splitters showing propagation of the reflected and the transmitted light within the filter

The racetrack resonators and the Y-splitter/combiner are designed such that, all the resonant wavelengths (shown by black arrows in Figure 3.2) from the light injected through the input port are reflected towards the same port. All the non-resonant wavelengths (shown in yellow

arrows in Figure 3.2) travel straight towards the through port giving the transmitted peaks. The waveguide branches of a Y-splitter and a Y-combiner form the bus-waveguides of the rings 1 and 3 and defines a coupling region C1 and C4. The ring 2 forms the coupling regions C2 and C3 along with the ring 1 and 3, respectively. The Y-splitter/combiner (also known as 3-dB couplers) are designed such that they split the power equally (50:50) into the two waveguide branches forming the bus waveguides. When the light mode is injected from the input port, the light power splits at the Y-junction. The resonant wavelengths are extracted from the light propagating at the upper branch of the Y-splitter by coupling into the ring 1 through the coupling region C1 and propagates in a clockwise direction (black colour light) within the racetrack resonator 1. All the resonant frequencies are coupled then through the coupling region C2 and propagates inside the racetrack resonator 2 in an anticlockwise direction (black colour light). Further, all the resonant wavelengths, couples through C3 and propagates clockwise (black colour light) within the racetrack 3 and finally moves out of the ring and are extracted at the reflected port. The extended FSR is related to the FSR of each racetrack resonator by (Schwelb, 2007) (Chaichuay et al., 2009):

$$FSR_{\text{extended}} = m_1 FSR = m_2 FSR = m_3 FSR \quad (3.1)$$

Where m_1 , m_2 and m_3 are resonant numbers for each racetrack resonator and are all co-prime integers. Initially the racetrack resonators in the design were chosen to be symmetric i.e. they had similar coupling lengths and constant gaps between inter-ring coupling regions and the ring and the bus-waveguide regions (the field coupling coefficient κ was same). But later the coupling regions were optimized to have proper peak response as discussed in equation 2.26 and the ' m ' values were carefully chosen to avoid occurrence of twin peaks and to obtain large interstitial peak suppression.

3.2 Simulations and Optimization

3.2.1 Simulation of a channel waveguide

In this chapter, we are presenting a single ring reflector and a cascaded 3-ring reflector based on silicon nitride (Si_3N_4) and silicon (Si) waveguides, respectively. The silicon nitride waveguide has a dimension of 435 nm (width) x 435 nm (height), deposited over Si wafer, buried in between 4 μm thick silicon dioxide (SiO_2) cladding from above and 4 μm from below whereas the Si waveguide is 440 nm wide and 220 nm high deposited over 2 μm thick clad and protected by 2 μm thick oxide cladding over it. The Si waveguides are fabricated on a SOI platform. The waveguide geometries are chosen to ensure single mode propagation for the TE polarization while still having low propagation losses near 1550 nm. The high refractive index contrast between Si/ Si_3N_4 and SiO_2 enables strong confinement of the optical mode. The chosen dimensions of Si_3N_4 waveguide provide a single mode propagation which was required by our industrial partner AEPONYX.

Assuming an ambient temperature of 300K, the waveguide effective refractive index ' n_{eff} ' (for both Si and Si_3N_4 waveguides) were numerically calculated using Eigenmode solver in Lumerical MODE. When a waveguide is modelled, Maxwell's equations are then formulated into a matrix eigenvalue problem which are rigorously solved by an Eigenmode solver, giving the optical mode profiles and effective refractive index of the waveguide modes. The n_{eff} and the group index n_g are wavelength dependent and can be seen in Figure 3.3 and Figure 3.4 for silicon nitride and silicon waveguides, respectively. In Figure 3.4(c), we observe a sudden drop in the value of n_g near wavelength 1600 nm which could be due to some numerical error. If we go beyond 1600 nm, it follows a same trend (straight line) as before 1600 nm. The propagation constant of the guided mode at a single wavelength can be calculated as $\beta = 2\pi n_{eff}/\lambda$. Since the n_{eff} is highly dispersive, sometimes we have used the group index n_g in our calculations for predicting the FSRs to be more accurate.

$$n_g = n_{eff} - \lambda \frac{dn_{eff}}{d\lambda} \quad (3.2)$$

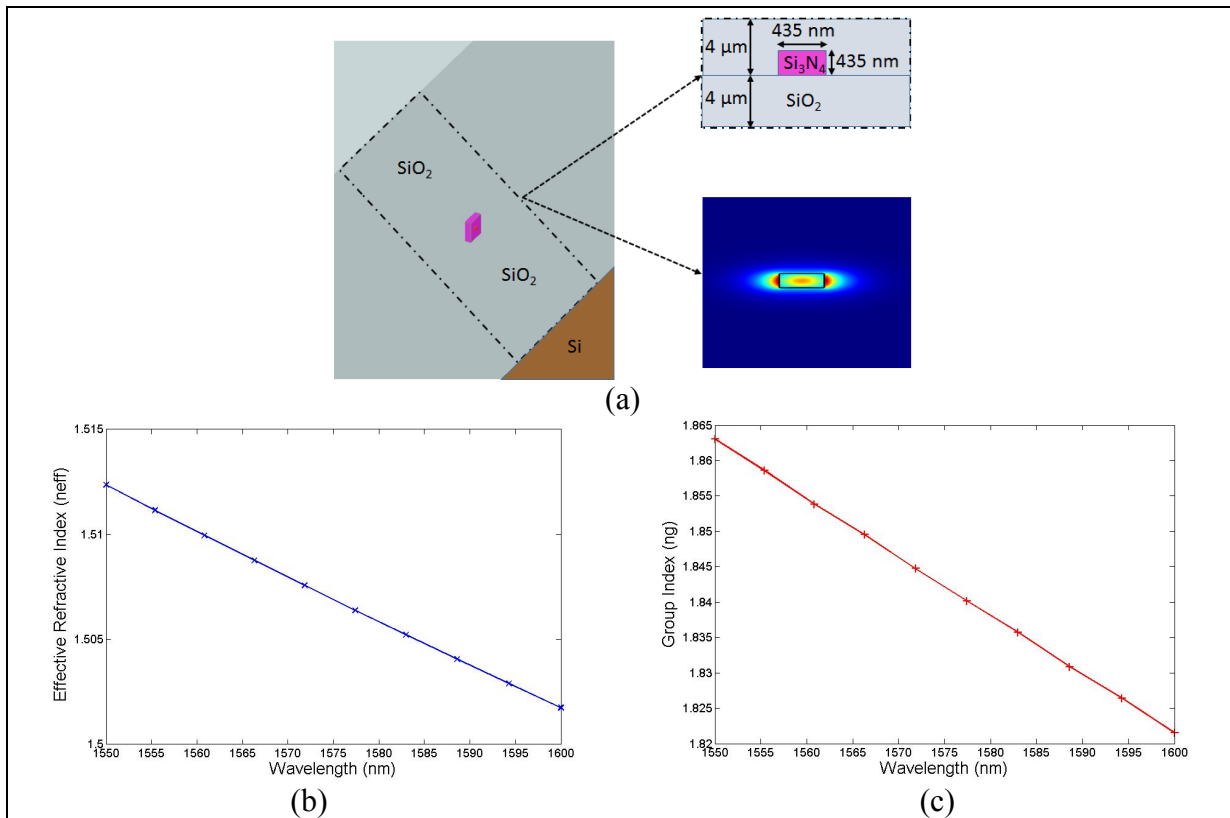
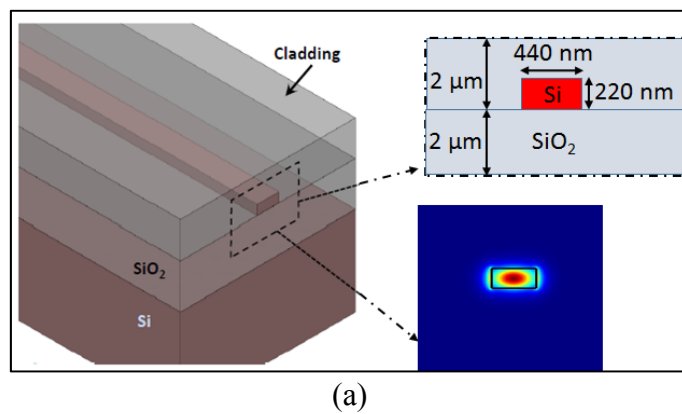


Figure 3.3 (a) Perspective view of Si_3N_4 channel waveguide with insets showing the cross-section waveguide geometry and TE mode distribution; (b) Wavelength dependent effective index (c) Wavelength dependent group index



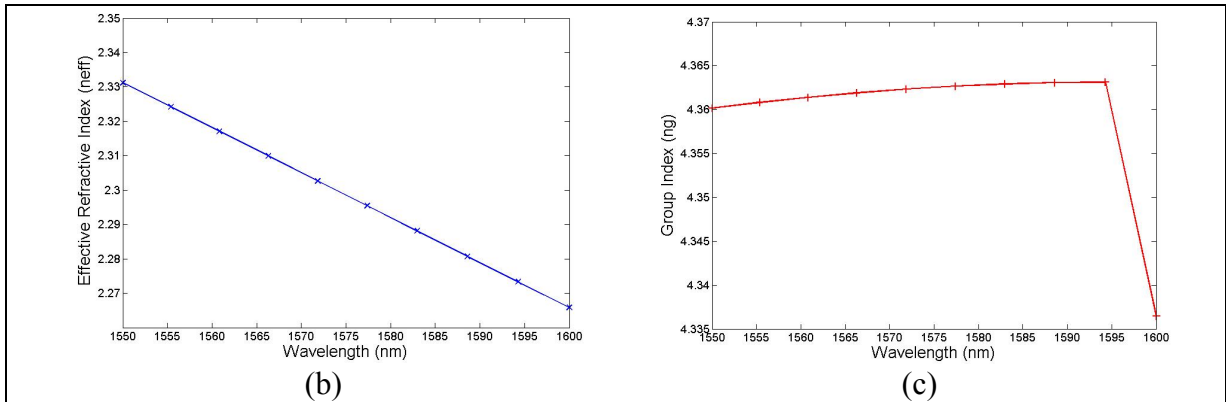


Figure 3.4 (a) Perspective view of Si channel waveguide with insets showing the cross-section waveguide geometry and TE mode distribution; (b) Wavelength dependent effective index; (c) Wavelength dependent group index

The effect of the change in the waveguide width on the n_{eff} and n_g for the silicon nitride waveguide and the silicon waveguide can be seen in Figure 3.5 (a) & (b), respectively. This n_{eff} dependence on the waveguide width is helpful in analysing the fabrication sensitivity of the waveguide and its impact on the device performance.

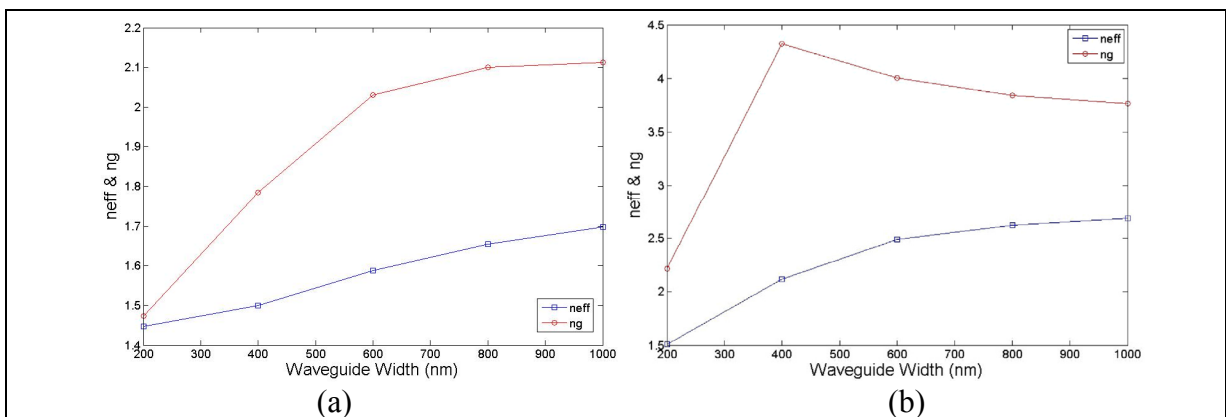


Figure 3.5 The effect of waveguide width variation over n_{eff} and n_g at 1550 nm for (a) Silicon nitride waveguide (thickness of 435 nm), (b) Silicon waveguide (thickness of 220 nm)

3.2.2 Simulation of a Directional Coupler

A directional coupler consists of two identical parallel waveguides with an optimized gap and a coupling length. The desired coupling coefficient and the transmission coefficient are obtained on the basis of the supermode analysis, as described in equations (2.5) and (2.6). The other important parameters of directional couplers are calculated using the same approach as mentioned in section 2.1. The supermodes for both types of waveguides and their n_{eff} dependence over the coupling gap can be seen in the Figure 3.6. The power behaviour within a directional coupler can be expressed as a function of the structure of the coupler, position of the coupler, the coupling coefficients and the power transmission ratio. From Figure 3.6 (b) we can see that for a Si waveguide based directional coupler, the Δn (difference between first two super modes) is very low and the supermodes converge around 1000 nm gap. On the other hand, Δn is still high for the directional coupler based on low refractive index contrast waveguide (in Figure 3.6 (a)) above 1000 nm gap. The symmetric modes of Si_3N_4 waveguides at lower gaps are well confined but antisymmetric modes tend to drift towards oxide layer, which is not the case for Si waveguide. In our simulations we assume that the coupling between

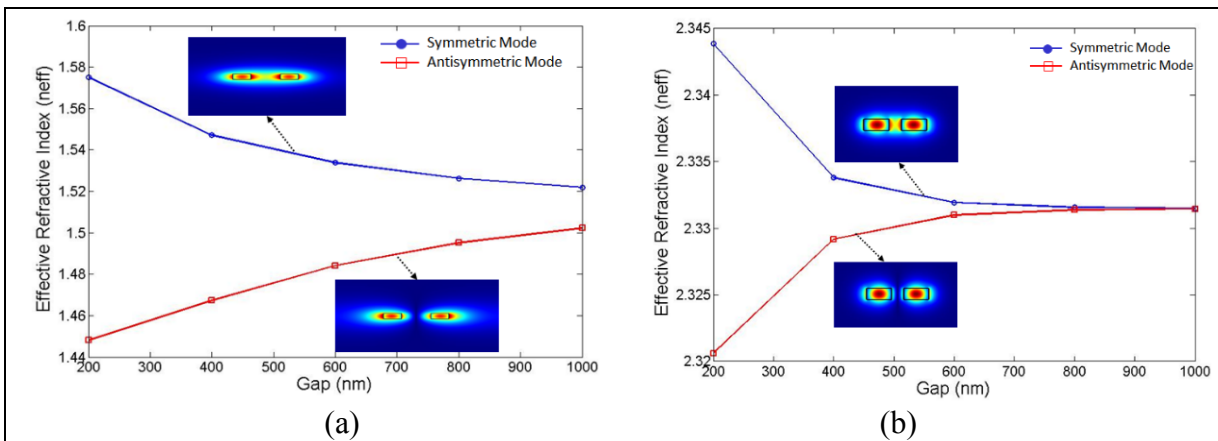


Figure 3.6 Symmetric and Antisymmetric modes dependence over the coupling gap at 1550 nm for (a) Si_3N_4 waveguide (b) Si waveguide; with insets showing supermodes electric field distribution

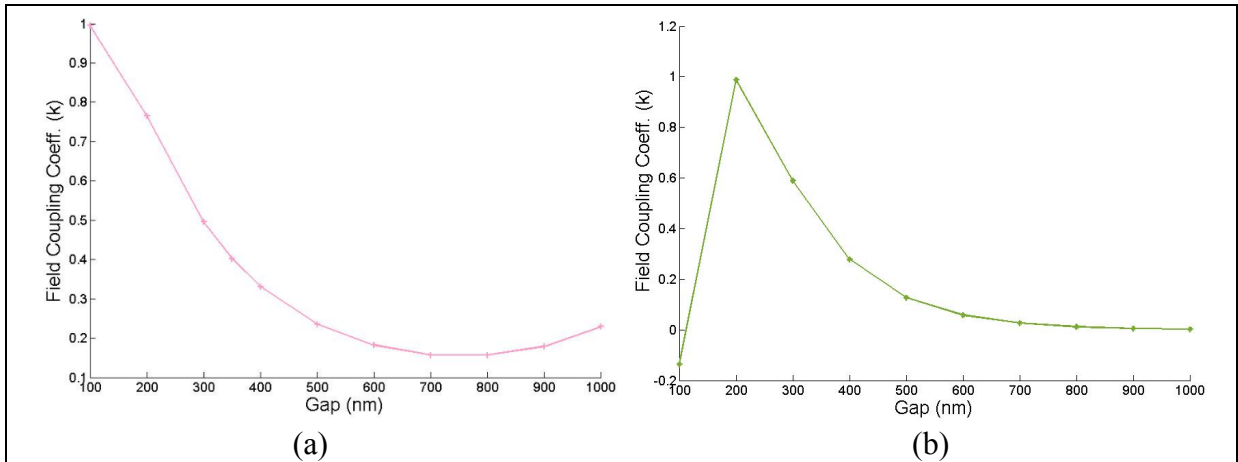


Figure 3.7 Field coupling coefficient ‘k’ versus coupling gap at 1550 nm for (a) Silicon nitride waveguide having dimensions 435 nm x 435 nm ($L=20\ \mu\text{m}$), and (b) Silicon waveguide having dimensions 440 nm x 220 nm ($L=20\ \mu\text{m}$)

the straight waveguide and ring is solely due to the coupling between the parallel section of the coupler and it does not include the bent region of the waveguide. The dependence of κ over varying coupling gaps for the silicon nitride waveguide and the silicon waveguide can be seen in Figure 3.7 (a) & (b), respectively. We notice that in Figure 3.7 (b), 20 μm long coupler has an almost zero coupling for a 100 nm gap. This is because the cross-over length (L_x) is 14.37 μm , hence the light goes through (almost) a complete cycle where (almost) all the power is returned to the original input waveguide. The field coupling coefficient κ helps in deciding the coupling condition and is carefully chosen to have a critical coupling condition. The κ further helps in deciding the other important design parameters such as coupling gap, coupling length, cross-over length, etc.

3.2.3 Simulation of a Silicon Nitride Ring Reflector

A silicon nitride ring reflector includes a single ring integrated with two Y-splitter/combiner. A general schematic of which can be seen in Figure 3.8. The mask layout dimension for the straight and the curved waveguides are 435 nm (width) x 435 nm (height) deposited over 4 μm SiO_2 layer and protected by 4 μm oxide cladding over it. The Si_3N_4 layer is deposited using LPCVD technique as per the requirements of the fab team in developing the process flow. The

ring radius considered for the design is $35\ \mu\text{m}$ which is selected based on the waveguide bending loss criterion shown in Figure 3.9 where the optical transmission is defined as a ratio of the output power versus the input power. This helps in achieving the minimum possible total optical path length so as to achieve a wide FSR with minimal bending and scattering losses. The total optical path length for the ring resonator is $220.56\ \mu\text{m}$ and is optimized to target the wavelength of interest at $1550\ \text{nm}$.

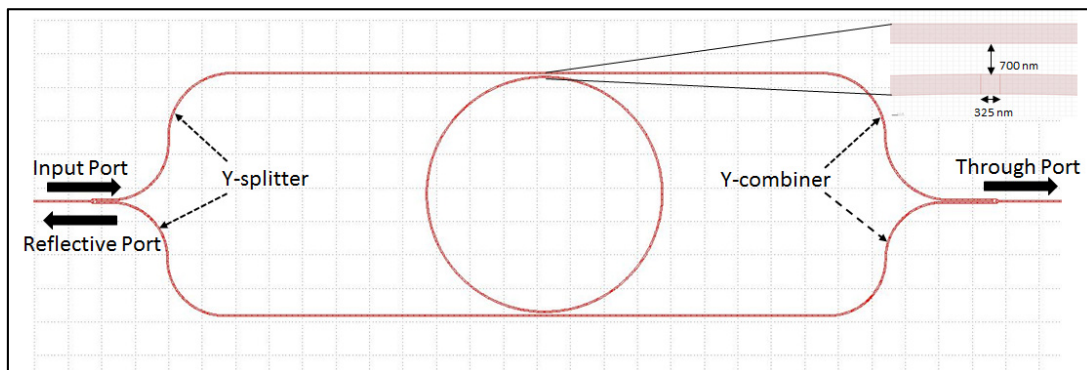


Figure 3.8 General schematic of a single ring reflector based on Si_3N_4 waveguide with dimensions $435\ \text{nm} \times 435\ \text{nm}$

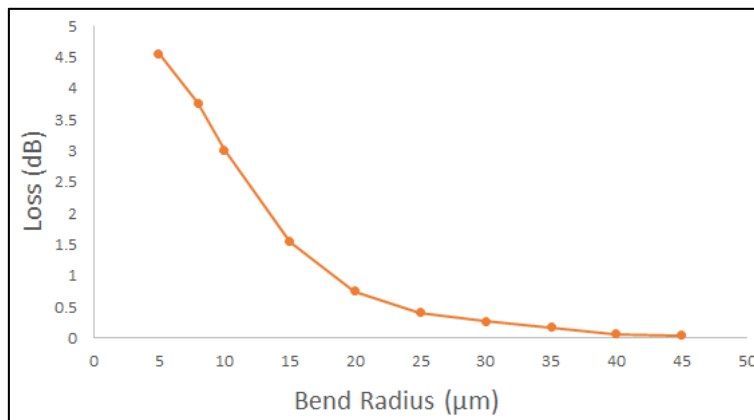


Figure 3.9 Waveguide bend loss versus radius for $435\ \text{nm}$ wide Si_3N_4 waveguide (in dB scale)

The κ is an important parameter for the selection of the design parameters of an add-drop ring resonator and to achieve the critical coupling condition. The effect of κ on the drop port peak intensity and on 3-dB bandwidth of the resonance peak can be seen in Figure 3.10. The

optimum κ is chosen to be 0.22 so as to achieve the critical coupling condition with high peak intensity and a narrow 3-dB bandwidth. Based on κ , other design parameters such as coupling length (L_c) and the coupling gap between the bus-waveguide and the ring resonator are determined to be 325 nm and 700 nm, respectively. The waveguide propagation loss considered while simulating is around 1 dB/cm (Bauters et al., 2011).

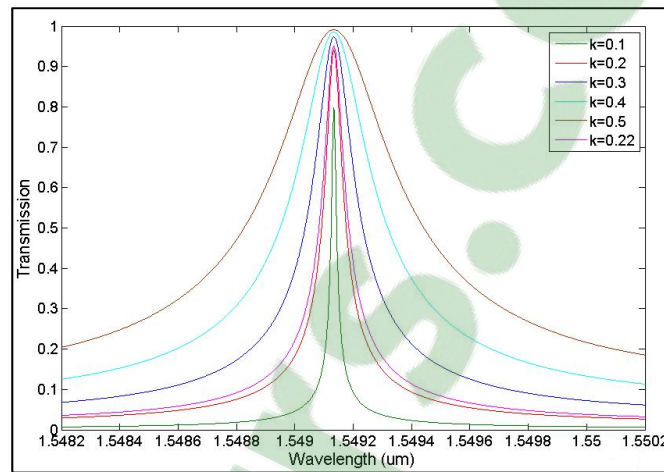


Figure 3.10 Effect of field coupling coefficient κ on the drop port peak intensity of an add-drop ring resonator

At a wavelength of 1550 nm, the refractive index considered for Si_3N_4 and SiO_2 is 2.04586 and 1.45, respectively. This value of Si_3N_4 is taken as an average over the wide wavelength range using Sellmeier equations. The n_{eff} of symmetric and antisymmetric mode for a 435 nm wide Si_3N_4 waveguide evaluated using finite difference element (FDE) simulations are 1.5281 and 1.4902, respectively (as seen in the inset of Figure 3.6 (a)) and their corresponding group indices are 1.8326 and 1.9124, respectively. The supermodes are evaluated using the Eigenmode solver in Lumerical MODE. The Y-splitters are designed to split the light power equally (50:50) into the two waveguide branches forming the bus waveguides for the ring such that the reflected resonant peaks are obtained at the input port. The total transmission loss obtained for the simulated Y-splitter in 2.5D-FDTD is 0.19 dB. The complete optimized design of the ring filter, including the ring-resonator integrated with the Y-splitter/combiner, is simulated using the 2.5D-FDTD solver and the obtained spectral response can be seen in the Figure 3.11 (a). The obtained FSR is around ~ 6.2 nm with a central resonant peak at 1549.9

nm. The transmission peak shows an extinction ratio of around ~ 67.72 dB. The plot (b) in Figure 3.11 represents a zoom in of a resonant peak at 1549.9 nm showing a 3-dB bandwidth of 0.97 nm giving a Q-factor of 1598. The total insertion loss of the device is calculated to be 0.1 dB.

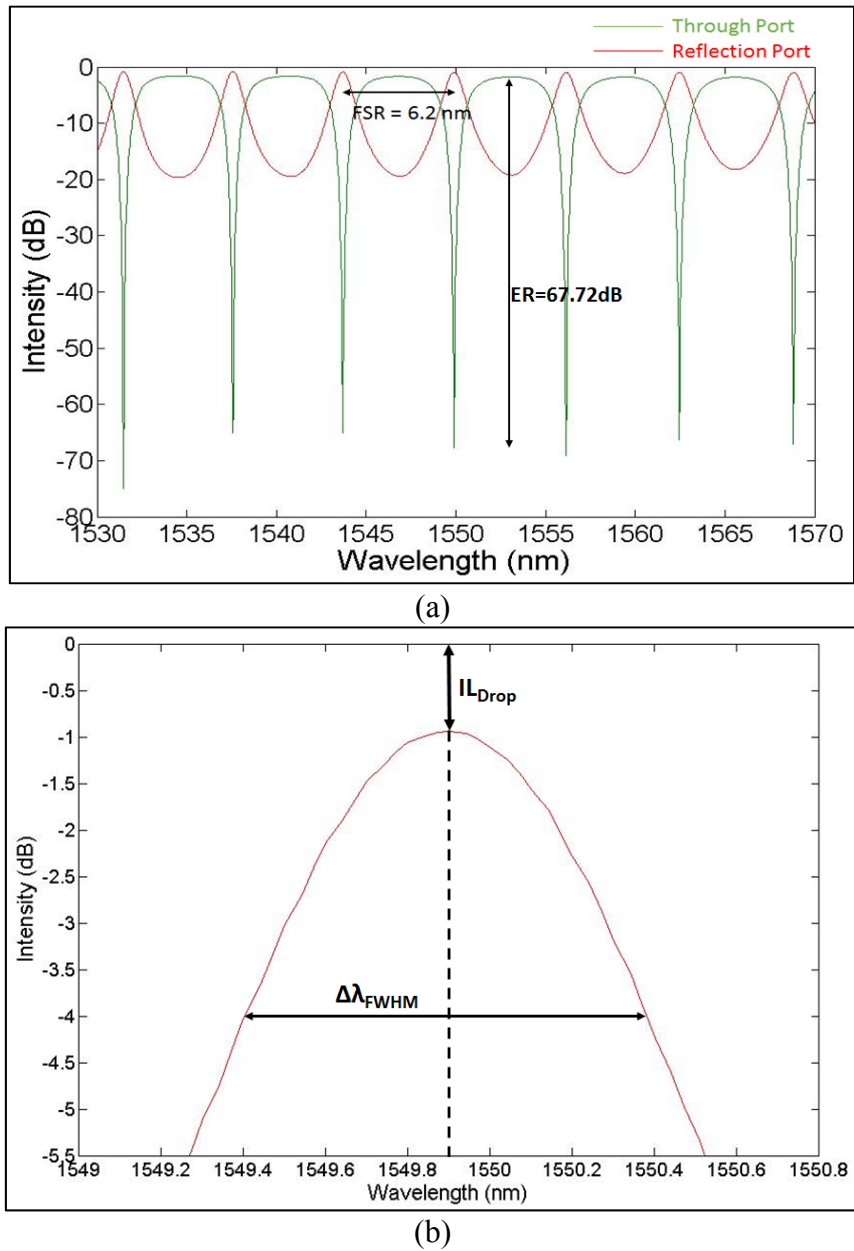


Figure 3.11 (a) Simulated spectral response of a silicon nitride single ring reflector, (b) zoom in of the resonance peak of the reflection/drop port response

3.2.4 Simulation of a Silicon Serially Coupled 3-Ring Reflector: The Vernier Effect

In order to design a silicon waveguide based a serially coupled 3-ring reflector as shown in Figure 3.2, single racetrack-resonators were designed and simulated initially with the goal to obtain a wide FSR and a narrow 3-dB bandwidth. Once the small ring resonators are designed having wide FSR, they are serially coupled and further modified by varying the coupling coefficients κ in order to achieve the optimized 3rd order ring reflector. The effective refractive indices and their corresponding group indices for a 440 nm wide and a 220 nm high waveguide are numerically calculated using the Eigenmode solver in Lumerical MODE. The waveguide geometry was chosen to ensure the single mode propagation for TE polarization, while still having low propagation losses. This Si waveguide has a 2 μm thick SiO_2 cladding above and below it. The calculated n_{eff} for the symmetric and the antiymmetric modes are 2.3504 and 2.3151 (as seen in Figure 3.6 (b)), respectively and their corresponding n_g are 4.2180 and 4.4650, respectively. To have a wide FSR, a minimum optical path length is required and therefore, small ring radiuses (r) (such as 3.2 μm , 3.6 μm and 4.3 μm) are considered and the design were simulated in the 2.5D-varFDTD simulator using the parameters which are presented below in Table 3.1. The total optical path length of ring1, ring2 and ring3 corresponding to ring radiuses 3.2 μm , 3.6 μm and 4.3 μm , respectively are 41.6 μm , 37.2 μm and 34.7 μm . As seen in the Table 3.1, the coupling coefficient (C) is kept constant along with

Table 3.1 Parameters of different RRs (based on Si waveguide) integrated with Y-splitters

	r (μm)	L_c (μm)	g (μm)	C
Ring 1	4.3	7.3	0.15	0.145
Ring 2	3.6	7.3	0.15	0.145
Ring 3	3.2	7.3	0.15	0.145

the coupling length (L_c) so as to have symmetrical couplers. The insertion loss of about 2 dB for the ring resonator (Zhang et al., 2013) and about 0.22 dB for the Y-splitters (Zhang et al., 2013) were included while performing the initial simulations. These loss values were in agreement with the simulated values using FDTD solver. The drop port spectra obtained from the 2.5-D FDTD simulation for each ring and there corresponding FSRs can be seen in the

Figure 3.12 over a large wavelength range with a common resonant peak around 1492 nm. The performance parameters corresponding to each ring are presented in Table 3.2 where the important attributes such as FSR, extinction ratio, Q-factor and 3-dB bandwidth are summarized.

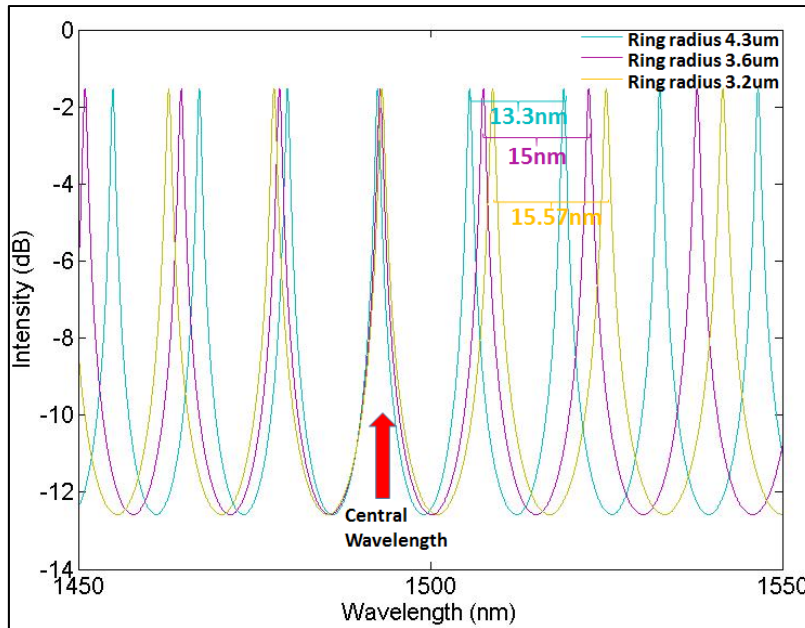


Figure 3.12 FSRs for three different ring reflectors, each of them showing a common central wavelength around ~ 1492 nm

Further, a serially coupled three ring reflector is simulated in a 2.5D-var FDTD solver using the design parameters mentioned in Table 3.1. The obtained reflection response shown in Figure 3.13 gives a FSR of ~ 20.6 nm between the adjacent resonant peaks. The obtained spectrum is not as expected, since the dominant resonant peaks which should show an extended FSR are not distinctive and also each resonance peak shows splitting. The peak splitting shows three peaks which is due to the cascading of three rings. The similar type of resonance peak splitting is observed in (Rubi Boeck et al., 2010) but with two peaks, where they have serially coupled two rings in order to demonstrate 2nd order ring filter.

Table 3.2 Attributes obtained for Si waveguide based three different ring reflectors

Ring Type	FSR (nm)	ER (dB)	Q-Factor	FWHM (nm)	λ_0 (nm)
$r=4.3 \mu\text{m}$	13.33	12.58	1243.75	1.2	1492.6
$r=3.6 \mu\text{m}$	15	12.58	1148.34	1.3	1492.8
$r=3.2 \mu\text{m}$	15.57	12.57	1066.5	1.4	1492.9

As discussed in (Robi Boeck et al., 2010), some of the factors must be ensured in order to achieve the optimized performance such as: (i) the removal of twin resonance peaks located in between the main resonance peaks, (ii) to make sure that the main resonance peak intensity is high (i.e. ensuring low insertion loss), (iii) there is a minimal splitting of the main resonance peak and (iv) there is a large interstitial peak suppression. Thus in order to optimize the device performance some design parameters were changed. As the total optical path length of the rings determines the extended FSR, so path lengths were carefully selected. Moreover, the power coupling factors also need to be optimized to obtain high main resonance peak intensity, minimal main resonance peak splitting and a large interstitial peak suppression (Schwelb, 2007) (Chaichuay et al., 2009) and thus, the field coupling coefficient ' κ ', the coupling gap ' g '

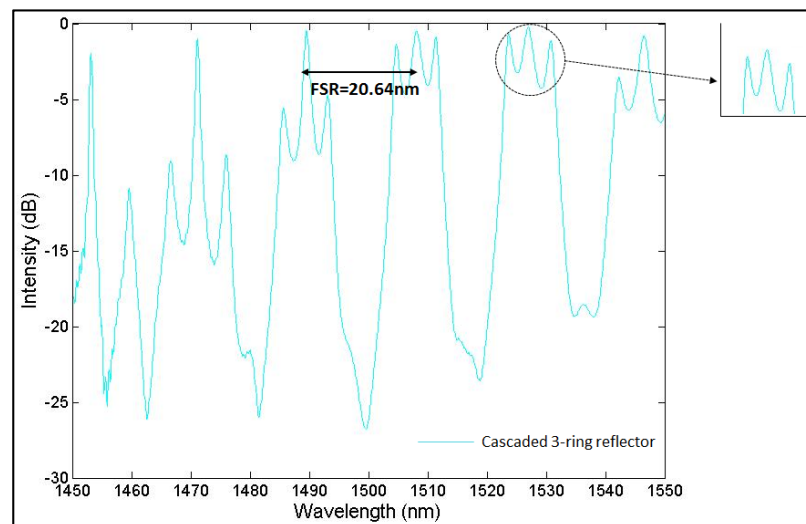
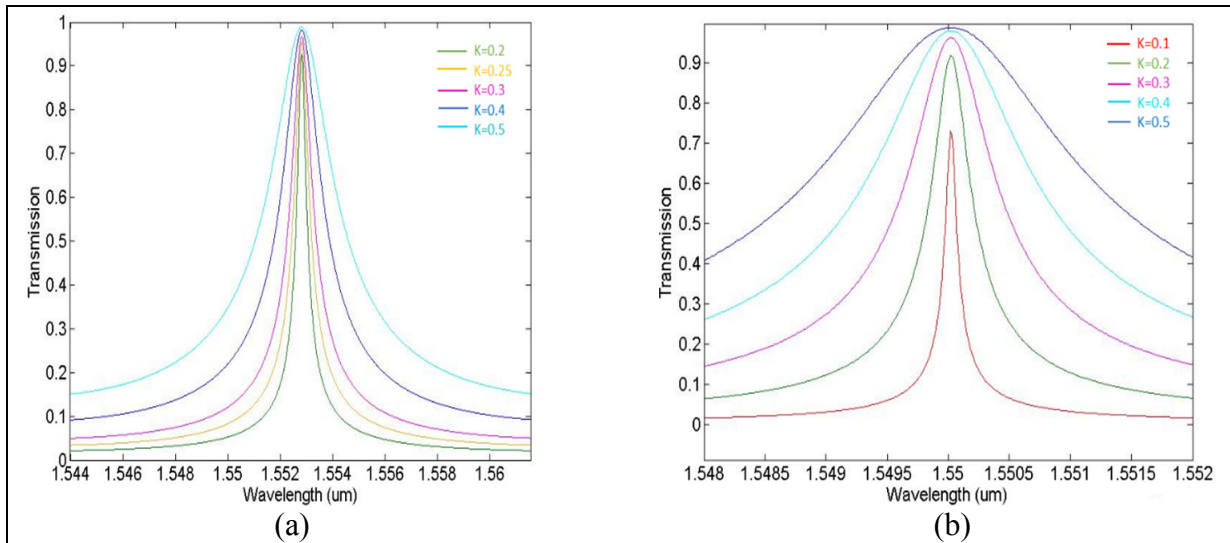


Figure 3.13 The reflection response of a serially coupled 3-ring reflector in a 2.5D-FDTD showing resonance peak splitting

and the coupling length ' L_c ' for each of the ring were changed. The ' κ ' for three rings was carefully chosen in order to have a critical coupling and a narrow 3-dB bandwidth using the analytical equations in MATLAB as shown in Appendix IV. This κ further determines the design parameters such as g and L_c using parameters in 2.5D-FDTD simulations to accurately design the ring reflectors. The selected radiuses for the individual ring resonators are $3.6 \mu\text{m}$, $10 \mu\text{m}$ and $4.3 \mu\text{m}$. According to equation (3.1), the extended FSR is related to the m (co-prime integer values) times the FSR of an individual ring and the m values are chosen to be 3, 5 and 7. Three plots in Figure 3.14 shows the effect of κ on the drop port intensity and its 3-dB bandwidth for three different rings, which is evaluated using the drop port transfer function equations in MATLAB. The selected parameters based on the optimum κ values are summarized in Table 3.3.



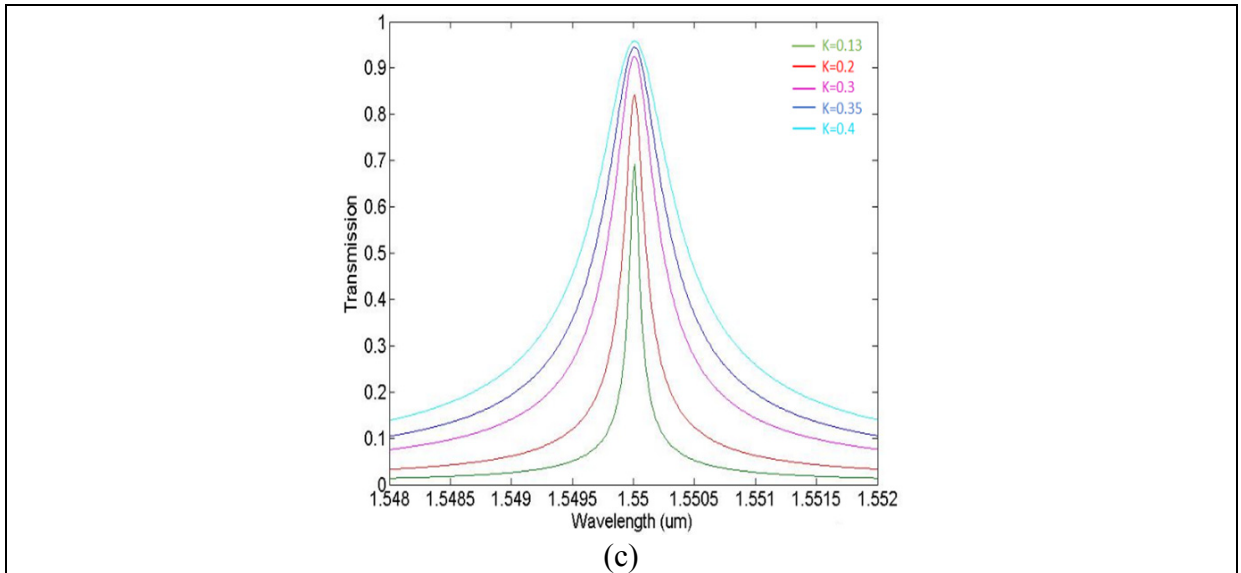


Figure 3.14 The effect of the coupling coefficient ' κ ' on the drop port peak intensity of Si waveguide based single ring resonator of radius (a) $3.6 \mu\text{m}$ (b) $4.3 \mu\text{m}$ and (c) $10 \mu\text{m}$

Table 3.3 Optimized design parameters for Si waveguide based three different single ring reflectors

	Radius (μm)	Coupling Length (μm)	Gap (μm)	Field Coupling Coefficient (κ)	Total Path Length of RR (μm)
Ring 1	3.6	2.6	0.15	0.145	27.81
Ring 2	10	1.59	0.18	0.137	66.01
Ring 3	4.3	2.007	0.15	0.145	31.03

The total optical path length of each ring is selected to target the desired resonant wavelength of $1.55 \mu\text{m}$. The coupling length for each ring resonator (RR) is assumed to be of straight parallel waveguides, excluding the bend region. The total optical path length for each of the ring resonator is presented in Table 3.3. The Y-splitters are designed to provide a 50:50 power splitting and are simulated in 2.5D-FDTD. The total transmission loss of the simulated Y-splitter is 0.17 dB. The reflection spectra for three different rings is shown in Figure 3.15 comparing there FSRs which are quiet high compared to previous designed RR's (as shown in Figure 3.12) and are centred around desired wavelength of 1550 nm. It shows high drop port peak intensities of around 94% of the total input light intensity. The other output performance

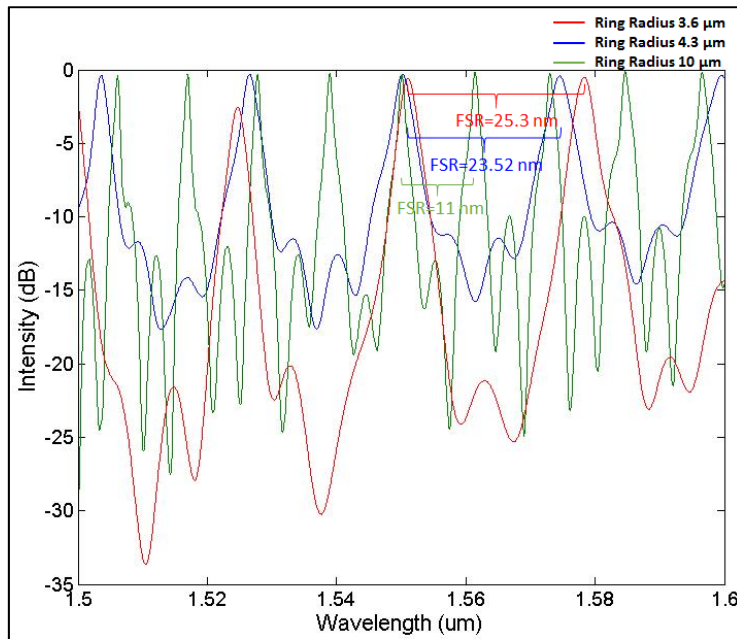


Figure 3.15 Reflection spectra obtained from 2.5D-FDTD for three different Si ring reflectors showing their corresponding FSRs

Table 3.4 Performance parameters for the optimized single Si ring reflectors

Ring Type	FSR (nm)	ER (dB)	Q-factor	FWHM (nm)	λ_0 (nm)
r=3.6μm	25.3	30.09	337	4.59	1550.89
r=10μm	11	19	1409	1.1	1550.07
r=4.3μm	23.52	17.56	500	3.1	1550.07

metrics such as ER, the Q-factor and the FWHM for three different ring reflectors are summarized in Table 3.4. The spectrum shows a high ER and a wide 3-dB bandwidth but the Q-factor obtained is low. This could be due to the over-coupling at the coupling region (i.e. $\kappa < \alpha$) which leads to a wider 3-dB bandwidth. Also, the propagation losses and the coupling losses within the device seems to be high leading to improper coupling which can be seen due to irregular lower region of the curves. Since, the bend radii selected are also small, to achieve wide FSR, so the losses due to bends also impacts the spectral peaks and thus the spectral response is not proper.

Finally, a cascaded 3-ring reflector is simulated using the optimized design parameters of three different ring-reflectors presented above (in Table 3.3) with an aim of achieving an extended FSR by an aid of exploring the Vernier effect. A quality optical spectrum showing the proper dominant resonant peaks with an extended FSR, the minimum peaks possible in-between the dominant resonant peaks and no main resonance peak splitting is expected. The whole structure is simulated using a 2.5-D variational FDTD mode solver. The obtained optical spectrum from the reflection port can be seen in Figure 3.16, showing an extended FSR of around 90.2 nm. We can clearly observe the two distinct dominant resonant peaks at 1428.8 nm and 1519 nm. Although the targeted wavelength was near 1550 nm but as seen in Figure 3.16 the resonant wavelengths of the rings have shifted. Also, the interstitial peak suppression is increased to 7.6

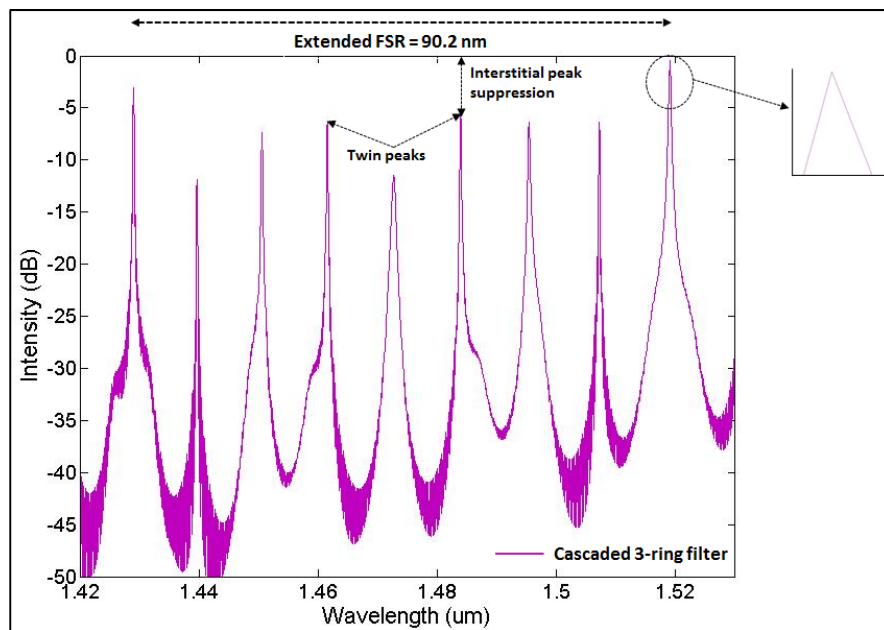


Figure 3.16 Reflection spectra for a serially coupled Si 3-ring filter illustrating the Vernier effect and showing the dominant resonant peak without peak splitting

dB in comparison to the previous response of 1.35 dB (in Figure 3.13). The obtained extended FSR of 90.2 nm is wide enough to cover the entire C or L-band (40 nm) as compared to any of the single ring reflectors presented above. We can clearly see that the peak splitting for the dominant resonant peaks has been resolved, as it was done in (Robi Boeck et al., 2010), in

comparison to the peaks observed earlier (in Figure 3.13). But the twin peaks still exist probably because the co-prime integer numbers m_1 , m_2 and m_3 , as mentioned in equation (3.1), for this design still need to be improved. To remove the occurrence of the twin peaks, m_2 should be equal to m_1-1 (assuming $m_1 > m_2$) and m_3 should be equal to m_2-1 (assuming $m_2 > m_3$). If the integer numbers increase, the interstitial peak suppression decreases and so they need to be small enough to give an adequate interstitial peak suppression. As the $\kappa < \alpha$ (as seen in Figure 3.15), the optimization of κ values will lead to a proper and smooth spectral response of an individual ring giving a narrow 3-dB bandwidths. Moreover, in order to decrease the resonant peak intensities in between the dominant resonant peaks, more optimization need to be done with respect to carefully choosing the co-prime integer multiple of FSRs and also by optimizing the κ which will be done in the future.

3.3 Fabrication, Measurements and Analysis

3.3.1. Mask Layout Description

The Si waveguide based cascaded ring reflector could not be fabricated at IME foundry within the given time frame due to the fab challenges and time constraints since the tools in the foundry were down for very long period. For the fabrication of a Si_3N_4 ring reflector, a single ring resonator is integrated with the Y-splitters, such that the Y-splitter branches form the bus waveguides as shown in Figure 3.8. The layout for the devices is made in the K-layout software. The total chip area is 1.5 cm x 2 cm. The mask dimensions for the straight and the curved waveguides is 435nm (wide) x 435 nm (height). The gap distance between the ring and the straight bus waveguide is kept at 700 nm and the total optical path length of the ring is 220.56 μm . No grating couplers or tapers are used at the end of the devices, allowing light to couple directly from the fibre to the waveguide edge facet. Considering fabrication constraints, few replicas of optimized ring-reflector designs along with the variation in the waveguide width and the coupling gaps have been incorporated within the chip. In total, there are 14 devices out of which devices 1-7 are the replicas of the final optimized design, designs 8-10 have waveguide width variations and designs 11-14 have varying coupling gaps. These several

design variations allow the possibility of achieving at-least one working device with the desired output spectral response as we expect at least one device to have a desired waveguide geometry.

3.3.2 Fabrication Process Flow for Si₃N₄ structures.

The different design variants developed through the simulation models are further processed for fabrication to understand their limitations and their optical response, using micro-fab techniques. These devices are fabricated in the various fab- and the clean room facilities across the Montreal region especially at McGill, Ecole-Polytechnic and National Institute of Scientific Research (INRS) universities. The SiN devices are deposited over the standard 8-inch silicon wafer. At first the Si wafer is cleansed using the chemical baths in order to remove the contaminants which may lead to a poor adhesion or a defect formation in the resist layer. The first layer deposited over Si substrate is the SiO₂ layer acting as a buried oxide (BOX) layer which is grown thermally. This is followed by the deposition of a SiN layer over a SiO₂ layer which is done using LPCVD technique which deposits Si-rich low stress SiN layer. This is further covered by the chromium (Cr) hard mask to have easy pattern transferring after dry-etch as Cr has high resistance to plasma etching. After that, the sample is made ready for the lithography step by adding an adhesion promoter such as hexamethyldisilazane (HMDS), which enhances the adhesion of the resist to the substrate. In the next step, a negative tone e-beam resist such as ma-N-2401 is spin coated over HMDS. Once the sample is ready for lithography, it is e-beam irradiated causing chemical changes in the exposed area which influence the solubility of the exposed area relative to the unexposed area of the resist in a developing solvent, thus leaving behind the SiN patterned structures. Then SiN layer along with the Cr hard mask and negative e-beam resist are etched using inductively coupled plasma (ICP) cryogenic reactive-ion-etching (RIE). After this, all of the Cr layer and negative resist which is left over the waveguide structures is removed leaving behind only SiN waveguides. Then at last, these waveguides are protected by depositing a SiO₂ cladding over the structures using the PECVD technique. The recipes associated with the microfabrication steps such as DRIE, e-beam lithography, LPCVD, PECVD, etc. are modified from time to time in order to

obtain an optimized process flow in collaboration with the fellow researchers and the clean room personals. Some of the dimensional issues of the devices have been addressed as and when needed through the efficient mix and match of the lithographic techniques. A general process flow for fabricating the Si_3N_4 waveguide structures over the standard Si wafer developed at various lab facilities is presented in the Figure 3.17:

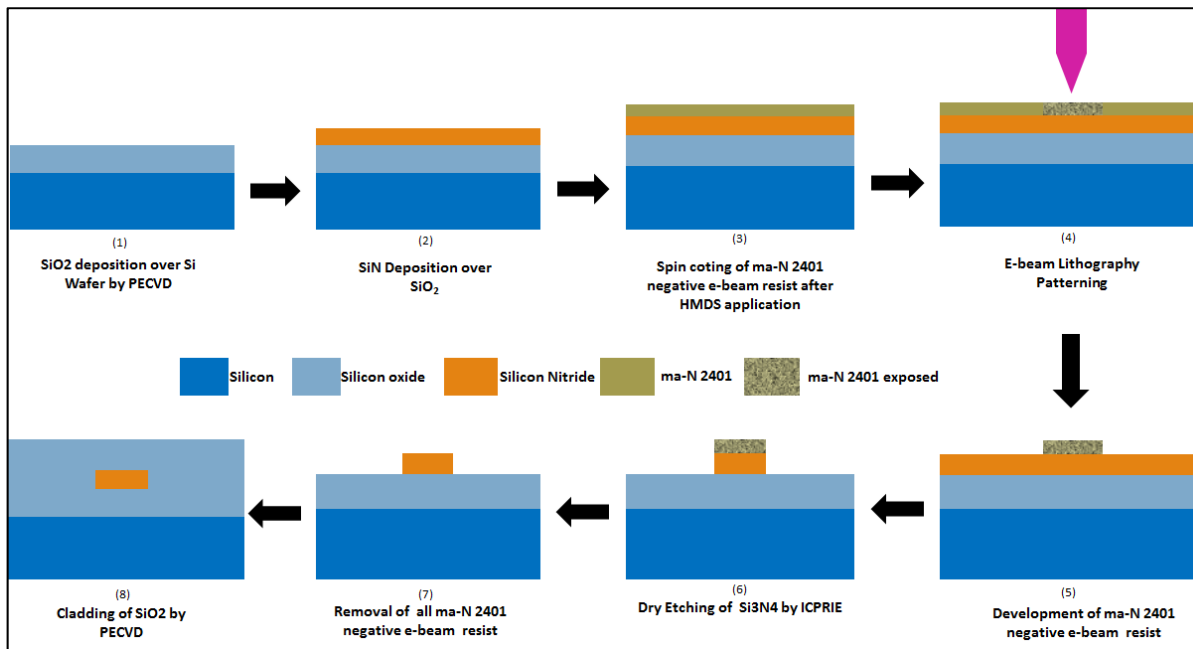


Figure 3.17 A generalised process flow for the fabrication of the Si_3N_4 waveguide structures.

3.3.3 Optical Test Setup

To take the measurements of the fabricated devices a setup with two optical fibres as shown in the Figure 3.18 (1) is used with the tapered lensed tips pointing towards each other such that the chip facet and both fibres are aligned at the straight axes without any angle inclination. Both input and the output fibres are single mode lensed fibre with a mode field diameter of around $3.3 \mu\text{m}$. The TE polarization is maintained for the input mode fibre using a polarization rotator (shown in figure 3.18 (6)). No grating couplers have been used for the fibre-to-waveguide coupling. Alignment of the fibres to the waveguide on the chip edge facet is

achieved with the help of a triple axis stage controller which is a NanoMaxTS purchased from the Thorlabs (shown in Figure 3.18 (5)). The chip containing the devices rest over the centre

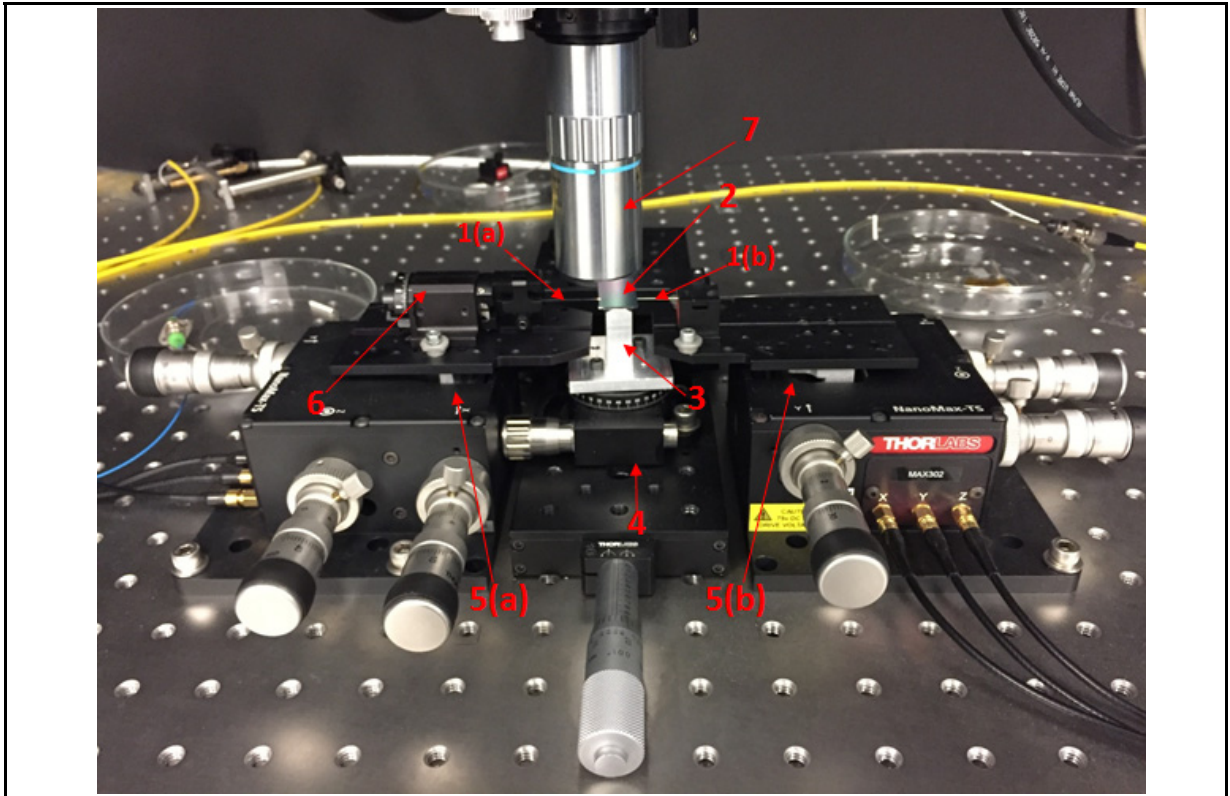


Figure 3.18 Optical Test Measurement Setup (1) (a) Single mode input fibre (b) Single mode output fibre (2) Device chip (3) Chip holding stage (4) Chip stage controller (5) Three axis stage controller for (a) input fibre (b) output fibre (6) Polarization rotator (7) Microscope

stage and on the other two stages lie the input and the output fibres. Also, the visible and infra-red cameras are used to achieve alignment via a microscope that is connected to a computer and are managed by Thorlabs and USB2.0-ARTCAM-008TNIR software, which visually displays on computer monitor. An optical power meter, of model N7744A purchased from the KEYSIGHT, is used to measure the optical power (in dBm) which is highly sensitive. A narrowband tunable laser source (model no.: 8168F) purchased from the KEYSIGHT-Agilent has a tuning range of 112 nm from 1480 nm to 1592 nm. The output spectra are measured using an optical spectrum analyzer (OSA), model no.: MS9710B which has a wavelength range from 0.6-1.75 μm .

An Optical Fiber Amplifier (AEDFA-33-B-FA) is used to send a broadband signal through the devices via an input polarization maintaining fiber. The device response is then measured by the OSA. The following procedure is followed to measure all the devices:

- a) The chip is aligned with the input and the output fibers with the help of a visible and an IR camera along with the microscope and the three axis stage controllers;
- b) Firstly, a broadband signal is sent through the devices and there output spectrum is measured in the OSA;
- c) Once output peaks are observed, then the broadband source is switched by the narrowband tunable laser source for better accuracy and to obtain sharp peak intensities with a better resolution;
- d) A tunable laser is set to an arbitrary wavelength;
- e) Some minor adjustments to the lateral positions of the fibers is done until a maximum intensity is achieved at the output;
- f) Then a sweep across the wavelengths is carried out to measure the maximum output power via an optical power meter;

3.3.4 Measurements and Analysis

The Si waveguide based cascaded ring reflector was not fabricated due to the fabrication challenges at the IME foundry and thus were not measured. Out of 14 devices on the chip containing SiN based ring-reflector designs, data is extracted only for devices 6, 8, and 9 because only 3 devices showed transmission response at the through port. For the remaining devices the spectral peaks are not observed at the through port nor at the reflected port. The reason for no output, at either of the ports, for the remaining devices could be due to the propagation losses within the waveguide, scattering losses due to waveguide surface roughness, bending losses at the bent junctions in Y-splitters and coupling losses at the coupling region of the ring and the bus waveguide due to fabrication discrepancies. The simulated waveguide width for the device 6, 8 and 9 are 435 nm, 445 nm and 455 nm, respectively. Thus, they are expected to show different peak response as the device output

spectrum is sensitive to the fabricated waveguide dimensions and the sidewall roughness. The measured transmission response for devices 6, 8 and 9 are shown in Figure 3.19 and the comparison of the transmission response between three devices can be seen in Figure 3.20,

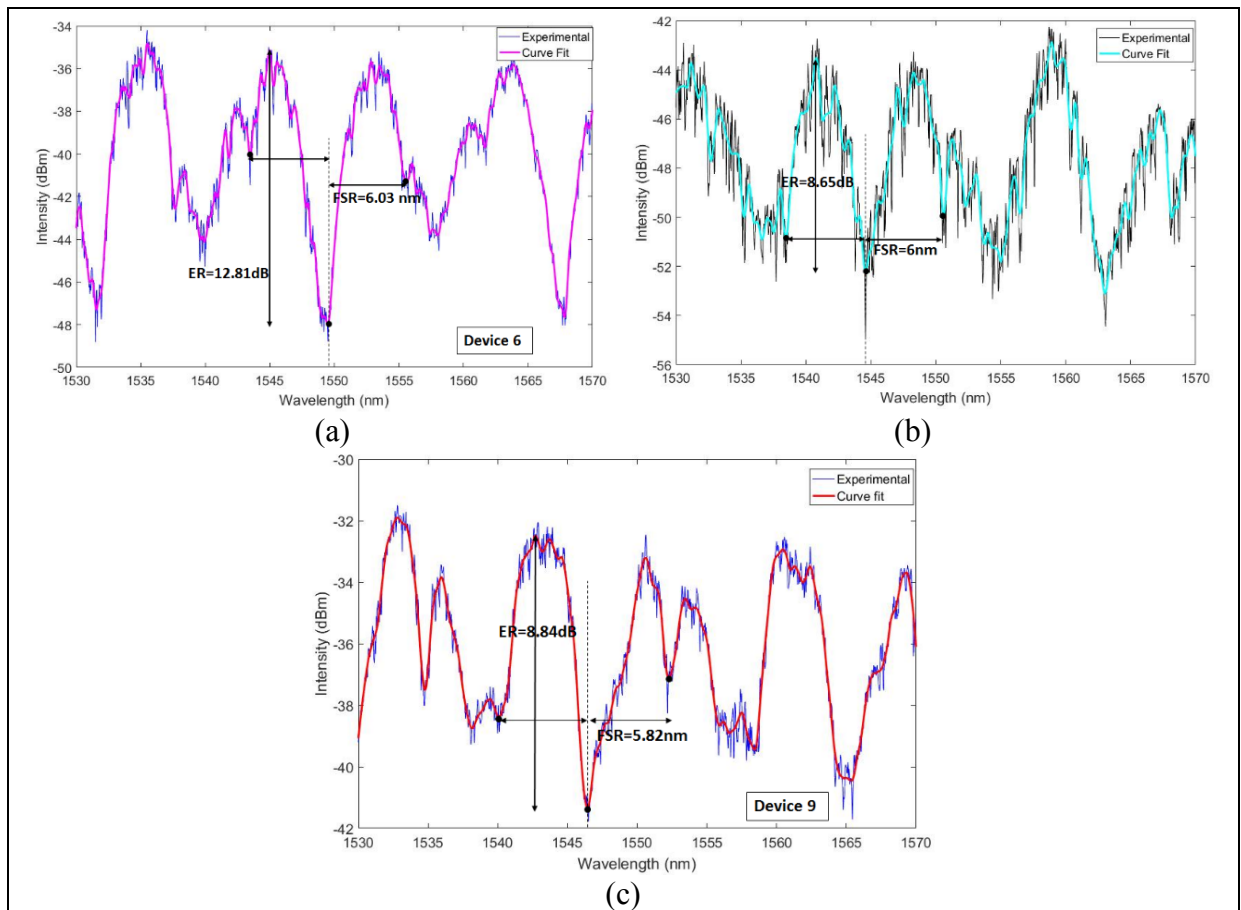


Figure 3.19 The through port transmission response for (a) Device 6, (b) Device 8 & (c) Device 9

which clearly shows a shift in the resonant peaks. For device 6, the observed resonant wavelength is at 1549.5 nm which is off by 0.5 nm from the targeted wavelength giving an FSR of ~ 6.03 nm. This FSR value is 0.17 nm off from the desired value of 6.24 nm. For device 8, the resonant wavelength nearest to the target wavelength is obtained at 1550.58 nm at an offset of 0.58 nm. The obtained FSR for device 8 is around ~ 6 nm which is off from the desired value by 0.24 nm. Similarly, for device 9, the observed resonant wavelength is at 1546.44 nm which is offset from the targeted wavelength by 3.56 nm. It gives a FSR of ~ 5.82 nm which is

less than the desired value by 0.42 nm. The important attributes obtained from the measurements characterizing device performance are illustrated in the Table 3.5.

The reflection spectrum is not presented as no response is obtained at the reflected port which could be due to the coupling losses, waveguide propagation and scattering losses and also the losses induced due to the circulator which is attached to the input fiber for measuring the reflection. Due to this reason only the through port response is presented. The comparison between the theoretical and the experimental transmission response is presented in Figure 3.21 where we can clearly see that the targeted resonant wavelength for the simulated response is 1550 nm. The measured response for the devices are slightly off from the simulated one and the FSR's obtained are in close proximity to the theoretical FSR of 6.2 nm. Out of three, device 6 gives the lowest 3-dB bandwidth and thus gives the highest Q-factor. Also the extinction ratio is around 12.81 dB which is good enough to be used in the DWDM applications. The device 8 and 9 shows an ER of around 8.5 dB but has a poor Q-factor and a 3-dB bandwidth. The output performance of these measured devices is not very well in accordance with the simulated designs and we can see some shift in the output metrics. A detailed analysis of the waveguide dimensional factors leading to such a performance is discussed next. Some other possibilities could be the inclusion of the lower value of waveguide losses while designing and simulation leading to the scattering of light and the propagation losses.

Table 3.5 Important attributes illustrating fabricated device performance

Device Type	FSR (nm)	ER (dB)	Q- factor	FWHM (nm)	λ_0 (nm)
Device 6	6.03	12.81	1122.82	1.38	1549.5
Device 8	6	8.65	660	2.34	1544.62
Device 9	5.82	8.84	678.26	2.28	1546.44

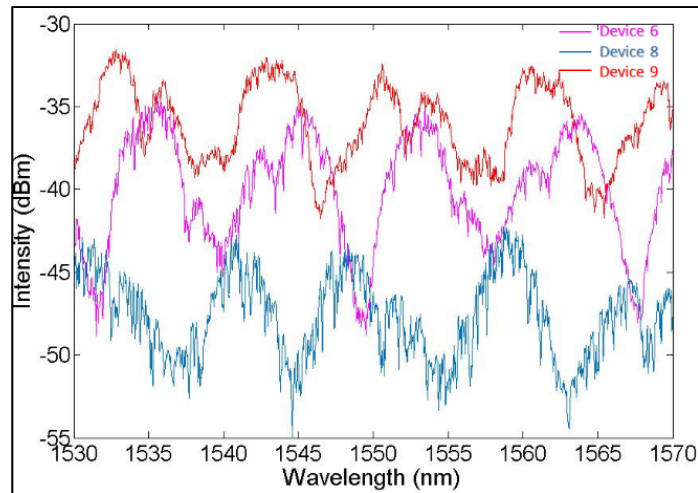
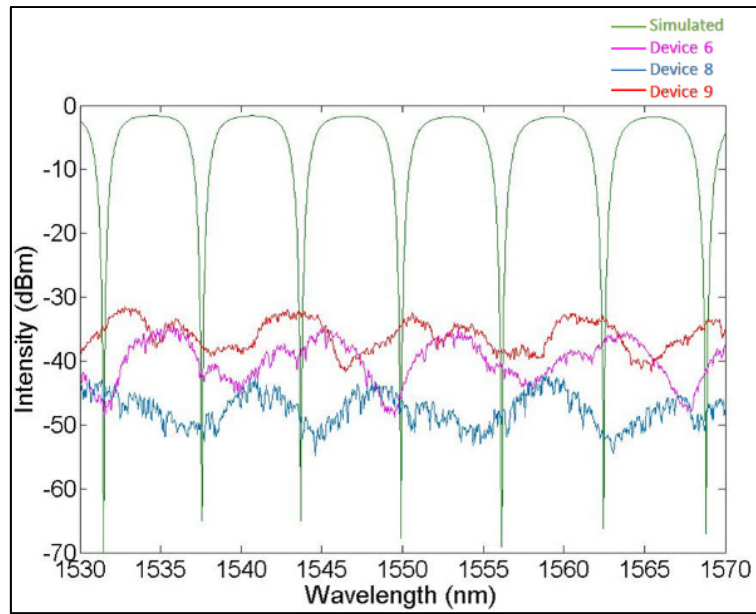
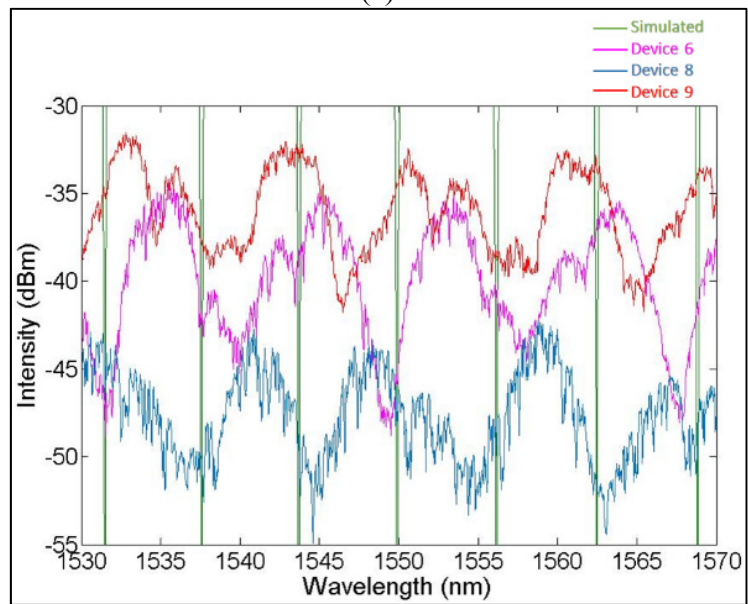


Figure 3.20 Comparison of the through port transmission response for 3 devices.

This difference in the FSR could be due to the variation in the expected waveguide width of 435 nm and the actual waveguide width. A SEM image of other device on the same chip is shown in Figure 3.22 which presents a top width of 386 nm and the bottom width of 427 nm with a thickness of 453.6 nm in comparison to the actual 435 nm x 435 nm design. The average width comes out to be 406 nm which is reduced by almost 30 nm from the actual dimension and the thickness has also increased by 5% of the actual dimension. Moreover, both of the coupling gaps measured are off by approximately 40 nm which leads to under-coupling. The discrepancy analysis of the fab dimensions for some devices on the chip shows that the waveguides are over-etched and is expected to be followed for the rest of the devices on the same chip. The effect of the fabrication on the device performance can be analysed from the Figure 3.23 which shows normalized curves for three devices having different widths and comparing their simulated and the experimental response. From the plots in Figure 3.23, we can infer that as the waveguide width increases (435 nm > 445 nm > 455 nm) for the devices, their corresponding FSRs decreases (6.03 nm > 6 nm > 5.82 nm). This



(a)



(b)

Figure 3.21 (a) Theoretical vs Experimental through port response for devices 6, 8 and 9 (b) Zoomed in response of plot (a)

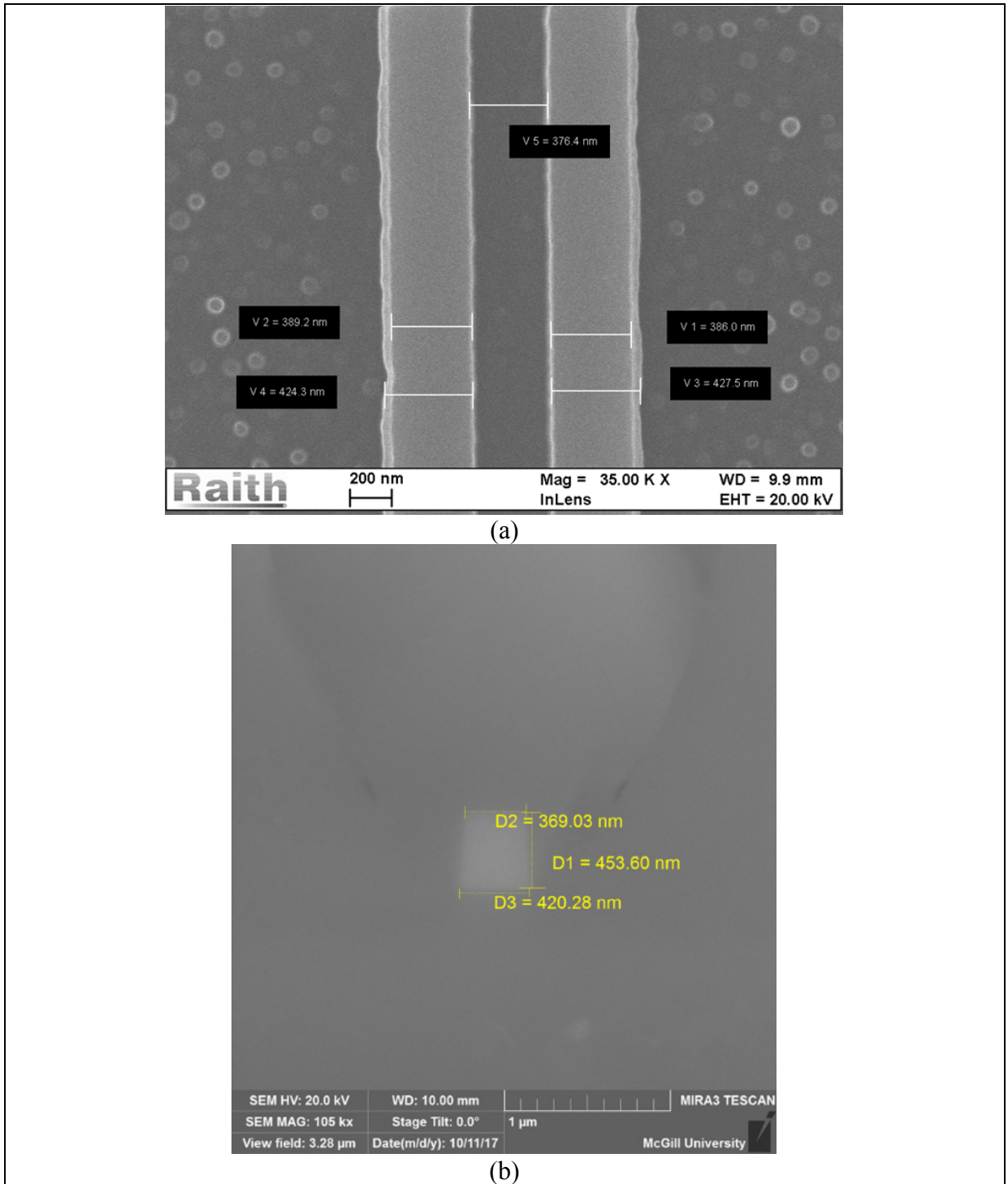


Figure 3.22 SEM image of the (a) fabricated waveguides forming the coupling region and (b) the cross section of the waveguide.

holds true theoretically, since as the waveguide width increases, the effective refractive index of the waveguide increases (Figure 3.5) and so does the group index and thus the FSR is expected to decrease (from eqn. 2.20 and 2.21). Also, the resonant wavelength (or the targeted wavelength) has been shifted to the left (i.e. it has reduced) for all of the devices as discussed above which holds true theoretically, since λ_r reduces as the n_{eff} of the waveguide reduces due to the decrease in the waveguide width (eqn. 2.1). The thickness of the waveguide also plays a major role in guiding the mode propagation in a confined manner. The waveguide allows guided wave propagation only if the thickness is greater than the critical cut-off thickness for each waveguide mode. If the thickness of the waveguide is below the cut-off thickness than the light is no longer confined in the waveguide and it begins to leak into the substrate. Thus, the thickness of the waveguide also determines the guiding modes in the waveguide (Gang, 2005) and is considered to be an important factor in deciding the output performance of the devices. The thickness of a silicon nitride waveguide used in designing a ring reflector is optimum for guiding a lowest order TE mode. The cut-off thickness for a three-layer waveguide structure ($n_{subs} = 1.45$, $n_{core} = 2.0458$, $n_{clad} = 1.45$) at a wavelength of 1550 nm is shown in Table 3.6. The cut-off thickness is evaluated using a MATLAB code shown in Appendix V. For only the lowest order TE mode to propagate inside the waveguide, the thickness must be less than 537 nm. The thickness of the fabricated waveguide is approximately ~453 nm and so it is well within the cut-off range of the first order TE mode. A plot in Figure 3.24 shows the tolerance of the waveguide's n_{eff} due to the change in the waveguide thickness and the waveguide width for the fabricated waveguide dimensions.

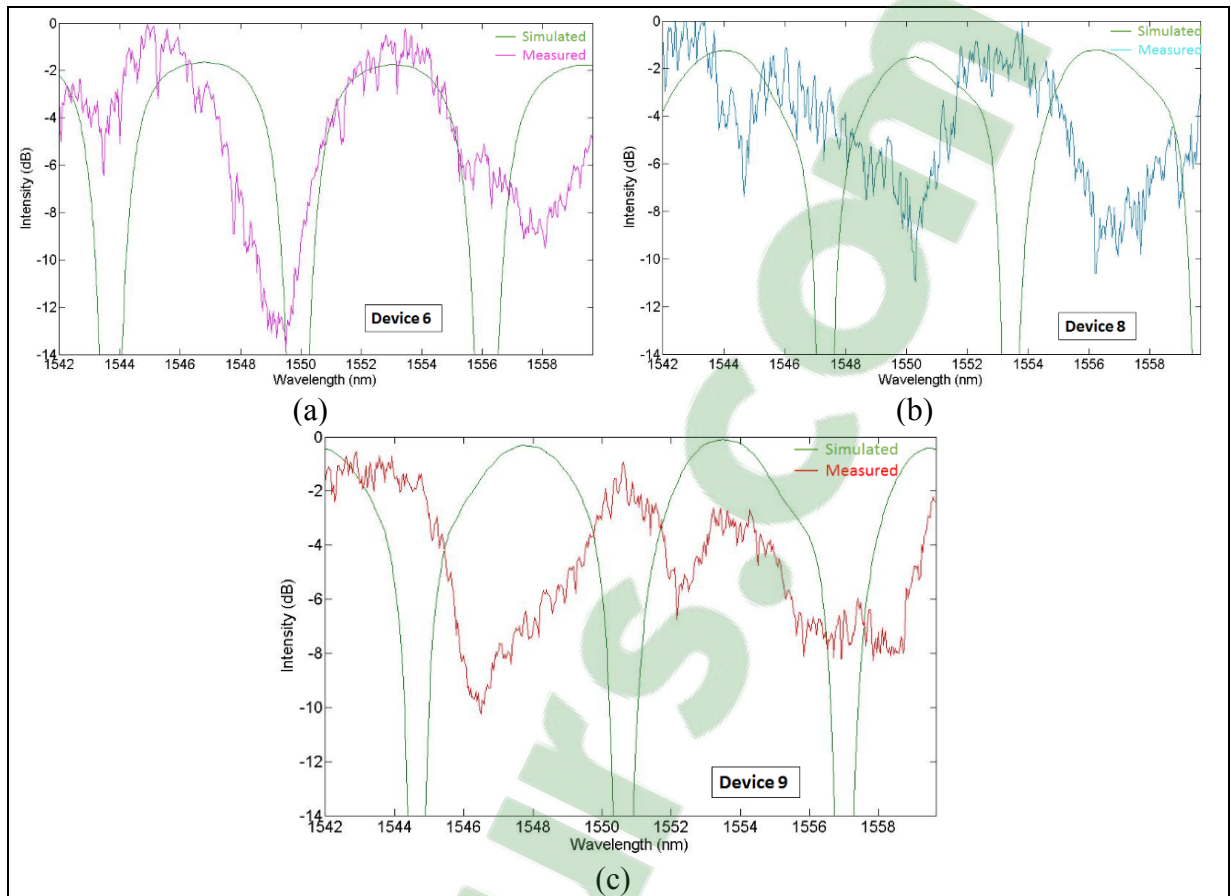


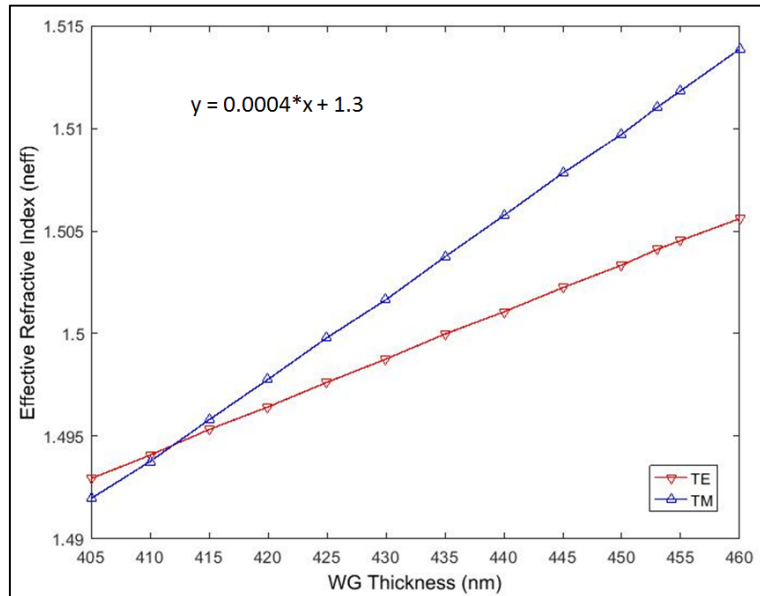
Figure 3.23 Normalized curve showing theoretical vs experimental response for varying widths (a) Device 6 (435 nm) (b) Device 8 (445 nm) (c) Device 9 (455 nm)

Table 3.6 Cut-off thickness for the waveguide structure

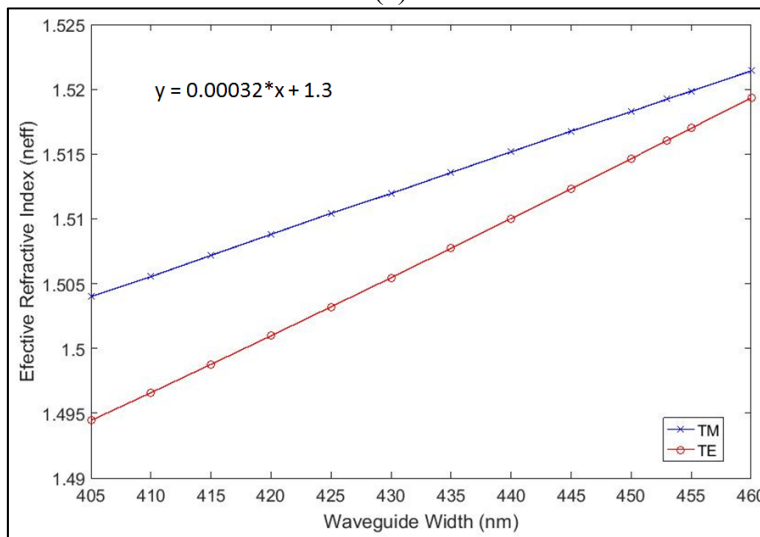
TE Modes	Cut-off thickness (μm)
0	0
1	0.537
2	1.07
3	1.62
4	2.148
5	2.685

The measured FSR of each device should be higher than the theoretical value since the waveguide width has reduced (thereby reducing the n_{eff} and n_g), but that is not the case. This shows that there are some other factors related to the n_{eff} or n_g , which plays an important role

in deciding the FSR. One of the factors could be the thickness of the waveguide as discussed in (Gang, 2005). A change in the thickness of the waveguide seems to have more impact on



(a)



(b)

Figure 3.24 The effect on the n_{eff} of the fundamental TE and TM mode for the (a) Fabricated waveguide width (386 μm top x 427 bottom) vs. the varying waveguide thickness and (b) Fabricated waveguide thickness of 453 μm vs. the varying waveguide width.

the device performance as compared to the change in the width of the waveguide which can be seen from the plots in Figure 3.24. If the waveguide width is kept constant (as fabricated)

and the waveguide thickness is varied, then the effect on the n_{eff} of fundamental TE and TM modes can be seen in plot (a) of Figure 3.24. Whereas, the effect on the n_{eff} of fundamental TE and TM mode due to the variation in the width when the thickness is fixed at 453.6 nm can be seen in plot (b) of Figure 3.24. The linear curve fit of data in both the plots show that the slope of the TM mode is higher in plot (a) as compared to the slope of the TM mode in plot (b) of Figure 3.24. Thus, the n_{eff} is more sensitive to the change of the waveguide thickness than the width of the waveguide. To mitigate this fabrication variation, the iterations based on the simulation and fabrication data will be done in the future, achieving the n_{eff} in the close proximity to the desired one, and thus, giving the desired output performance of the devices.

3.4 Summary

To summarize, we have demonstrated a single ring reflector based on a Si_3N_4 waveguide. It uses a racetrack resonator with a 35 μm radius connected to a Y-splitter and a combiner forming a reflector configuration. One out of three devices, device 6 shows an extinction ratio of 12.81 dB with the resonant wavelength at 1549.5 nm, which is in close approximation to the targeted wavelength of 1550 nm. The measured FSR of the fabricated device is 6.03 nm. The obtained 3-dB bandwidth of the resonant peak is 1.38 nm giving a Q-factor of 1122.82. In future, a serially coupled 3-ring reflector, based on a silicon nitride waveguide, will be developed with a target of achieving an extended FSR wide enough to cover the entire C or L-band spectrum. The other reflector type is a 3-ring reflector cascaded in series, designed using a silicon waveguide. This ring reflector is theoretically designed showing an extended FSR of 90.2 nm which is wide enough to cover the entire C or L-band (40 nm), in comparison to a single ring reflector by using Vernier effect. It shows an interstitial peak suppression of 7.6 dB with no dominant resonance peak splitting. Further, the twin peaks need to be removed by the careful selection of an integer multiple of FSR (m) and also by choosing the accurate coupling coefficient κ , which will be done in the future. These devices propose an optical 3rd order ring filter that is promising for a wavelength channel selection system in a tunable laser, tuned via MEMS actuator.

CHAPTER 4

RACETRACK RESONATOR FOR THE CHIRPED MODULATED LASER

Over the past decade, there has been a tremendous growth in the data services due to the large files downloading, online streaming, high definition televisions and massive multiplayer online games, resulting in the upgradation of the access networks. In the current market, upgrading the metro systems capacity from 2.5 to 10 Gb/s is the prime interest for most of the carrier operators, without adding costly dispersion-compensation modules (DCMs). The International Telecommunication Union (ITU) recommendation ("40-Gigabit-capable passive optical networks 2 (NG-PON2): Physical media dependent (PMD) layer specification ", 2014) specifies the physical media dependent (PMD) layer requirements for a passive optical network (PON) system with a nominal aggregate capacity of 40 Gbit/s in the downstream direction and 10 Gbit/s in the upstream direction, which is referred to as the next generation passive optical network stage 2 (NG-PON2). NG-PON2 is basically a flexible optical fibre access network which is capable of supporting the bandwidth requirements of mobile backhaul, business and residential services. Four (4) x 10 Gb/s time and wavelength division multiplexing (TWDM) was proposed to address the increasing bandwidth demand as part of the NG-PON2 (Kazovsky et al., 2007). Due to this advancement in the technology, the 10 Gb/s-transmitters were developed which necessitates innovative but also cost-effective and compact solutions providing long reach transmission (>60 Km) and high extinction ratio (>10 dB).

Among the solutions considered for achieving the high extinction ratio (ER) and the long range transmissions, the externally modulated lasers (EML) is one key example. The other attractive and widely used candidate is the directly modulated lasers (DML) which is low cost, consumes low electrical power and provide high output optical power. Although the signal generated with the direct modulation is considered to be robust as the output power of the device directly depends on input drive current, but is severely distorted (shown in Figure 4.1) during the fiber transmission because of the inherent chirp of the DML. At high bit rates, direct modulation generates frequency chirp that interacts with chromatic dispersion in the fiber thereby limiting

the range of the transmission and making it difficult to achieve a high ER. Chirp is the time dependence of the instantaneous frequency of an optical pulse which basically occurs due to the change in the refractive index associated with the change in the carrier density (Paschotta). Up-chirp means that the instantaneous frequency rises with the time, whereas down-chirp means that the instantaneous frequency decreases with the time. The chirp manifests in primarily 2 manners when a semiconductor laser is directly modulated: -

- a) Chirp which occurs at the bit transitions is known as transient chirp.
- b) Chirp that causes '1' bits to blue shift relative to the '0' bits is known as adiabatic chirp.

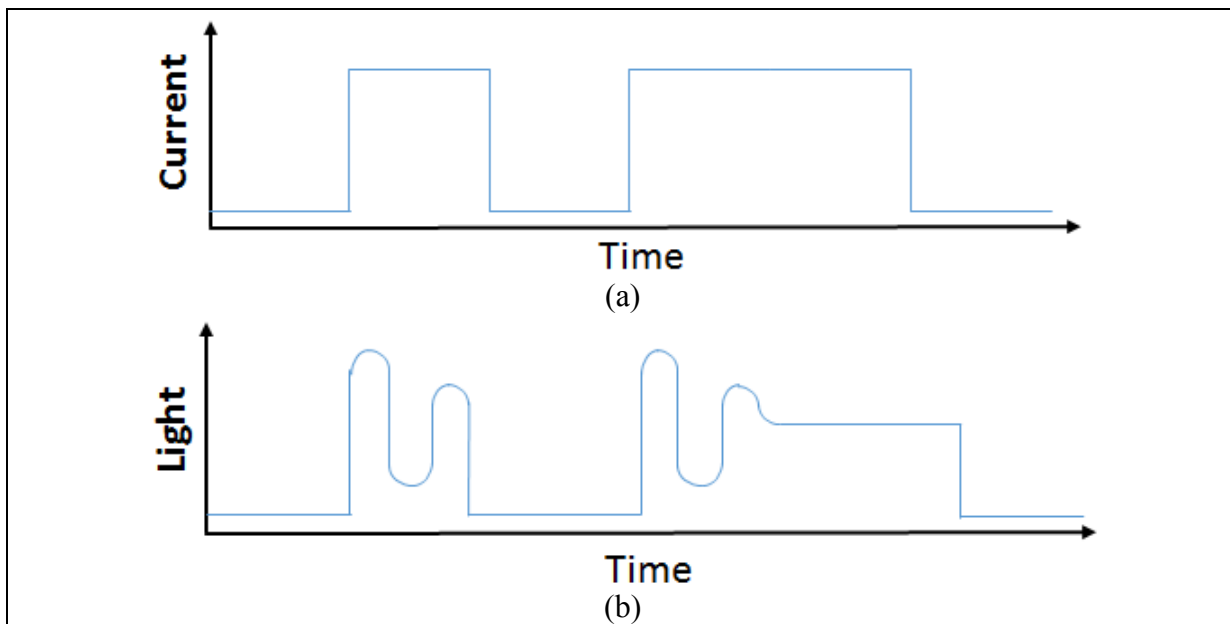


Figure 4.1 (a) Electrical signal at the input, and a distorted (b) optical signal at the output, of a DML due to chirp

The principle of any semiconductor laser or DML is based on modulating the bias current upto the threshold value (I_{th}) to modulate the laser. The increase in the bias current increases the number of charge carriers in the active region thereby leading to the reduction in the refractive index which in turn reduces the instantaneous frequency (ω_{inst}). This is known as a positive chirp or blue shift of ω_{inst} which is on the rising edge. If bias current decreases, then carrier density decreases thereby increasing the refractive index and thus increasing the ω_{inst} which is

known as negative chirp. It is on the falling edge of the frequency (J. Liu & Kobayashi, 2010). This positive and negative chirp of the frequency can be seen in the following Figure 4.2.

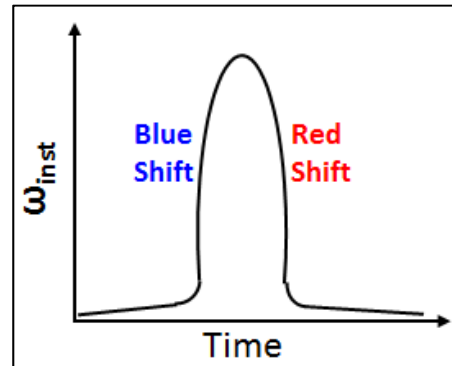


Figure 4.2 Change of instantaneous frequency ω_{inst} with time showing blue and red shift

Some of the solutions to overcome the challenge of chirp are dispersion compensating fiber (Mizuhara, Nguyen, Tzeng, & Yeates, 1995), spectral broadening reduction (Binder & Kohn, 1994) or electronic dispersion compensation (Feuer, Huang, Woodward, Coskun, & Boroditsky, 2003) and specific optical filtering (Wedding, 1992) (Morton et al., 1996). Many directly modulated distributed feedback (DFB) lasers operating at 10 Gb/s have been demonstrated and being used in the optical fiber and the telecom industry ("40-Gigabit-capable passive optical networks 2 (NG-PON2): Physical media dependent (PMD) layer specification", 2014), but they lack the rapid tunability required for the latest NG-PON2 standard. The DFB lasers required in NG-PON2 will be used in the burst mode for TWDM and point-to-point WDM. One approach to implement a tunable DML is to design the DBR laser in such a way that it can be tuned electrically and independently from the laser gain. However, due to the inherent chirp of the DMLs, the signal reach of the transmitters is limited. In order to mitigate these problems, chirp managed directly modulated laser (CML) came into existence and are considered as a breakthrough technology for the rapid tunability required by the NG-PON2. The CML is an alternative transmitter technology using an external filter in front of the DML to attenuate the laser signal transmitting data '0' bits and allowing only data '1' bits signals to pass through, which significantly increases the ER and thereby extending the reach of the signals.

In particular, a CML transmitting over 200 km at 1550 nm was demonstrated (Matsui et al., 2006) but at the expense of a complex wavelength algorithm to suppress the time dependent chirp and the use of the relatively bulky etalon filter, which increases the cost. A DFB laser with a microring resonator (MRR) (Gallet et al., 2016) (Chimot et al., 2016) as an external filter has been demonstrated. The MRR as an optical filter along with the DFB laser has been implemented either in silicon photonics (Gallet et al., 2016) or in III-V semiconductor materials such as indium phosphide (InP) (Chimot et al., 2016). Here, we demonstrate a MRR made with silicon nitride (SiN) waveguides using a CMOS compatible process as a potential external filter to be used along with the tunable laser. The tunable laser used for developing tunable CMLs will have a chirp of 10-30 GHz. The filter type we demonstrate has advantages such as compactness and cost effectiveness since we use a Si₃N₄ racetrack resonator. This optical filter will be used in future as an optical spectrum reshaper (OSR) in order to build a transmitter for the NG-PON2 channel grid. The low propagation losses of SiN waveguides enable the implementation of a large but an efficient MRR having a FSR that matches the ITU (ITU-T G.989.2, 2014) network grid of 100 GHz (0.8 nm) spacing in optical frequency. Thus, it is possible to address all the channels with a single MRR. We compare and demonstrate two MRR designs: a small ring with a FSR seven times wider than the required ITU channel grid of 100 GHz and a large ring with a FSR in close proximity to the required channel grid spacing. Hence a tunable transmitter can be implemented by combining several small rings or with only one large ring.

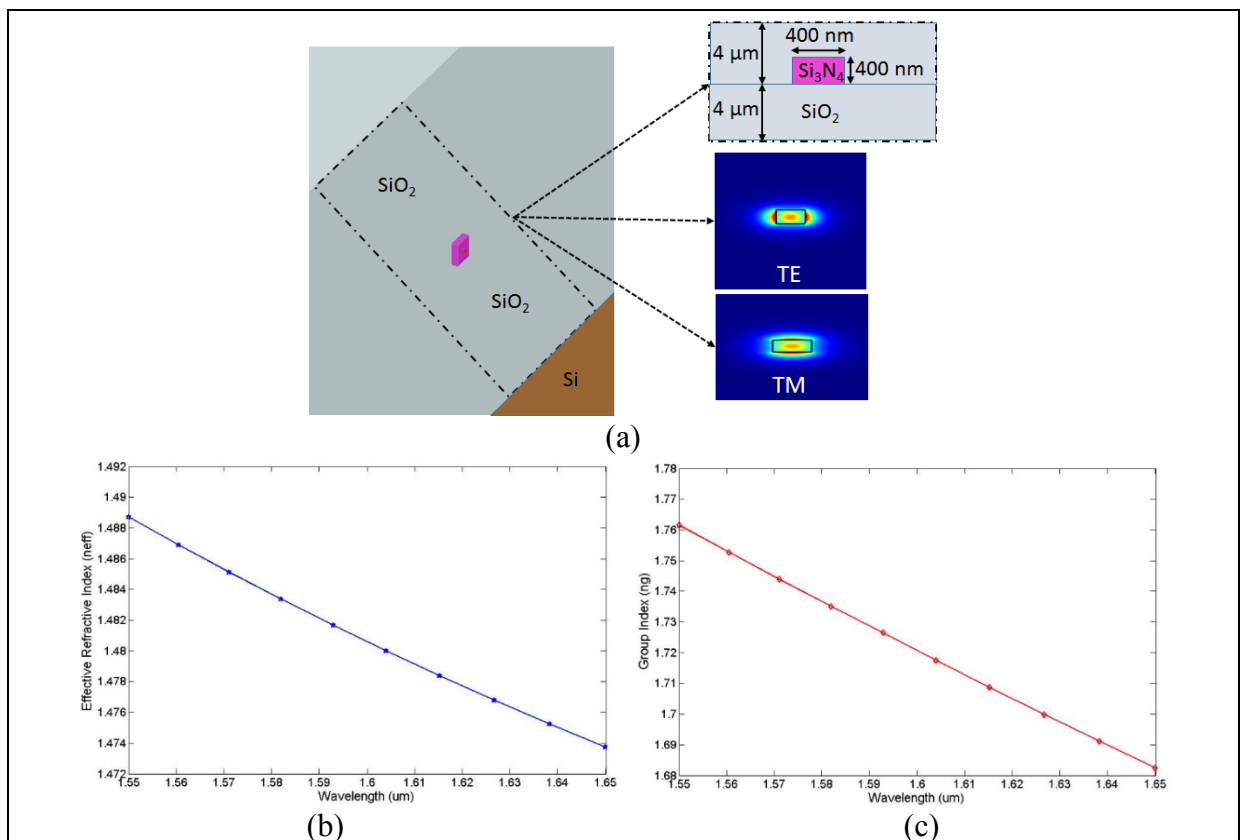
4.1 Small 4-port add-drop racetrack resonator

4.1.1 Design, Simulation and Optimization

With the goal of designing an economically viable ring filter for the CML, a low-loss SiN waveguide based compact racetrack-resonator is demonstrated. A square SiN waveguide with dimensions of 400 nm (width) x 400 nm (height) is used. These dimensions provide a good confinement of the light and are selected as per the fabrication recipe of our industrial partner.

These ring-resonators are fabricated over a standard Si-wafer where the SiN structures are deposited over a 4 μm thick SiO₂ BOX layer and covered with a 4 μm thick SiO₂ clad over it. At a wavelength of 1550 nm, the refractive index of the SiN is considered to be 2.0458 and for the SiO₂ is 1.45. The effective refractive index ' n_{eff} ' and the group index ' n_g ' are evaluated using the Eigenmode solver in Lumerical MODE via FDE method. The calculated n_{eff} for the fundamental TE and TM modes are 1.488701 and 1.488146, respectively. Whereas, their corresponding group indices n_g are 1.761564 and 1.7713, respectively. The n_{eff} and the n_g dependence on wavelength can be seen in Figure 4.3, which shows that at higher wavelengths, n_{eff} and n_g decreases.

The waveguide fabrication tolerance can be studied from Figure 4.4, where we can see the effect of changing the width and the thickness of the waveguide over the n_{eff} . This helps in understanding the fabrication sensitivity of the waveguide and its impact on device performance. If the thickness of the waveguide is fixed at 400 nm and the waveguide width is



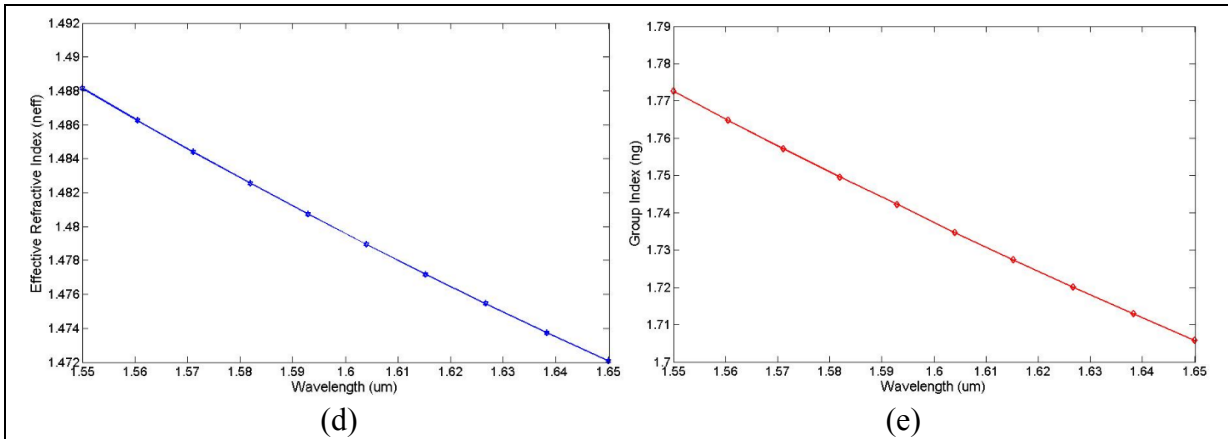


Figure 4.3 (a) Perspective view of a Si_3N_4 channel waveguide with insets showing the cross-section waveguide geometry and fundamental TE & TM mode distribution; (b) Wavelength dependent effective index for TE mode (c) Wavelength dependent group index for TE mode (d) Wavelength dependent effective index for TM mode (e) Wavelength dependent group index for TM mode

varied (Figure 4.4 (a)), then below 228 nm or above 398 nm, the mode with higher n_{eff} will be TE mode. If the waveguide width is selected in between the above-mentioned range, then the TM mode has higher n_{eff} . On the other hand, if the waveguide width is fixed at 400 nm and the thickness varies (Figure 4.4 (b)), then after 404 nm the TM mode has higher n_{eff} than TE mode.

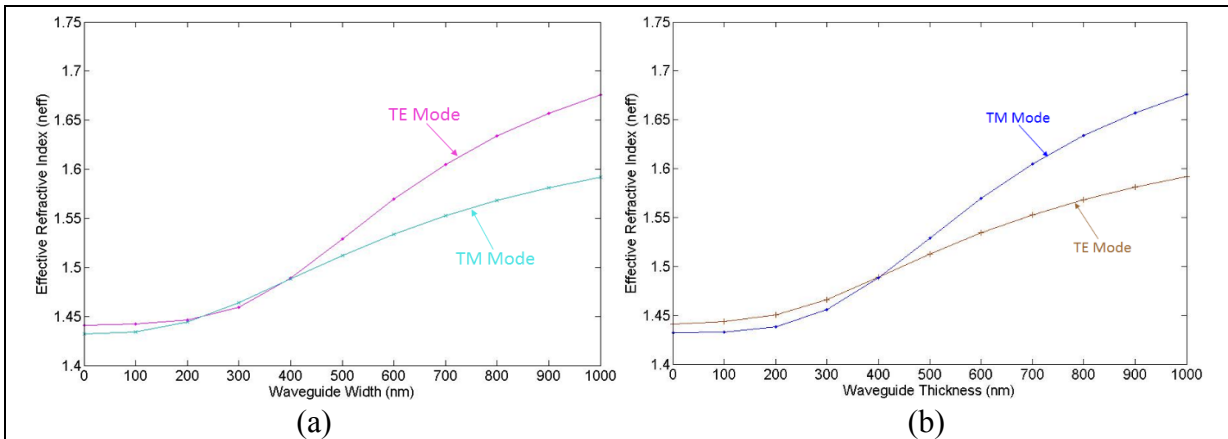


Figure 4.4 The fabrication tolerance showing the change in the n_{eff} of fundamental TE and TM mode at 1550 nm due to (a) variation in the width (fixed thickness at 400 nm) (b) variation in the thickness (fixed width at 400 nm)

Whereas, below this thickness, TE mode has higher n_{eff} than TM mode. Also, if waveguide width or thickness is chosen to be below 180 nm then modes are no longer confined within the waveguide and they tend to diffuse inside cladding. This change in the n_{eff} of the fundamental mode due to the change in the waveguide dimensions allows us to study the impact on output performance metrics of the device such as FSR, 3-dB bandwidth and Q-factor.

To design the racetrack-resonators, the design parameters were selected on the basis of the supermode analysis as discussed in section 2.1. The first two eigenmodes of the directional coupler are evaluated using a finite element mode solver in Lumerical MODE. An optimum field coupling coefficient κ is chosen so as to have the critical coupling condition. A selection of κ is done using a MATLAB code for designing an add-drop ring resonator (shown in Appendix IV). The optimum κ value helps in deciding the other design parameters such as the coupling gap and the coupling length. The coupling length considered here is simply the length of the two identical parallel waveguides. As the value of κ changes, accordingly the coupling gap also changes which determines the optimum coupling condition at the coupling region. The dependence of κ over the coupling gaps can be seen in Figure 4.5 for different coupling lengths of 5 μm , 10 μm , 15 μm and 20 μm for a waveguide of dimensions 400 nm x 400 nm.

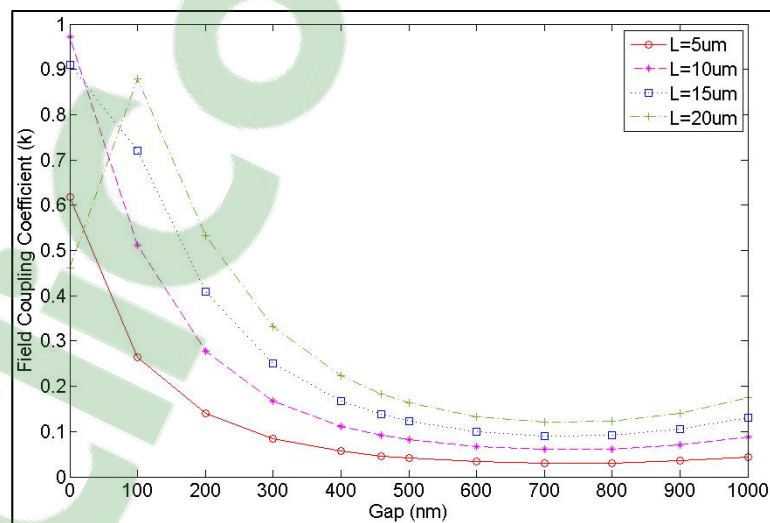


Figure 4.5 Field coupling coefficient ' κ ' vs gap, $\lambda=1550$ nm, coupler length $L=5$ μm , $L=10$ μm , $L=15$ μm and $L=20$ μm , 400 nm x 400 nm waveguide, calculated using the waveguide mode solver with a 10 nm mesh size

The coupling gap is an important parameter to obtain the critical coupling condition and for the ring to behave as a perfect resonator, the dependence of the two supermodes on the coupling gap is also shown in Figure 4.6. This plot shows how the coupling behaviour varies if the coupling gap changes due to the fabrication discrepancies. The n_{eff} of the first two Eigen modes (symmetric and antisymmetric modes) calculated at a wavelength of 1550 nm for a coupling gap of 460 nm are 1.517327 and 1.448628 respectively, and for a coupling gap of 900 nm is 1.500668 and 1.470932, respectively. These effective refractive indices are used to model two different racetrack resonators presented further and to determine the output performance metrics of these device such as FSR, 3-dB bandwidth and Q-factor. The bending radius of the rings are selected to minimize bending losses for the 400 nm x 400 nm waveguide which can be seen in Figure 4.7 for a 90° bend. The coupling length and the radius are selected to obtain a specific path length so as to have the required FSR. Type A racetrack resonator has a total optical path length of 602.11 μm and type B has a total optical path length of 315.56 μm . The κ is chosen to have a high drop port peak intensity and to obtain a critical coupling condition with the minimal 3-dB bandwidth using the transfer function equations in MATLAB (Appendix IV). The selected κ helps in determining the design parameters of ring resonators

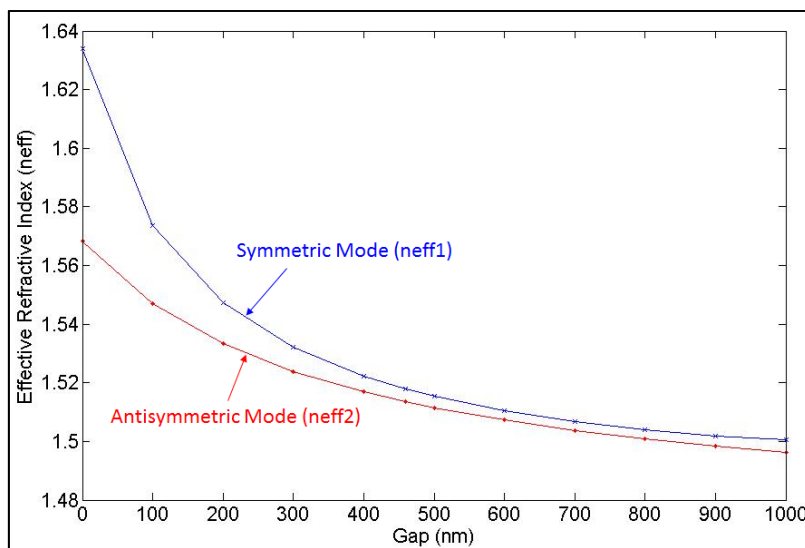


Figure 4.6 The n_{eff} of symmetric and antisymmetric modes versus the coupling gap, $\lambda = 1550$ nm, 400 nm x 400 nm Si_3N_4 waveguide

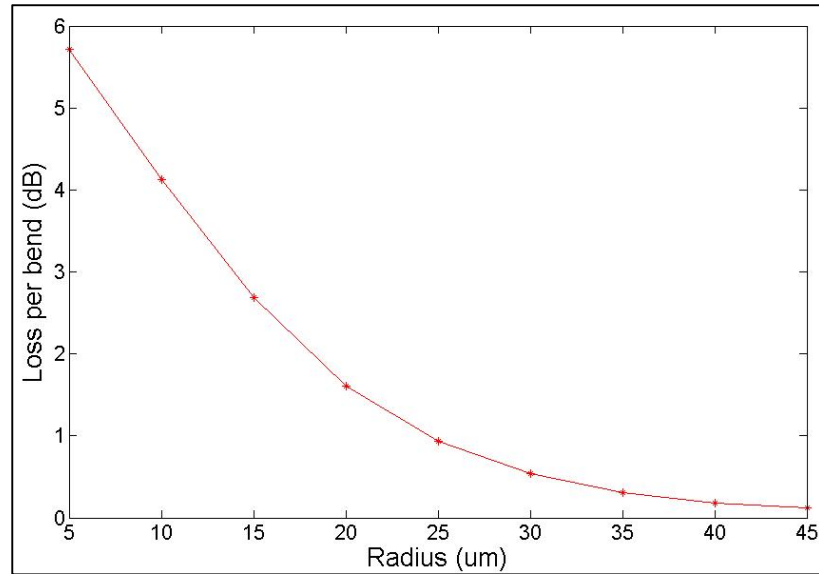


Figure 4.7 Waveguide bend loss vs. radius for 400 nm wide SiN waveguide (in dB scale), bend angle of 90°

such as g and L_c using equations (2.5) – (2.8). The waveguide propagation loss included in the simulations is 1 dB/cm (Bauters et. al, 2011). Both filters are designed to target the central resonant wavelength (λ_o) of 1550 nm. The optimum design parameters for the modelling and simulation of both types of racetrack resonators are listed in Table 4.1. These parameters are used to simulate the structure in 2.5D-FDTD solver to obtain accurate optical response.

The schematic for both the designs are seen in Figure 4.8. The optical power attenuation coefficient ' α ' is considered to be 1 [1/cm]. The simulated optical response of type A and type B are shown in Figure 4.9 and 4.10, respectively. The attributes from the simulated responses are presented in Table 4.2. The FSR obtained for type A ring filter is 2.34 nm (~ 291 GHz) which is almost three times the channel spacing and for the type B is 4.57 nm (~ 568.40 GHz) which is more than five times the channel spacing. The targeted resonant wavelength is near 1550 nm with a high ER for both the designs.

Table 4.1 Design parameters for two different racetrack-resonators

Parameters	R (μm)	L (μm)	Gap (nm)	κ	λ_0 (nm)
Type A	90	18.31	460	0.1699	1550
Type B	50	0.7	900	0.2	1550.34

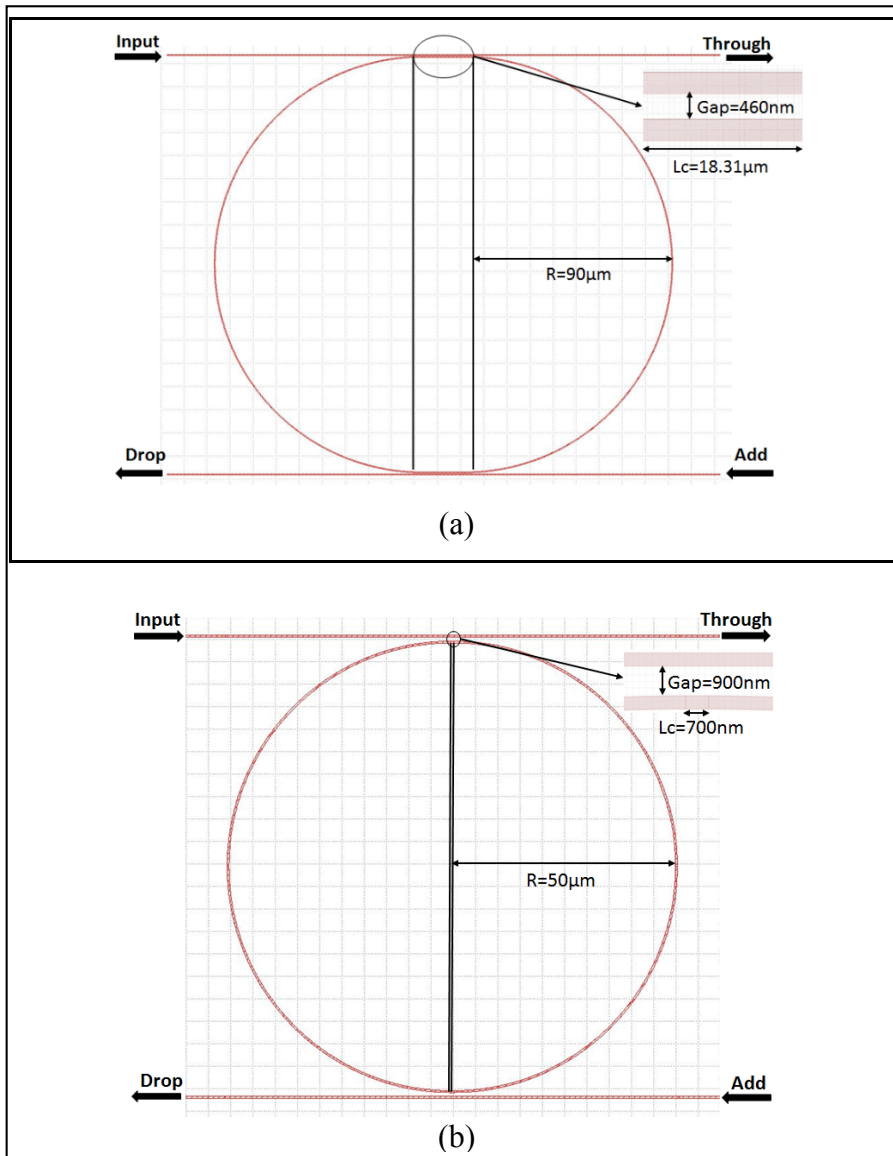


Figure 4.8 The schematic design of two different racetrack resonators (a) Type A, (b) Type B

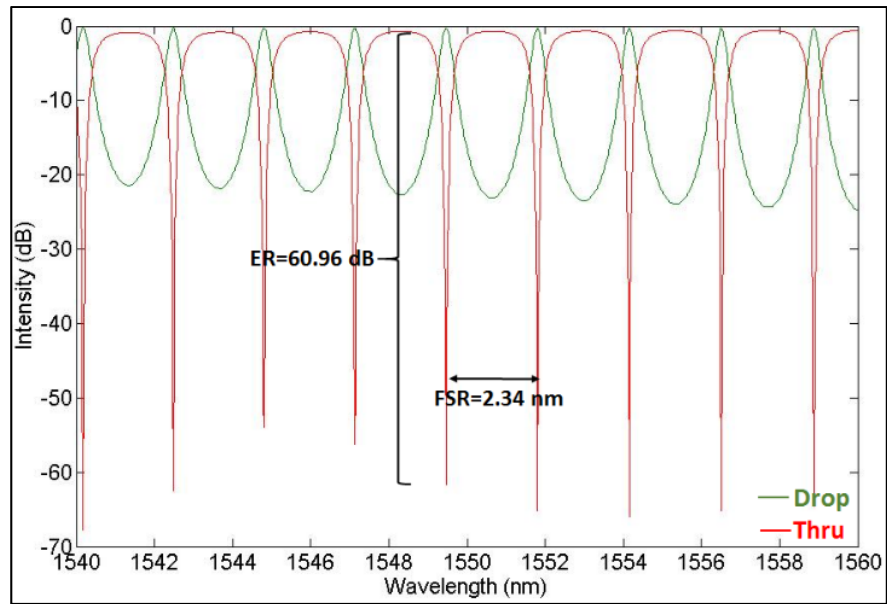


Figure 4.9 Simulated optical response for type A racetrack-resonator

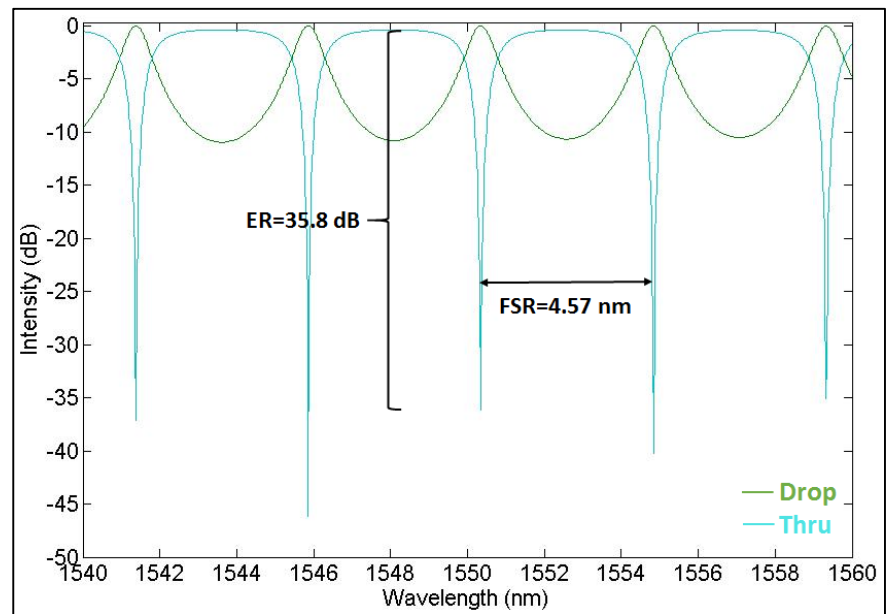


Figure 4.10 Simulated optical response for type B racetrack-resonator

Table 4.2 Performance attributes for two different racetrack-resonators

<u>Parameters</u>	<u>FSR (nm)</u>	<u>FWHM (nm)</u>	<u>ER (dB)</u>	<u>Q-factor</u>	<u>Finesse</u>	<u>λ_0 (nm)</u>
<u>Type A</u>	2.34	0.0074	60.96	209386	316.21	1549.46
<u>Type B</u>	4.57	0.0151	35.79	102671	302.65	1550.34

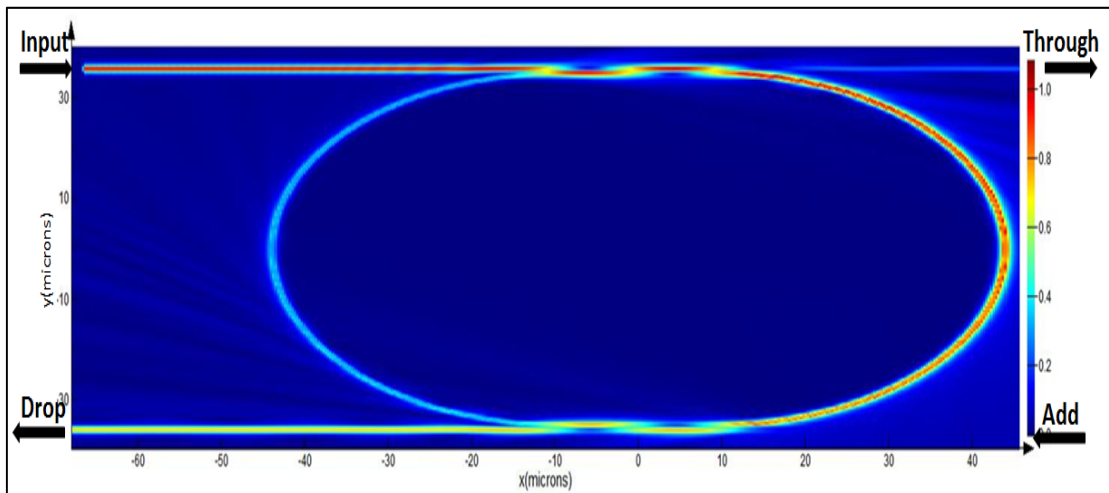


Figure 4.11 The intensity profile of the light propagating inside the racetrack resonator obtained using 2.5D-FDTD simulations in Lumerical MODE.

The drop port peak intensities for both the rings is around $\sim 93\%$ of the total input light power which shows that there is still scattering losses in the FDTD simulations. Figure 4.11 shows the intensity profile of the light propagating inside the ring and some scattering losses as well. It is in an on-resonance state, showing the extraction of all the resonant wavelengths at the drop port from the light injected at the input port, leaving no transmission at the through port.

4.1.2 Fabrication, Measurements and Analysis

For the fabrication of these devices, the layout was made in the K-layout software. The mask dimensions for the straight and the curved waveguides is 400 nm (wide) x 400 nm (height). The total chip size is 1.6 cm x 3.58 cm. Few replicas of the main design are proposed along with some variations in the gaps of the coupling regions and the waveguide widths. Due to the

fabrication discrepancies, these design variations allow a possibility of achieving at-least one working device with the desired output spectral response. No grating couplers or tapers are used at the end of the devices and therefore, light from the input fiber is coupled directly to the waveguide edge facet. The devices were fabricated using the process flow described in the section 3.3.2, where instead of a LPCVD, we have used a PECVD technique for the Si_3N_4 deposition as per the requirement of the research group. The propagation loss measured for the deposited waveguide is around ~ 0.4 dB/cm. Only type A racetrack-resonator devices were measured using the optical test setup (described in section 3.3.3). Type B devices were fabricated but could not be measured due to time constraints. The proper transmission peaks were observed for the devices only at the through port. At the drop port, no proper transmission peaks were measured, instead noise was obtained. This could be due to the high scattering, propagating or coupling losses induced due to the improper coupling gap regions, variation in the waveguide widths and sidewall roughness of the waveguides. The measured transmission response at the through port and the curve-fit for one of the device can be seen in Figure 4.12. This curve fit is nothing but the smoothness of the measured response where the actual device signal is extracted and differentiated from the overall noise due to the setup. Noise can be seen in the measured response which is possibly due to the slight vibration observed in the optical test setup and the noise of the instruments itself. Isolating the optical stage along with both input and output fibres could possibly resolve the issue of noise while performing measurements. Moreover, there is a drift observed in the transmission response of the device which is due to a shift in the test setup while running the wavelength sweep. The obtained FSR is around ~ 5.76 nm which is higher than the theoretical value of 2.34 nm. This increase in the FSR could possibly be due the difference in the fabricated waveguide dimensions as the waveguide width has reduced by almost ~ 40 nm. This reduction in the waveguide width reduces the n_{eff} thereby increasing the FSR (from eqn. 2.20) and so the obtained value holds true as per theory. The obtained n_{eff} of the fabricated waveguide has reduced from 1.4889 to 1.4752 and the n_g has reduced from the 1.762 to 1.6975. This reduction in n_g due to decrease in width of the waveguide has increased the FSR which was validated by simulating the RR using the fabricated dimensions. Although, the change in the thickness of the core waveguide

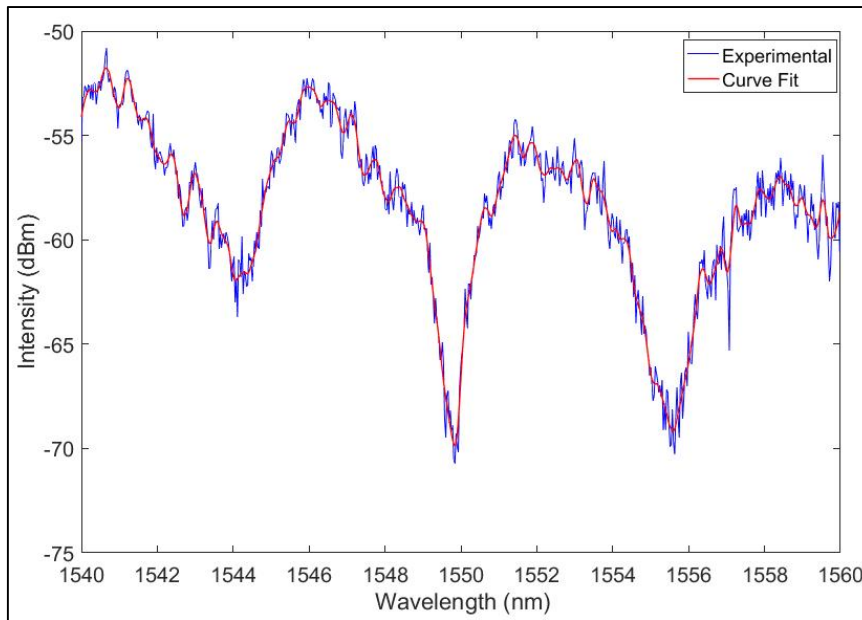


Figure 4.12 Transmission spectra for a small ring filter, waveguide 400 nm x 400 nm

was not taken into consideration. The ER obtained is around ~ 17.21 dB which is well above the desired ER (of 10dB) required for the use in DWDM applications. The measured FWHM is approximately 0.45 nm giving a Q-factor of around 3444 which are low as compared to the simulated results. The SEM image of the fabricated RR and its coupling region is shown in Figure 4.13 where the coupling gap is seen higher than the designed value by ~ 30 nm and the waveguide widths are off by ~ 40 nm. The possible explanation for no output at the drop port could be due to the variation in the coupling gap region which leads to under-coupling, scattering losses due to the sidewall roughness and the propagation losses of the fabricated waveguide. The low peak sharpness and high 3-dB bandwidth could possibly be due to reduction in the n_{eff} of the waveguide. This reduction in n_{eff} has increased the 3-dB bandwidth which in turn has reduced the Q-factor of the fabricated device. Also, the central resonant wavelength (λ_o) is shifted to 1549.84 nm since the n_{eff} has reduced due to change in the fabricated dimensions (from eqn. 2.1). In order to fabricate these filters with dimensional accuracy, some iterations need to be made in the design in future taking into account the fabrication discrepancies. The FSR of the designed filter is much larger than the required channel grid recommended by ITU. But several of these ring filters can be used, as transmissive filters, to remove the chirp of a tunable laser tuned electromechanically via MEMS actuators

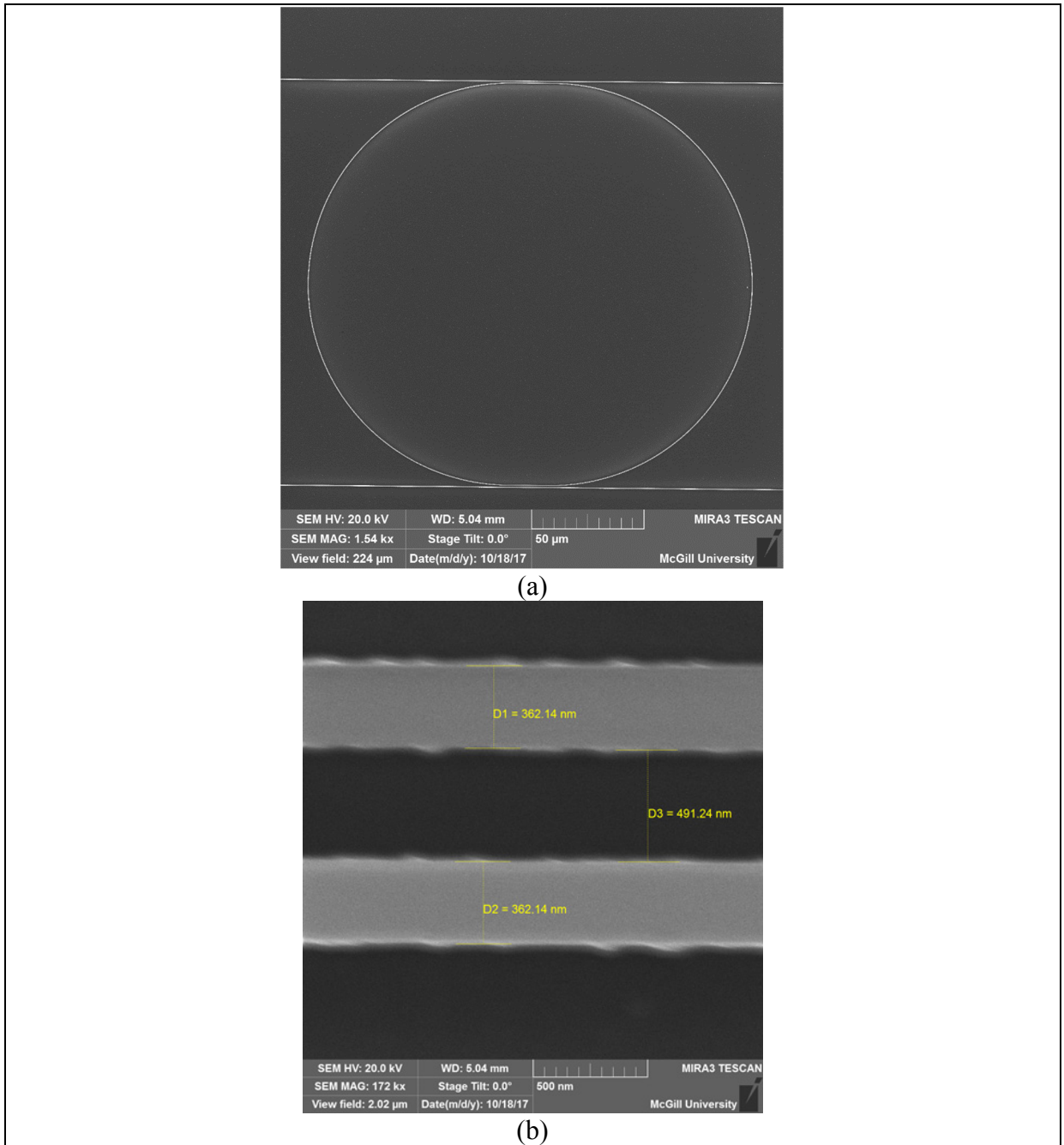


Figure 4.13 SEM image of (a) the fabricated RR and (b) the coupling region of RR showing variation in the gap and the waveguide widths

(setup as shown in Figure 3.1). The transmitted signal from the tunable laser is focused on one of the many transmissive ring filters each corresponding to a different wavelength channel. To

change the wavelength channel, potential is applied to the electrostatic actuator which in turn rotates the MEMS mirror thus allowing to choose the different filters. This selection of different channels will attenuate the ‘0’ data bits and allow only ‘1’ data bits to pass through, thus removing the chirp of a tunable laser.

4.2 Large 4-port add-drop racetrack resonator

4.2.1 Design, Simulation and Optimization

In this section we present a novel method for developing a tunable transmitter by using a Si_3N_4 waveguide based large racetrack resonator filter with a FSR matching the ITU channel grid required for the NG-PON2 systems. With an aim of achieving an economical approach, a low loss SiN ring filter is demonstrated using a CMOS compatible process. The channel waveguide has a square dimension of 435 nm x 435 nm (as seen in Figure 3.3 (a)) giving a good confinement of the light. These dimensions are selected in accordance with our industrial partner so as to match their fabrication process. These nitride ring filters are fabricated over a 4 μm thick SiO_2 layer on a standard Si wafer, cladded by a 4 μm thick oxide over it. The refractive indices of the Si_3N_4 and the SiO_2 at 1550 nm are considered to be 2.0458 and 1.45, respectively. The effective refractive indices n_{eff} and the group indices n_g are calculated using the FDE method via Eigenmode solver for the fundamental TE and TM modes. The obtained n_{eff} for the fundamental TE and TM mode for a straight waveguide are 1.51236 and 1.51217 and their corresponding group indices are 1.8616 & 1.8666, respectively. The n_{eff} and n_g are wavelength dependent and their dependency can be seen in chapter 3 in Figure 3.3 (b) and (c) respectively.

The design approach, as discussed in the section 3.2.2, is based on the initial design of the directional coupler using CMT. Based on the CMT, all the desired coupling parameters are calculated using the analytical equations as discussed in section 2.1. At first, an optimum κ is selected using the analytical equations shown in the MATLAB code for designing a RR (Appendix IV). The waveguide propagation loss considered in simulations is 1 dB/cm (Bauters

et al., 2011). To obtain a critical coupling condition, the coupling losses are included in simulation equal to the cavity losses given by $t = |t|exp(j\phi_t)$, where $|t|$ represents the coupling

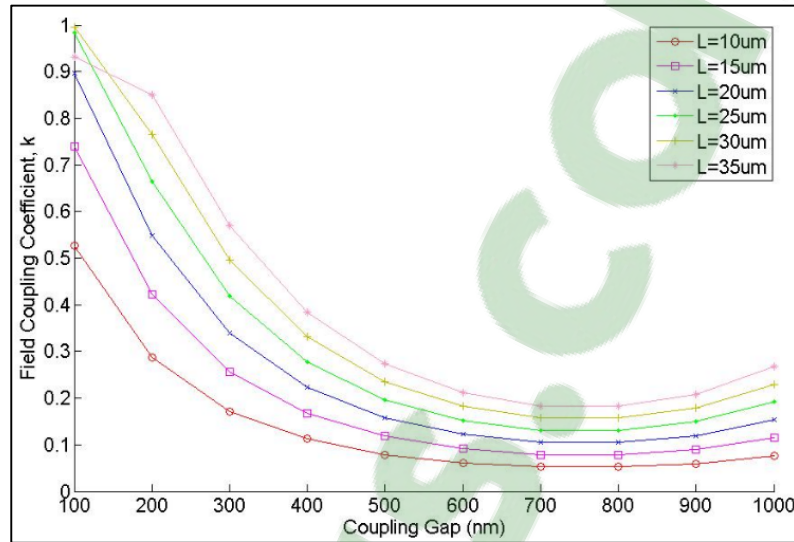


Figure 4.14 Field coupling coefficient ' κ ' vs gap, $\lambda=1550$ nm, coupler length $L=10$ μm , $L=15$ μm , $L=20$ μm , $L=25$, $L=30$ μm and $L=35$ μm , 435 nm x 435 nm waveguide, calculated using the waveguide mode solver with a 10 nm mesh size

losses and ϕ_t represents the phase of the coupler. The value of κ is chosen to have high drop port peak intensity with a minimal 3-dB bandwidth possible. The κ is an important factor in deciding an optimum coupling region and helps in choosing the design parameters such as coupling gap (g) and coupling length (L). A general trend of an exponential decrease in the κ with the increasing gap can be seen in Figure 4.14 for the selected waveguide dimensions as function of coupling lengths. The chosen κ is 0.4645 giving a drop port peak intensity around 99% of the total input power, targeted for λ_0 near 1550 nm. The coupling length in our design consists of two parallel waveguides only (excluding bends) and the power behaviour within a directional coupler can be expressed as a function of the structure of the coupler, position of the coupler, the coupling coefficients and the power transmission ratio. The n_{eff} of the symmetric and antisymmetric modes evaluated using the FDE method are 1.552085 and 1.462307 , respectively for the selected directional coupler gap of 350 nm. The change of these effective refractive indices as a function of coupling gaps is shown in previous chapter in

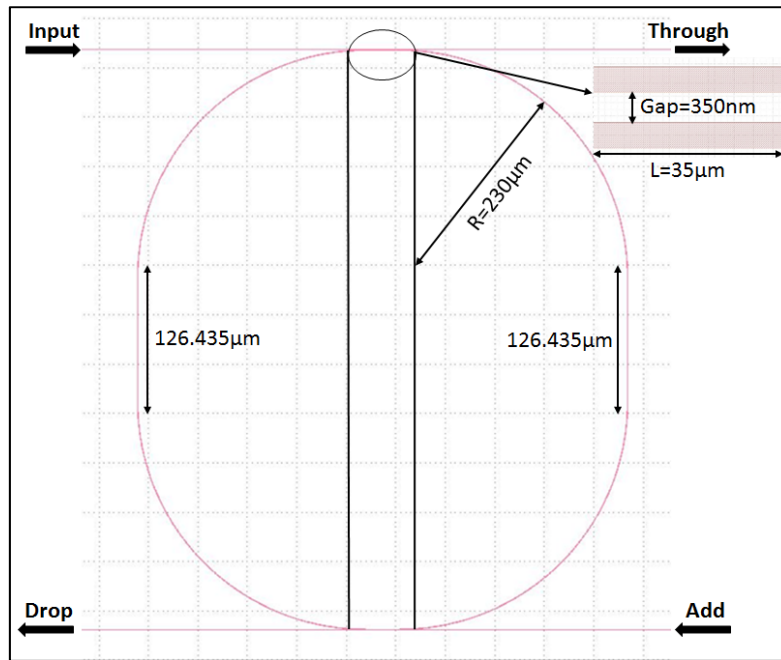


Figure 4.15 The general schematic design of a large racetrack resonator

Figure 3.6 (a). A total optical path length of $1768 \mu\text{m}$ is chosen in order to obtain a desired FSR of 100 GHz (0.8 nm), comprising of ring radius (r) of $230 \mu\text{m}$, coupling length (L) of $35 \mu\text{m}$ and two straight waveguides each of length $126.435 \mu\text{m}$. Using equation (2.9), the required L is obtained to be $35 \mu\text{m}$ depending upon optimum κ and chosen g . The design is simulated in 2.5D-FDTD using Lumerical MODE whose general schematic can be seen in Figure 4.15. A simulated spectral response shown in Figure 4.16 gives the desired FSR of 0.8 nm with the λ_0 at 1550.17 nm which is close to the target wavelength of 1550 nm . The ER obtained is around $\sim 26 \text{ dB}$ for the central resonant wavelength. We have obtained a narrow 3-dB bandwidth of 0.0126 nm giving a sharp resonant peak with a Q-factor of $123,029$. Another important characteristic is Finesse which is calculated to be 63.49 . This single large ring-filter can be used as an external filter in the CML for the NG-PON2 systems as its FSR matches the ITU channel grid.

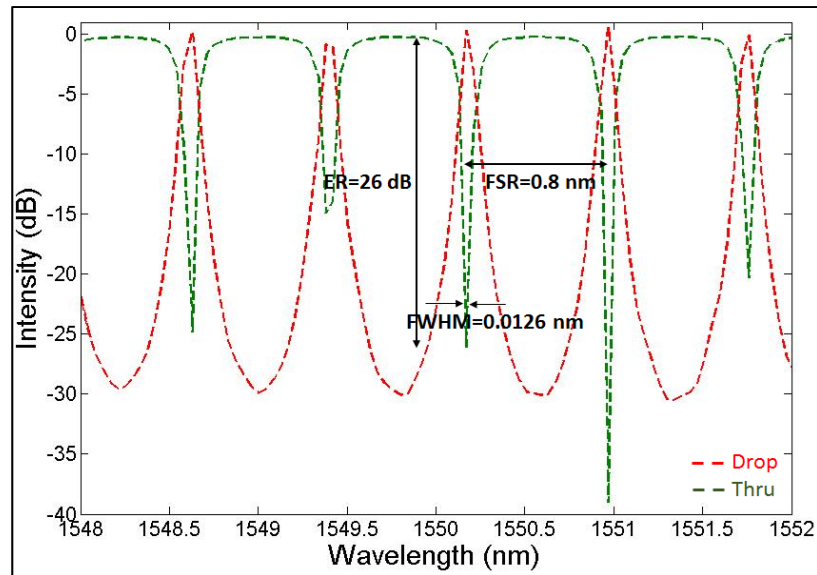


Figure 4.16 Simulated optical spectra of a large racetrack resonator showing transmission at the drop port and the through port (in dB)

To validate that the designed racetrack resonator (as an external filter) aids in improving the ER of the DML, circuit simulations are carried out using Lumerical Interconnect. A circuit simulation schematic in Figure 4.17 shows four different configurations, wherein firstly, a DML signal is sent directly to an EYE diagram analyser which can perform a comprehensive set of measurements on the time domain waveform (Figure 4.17 (1)). Secondly, a DML laser is sent through a 20 Km long fiber to an EYE analyser (Figure 4.17 (2)) which gives the ER without a filter. In a third configuration, the DML signal is sent through a racetrack resonator filter designed for a 100 GHz FSR directly into the EYE diagram analyser (Figure 4.17 (3)), which should aid in increasing the ER of the laser. In the fourth configuration, the DML signal is transmitted through a ring filter which is further sent through a long fiber (20 km) going into an EYE diagram analyser (Figure 4.17 (4)) to verify the effect on the ER as the data signal transmits over a long distance through a fiber. In configuration (1), the EYE filter analyser gives a low ER of 2.97 dB. In configuration (2), the optical signal from the DML is sent just through a 20 Km long optical fiber giving a slightly reduced ER of 2.95 dB which is due to the signal degradation because of the interaction of the frequency chirp with the chromatic dispersion of the fiber. In configuration (3), the DML signal is transmitted through a designed ring filter giving an increased ER of 10.65 dB. This increase in the ER of the DML signal (in

comparison to the configuration (1)) is due to the attenuation of the red-shifted ‘0’ data bits of the signal allowing only the blue-shifted ‘1’ bits to pass. This is done by aligning the laser wavelength on the transmission edge of an OSR, which in this case is the above designed

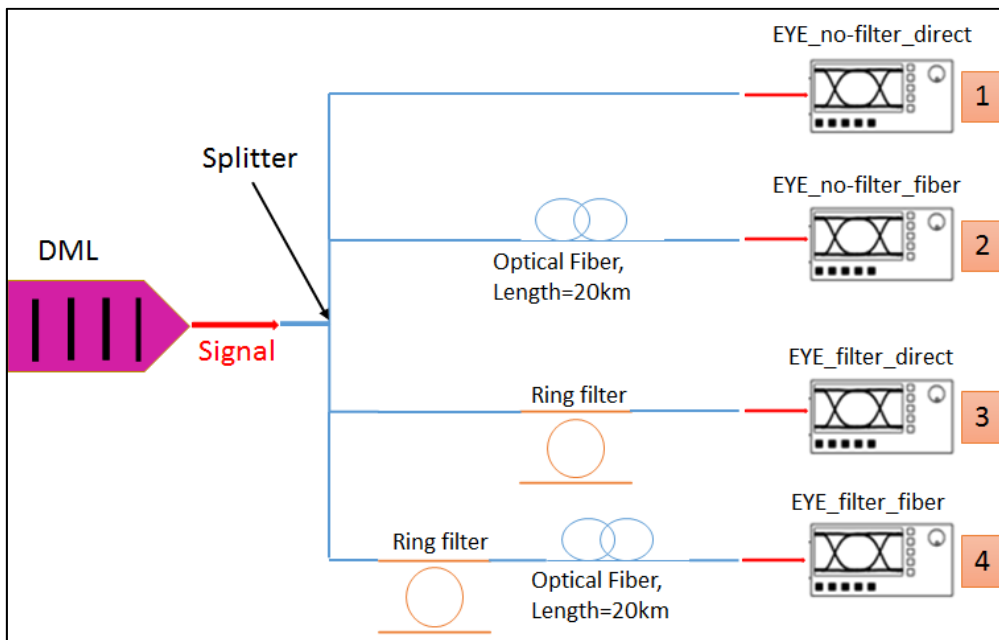


Figure 4.17 A general schematic of the circuit simulation setup in the Lumerical Interconnect showing 4 different configurations

racetrack resonator. The laser wavelength is set at 1550.27 nm. An ER of around ~ 8.81 dB is obtained from the EYE analyser in configuration (4) which is higher compared to the configuration (2) but lower than (3) due to the interaction of the chirp with the chromatic dispersion of the fiber. For the configuration (3), the obtained ER is plotted in Figure 4.18 versus the detuning of the wavelength ($\Delta\lambda$) for a span of ± 1 nm. It shows an increase in the ER of the DML at the wavelengths similar to the resonant wavelengths of the ring filter which occurs by the virtue of aligning the laser wavelength (1550.27 nm) on the transmission edge of the racetrack resonator filter. We observe a high ER of 10.65 dB at a span of ± 0.8 nm corresponding to the FSR of the filter. But, we also observe two peaks at ± 0.4 nm giving even a higher ER of 18.5 dB. The possible explanation for this could be that at ± 0.4 nm the ‘0’ bits are completely attenuated whereas ‘1’ bits are not and are allowed to pass. Whereas, at ± 0.8

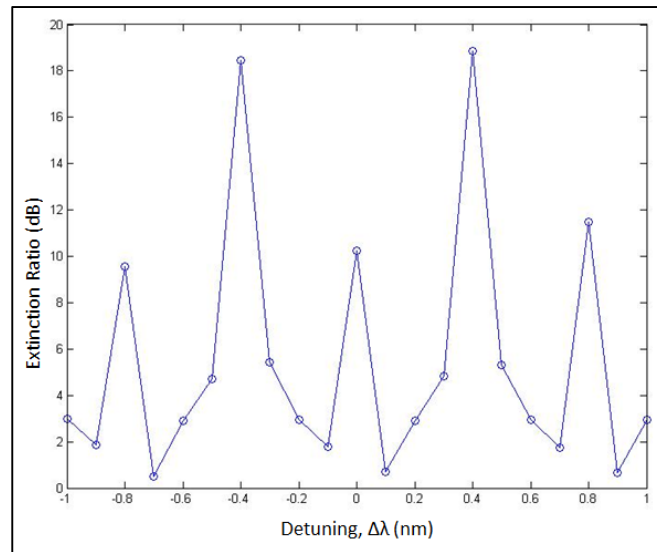


Figure 4.18 Plot showing ER (in dB scale) vs. detuning ($\Delta\lambda$) for configuration (3)

nm, '1' bits are more attenuated than '0' bits resulting in an inversion of the bit pattern which can be seen in Figure 4.19 where the waveform for signal amplitudes are compared and measured using an oscilloscope directly from the laser and after the light has propagated through the ring filter. Thus, higher ER of around 18.5 dB is obtained due to the complete

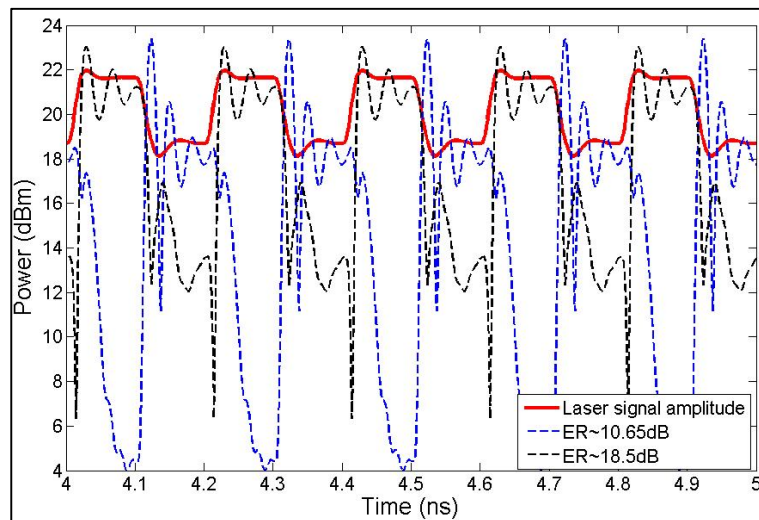


Figure 4.19 Graph showing pulse amplitude from the laser (red line) and the comparison of pulse amplitudes after the propagation through ring filter for lower ER (blue dashed line) and higher ER (black dashed line) obtained

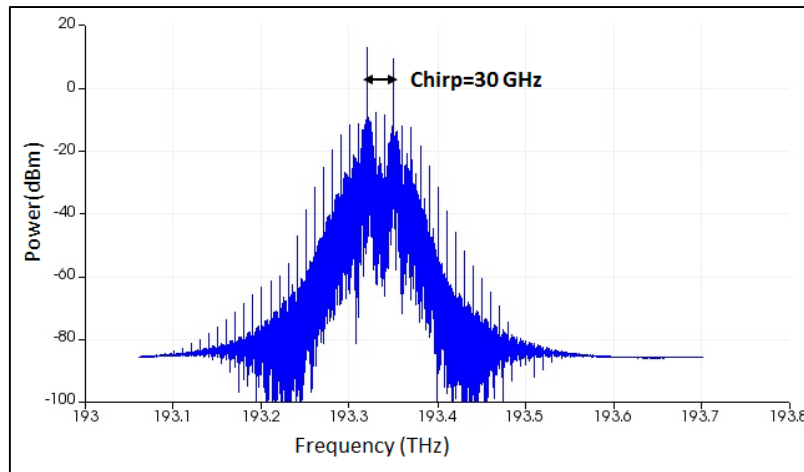


Figure 4.20 Power spectrum as a function of frequency (THz) showing adiabatic chirp

attenuation of ‘0’ bits without attenuating ‘1’ bits. Whereas, other ER of around 10.65 dB is obtained when ‘1’ bits are also attenuated along with ‘0’ bits. The distortions in the pulses after passing through the filter is due to the gain-saturation-induced self-phase modulation (SPM) (Agrawal & Olsson, 1989). An adiabatic chirp of the DML used in the circuit simulations is 30 GHz shown in Figure 4.20. These circuit simulations show and validate the use of a designed racetrack resonator as an external filter in front of the DML (which in our case will be a tunable laser) in order to develop an alternative transmitter, increasing the range of the transmission.

4.2.2 Fabrication, Measurements and Analysis

For the fabrication of this large racetrack resonator, the mask layout is made in the K-layout software with the straight and the curved waveguide mask dimension of 435 nm width. The total chip area is 1.5 cm x 2 cm. Some design variations are proposed so as to mitigate the fabrication discrepancies and to achieve at least one working device giving a desired spectral response. They are designed such that the light couples directly from the input fibre to the waveguide edge facet. The fabrication process flow of these devices is already presented above in section 3.3.2 to match the fabrication criteria of our industrial partner.

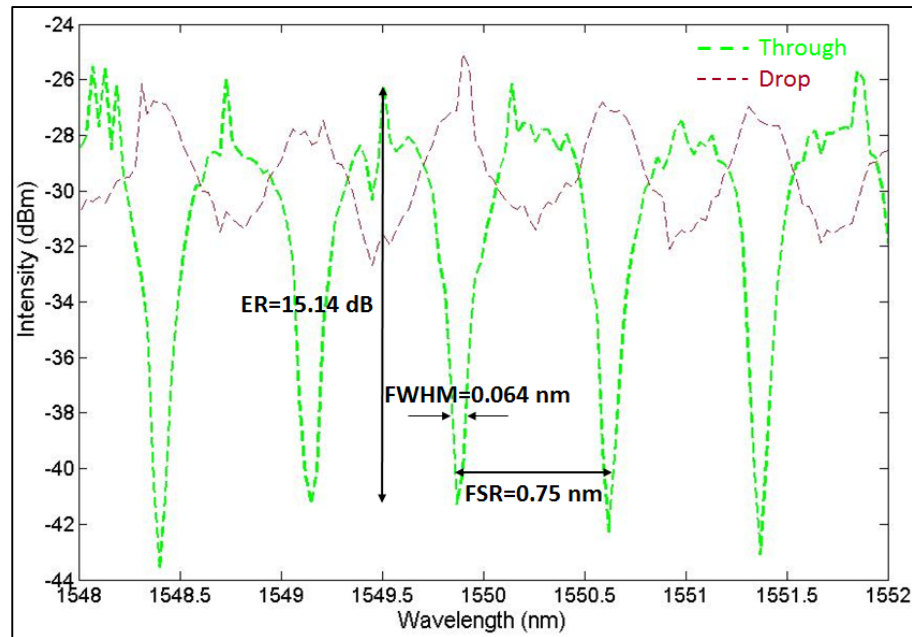


Figure 4.21 Measured spectra showing the transmission at the through and the drop port for a large racetrack resonator

These large racetrack-resonator devices were measured using the optical test setup described in section 3.3.3 where only the fundamental TE mode is excited and the polarization is maintained using the polarization controller. The measured output spectral response at the through and the drop port is shown in Figure 4.21. The measured FSR is 0.75 nm between the two resonant wavelengths at 1549.87 nm and 1550.62 nm. The FSR differs from the theoretical value probably due to the change in the n_g and n_{eff} caused by the difference in the fabricated waveguide dimensions. The obtained ER of the device is 15.14 dB which is less than the theoretical value. The 3-dB bandwidth at 1549.87 nm is 0.064 nm, corresponding to a high Q of 24,217. The Finesse of the device is measured around 11.71. The SEM image of the measured device in Figure 4.22 shows that the waveguide widths have reduced by almost 30 nm and that the gap has increased by almost 40 nm. Therefore, the reduction in the 3-dB bandwidth and the Q-factor could be due to this increase in the coupling gap, which in turn has reduced the κ and n_{eff} (from eqn. 2.22 and 2.24). The ER of the drop port peak intensities are low as compared to the simulated values. A reason for this could be the decrease of κ which in turn has reduced the mode amplitude in the drop port waveguide. A normalized through port transmission curve, shown in Figure 4.23, compares the measured and the simulated response

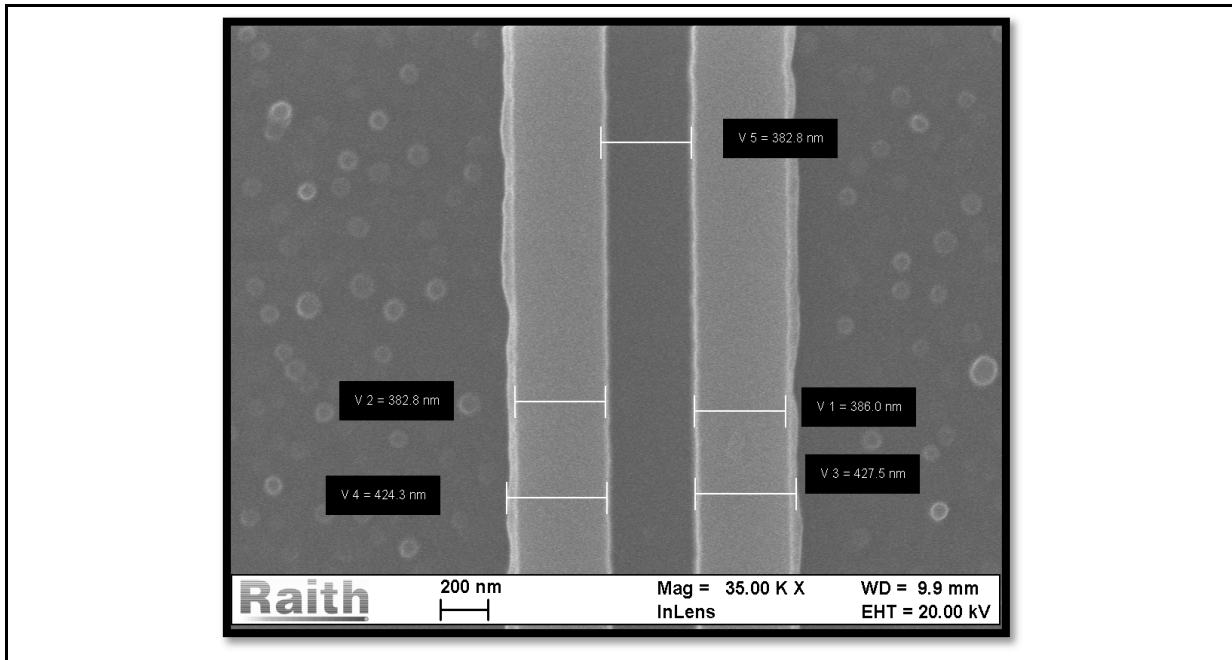


Figure 4.22 SEM image of a directional coupler of a fabricated large RR

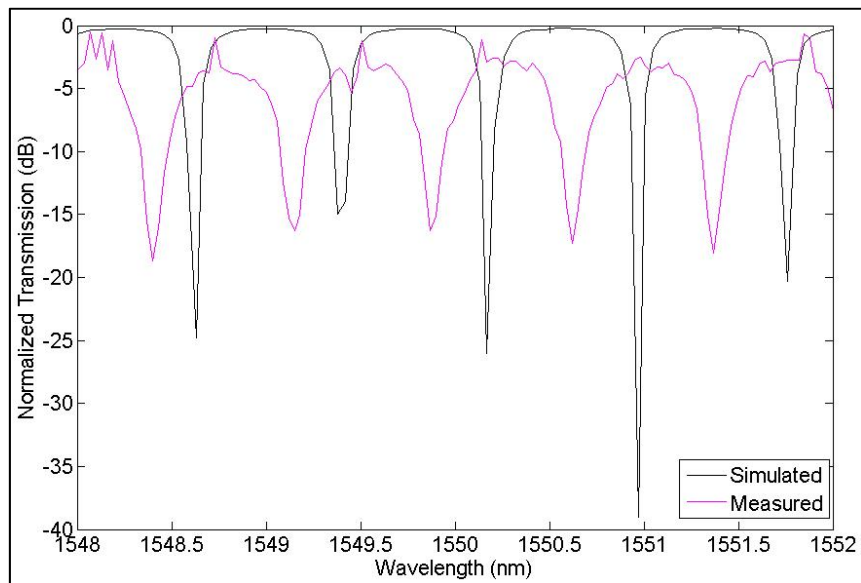


Figure 4.23 Normalized transmission spectra (in dB) showing the simulated and the measured through port response

which shows a blue-shift in the resonant wavelength λ_o . This holds true since the n_{eff} has reduced, thereby, reducing the λ_o (from eqn. 2.1). The measured insertion loss of the fabricated device is around ~ 6 dB. Using equation 2.2, the measured n_g of the fabricated waveguide is 1.8115 which is lower than the simulated value of 1.8625 which effects the device performance. Also, the thickness of the waveguide has increased by 5% which has more effect on the device output as compared to the waveguide width, which can be studied from the plots in Figure 3.24. Therefore, to mitigate the fabrication discrepancies, some iterations will be done in future designs based on the performance of the devices and other data obtained.

4.3 Summary

To summarize, we demonstrate a small and a large Si₃N₄ waveguide racetrack resonator to be used as an external filter in front of the tunable laser to attenuate the adiabatic chirp of the laser. When the laser wavelength is aligned on the transmission edge of the ring filter, data bits ‘0’ are attenuated while data bits ‘1’ are allowed to pass through. This will aid in increasing the ER, thereby increasing the transmission range of the data signal coming from the tunable laser, which will be used in future for implementing the CML. A small racetrack resonator of waveguide dimensions 400 nm x 400 nm gives a FSR of 5.76 nm. The λ_o has shifted to 1549.84 nm, measuring a 3-dB bandwidth of approx. 0.45 nm giving a Q-factor of around 3444. The ER of the device is measured to be around 17.21 dB which is large enough to be used in realizing CML. The measured FSR of the ring filter is almost 7 times the required ITU channel grid. Hence in order to be used for a tunable transmitter, several small rings can be used in front of the tunable laser each corresponding to a particular wavelength channel. The wavelength channel selection will be done using MEMS actuation, thereby attenuating the adiabatic chirp of the tunable laser.

Also, we have demonstrated a large racetrack resonator filter made of Si₃N₄ waveguide with a FSR of 0.75 nm (93.58 GHz) aiming to match the ITU channel grid of 100 GHz spacing. However, the measured FSR is off by 0.05 nm from the desired value of 0.8 nm. The obtained ER is 15.14 dB with a Finesse of 11.71. The measured 3-dB bandwidth at λ_o (1549.87 nm) is

0.064 nm giving a Q-factor of 24,217. The interconnect simulations show an enhancement in the ER of the DML from 2.97 dB to almost 18.5 dB by the use of the designed ring filter. Some iterations will be done in the future design to mitigate the fabrication challenges, thereby, obtaining the desired FSR of 100 GHz. Therefore, in future, the designed RR allows the possibility to demonstrate a novel cost-effective and a compact alternative transmitter technology for the NG-PON2 systems.

CONCLUSIONS AND FUTURE WORK

In summary, we have studied, in theory and experiment, the racetrack-resonators in different configurations and in different waveguide geometries. The photonic ring filters based on Si₃N₄ waveguide platform have been designed, simulated and characterized. The filters demonstrated using a CMOS compatible platform include:

- A photonic ring reflector constituting of a ring having a radius of 35 μm , integrated with Y-splitters to form a reflector configuration. It gives a measured FSR of 6.03 nm with a Q of 1122.82 at λ near 1550 nm with an aim of targeting a wide FSR to be used potentially in tunable lasers.
- A small RR filter with the radius of 90 μm giving a FSR of 5.76 nm, FWHM of 0.45 nm, a Q of 3444 and a high ER of 17.21 dB. This designed small RR filter gives a FSR seven times the channel spacing of the ITU-channel grid of 100 GHz. This compact and cost-effective RR has a potential application in implementing a tunable transmitter by using several such RR's in front of the tunable laser, each corresponding to a different wavelength channel. Then the chirp of the tunable laser will be attenuated by aligning the laser wavelength to one of the many RR wavelengths using channel selection mechanism, thereby, increasing the transmission range of the signal by increasing the ER of the laser.
- A large Si₃N₄ RR filter with an optical path length of 1768 μm giving a FSR of 0.75 nm, a high ER of 15.14 dB, a 3-dB bandwidth of 0.064 nm at 1549.87 nm and a high Q-factor of 24,217. A simulated response gives the desired 100 GHz FSR and high ER of 26 dB but due to fabrication discrepancies the measured values differs. This demonstrated RR filter provides a novel platform for developing a tunable transmitter by acting as an external filter in front of the tunable laser. Our platform of Si₃N₄ photonics provide a cost-effective approach towards developing a CML as compared to the other concepts presented in the literature, wherein instead of thermal tuning we will potentially use electromechanical tuning using MEMS actuators which uses less power

Interconnect simulations have been presented in the thesis for the designed large RR filter which shows an enhancement in the ER of the DML from 2.97 dB to almost 18.5 dB. Also, a novel Si waveguide based serially coupled 3rd order ring filter in the reflector configuration has been designed and simulated showing an extended FSR of 90.2 nm wide enough to cover the entire C or L-band. The Vernier effect is used to achieve a wide FSR using three ring-resonators of different optical path lengths. The spectral response of the device shows an interstitial peak suppression of 7.6 dB with no dominant resonance peak splitting. The important factors concerning design improvement are discussed and compared with the work of the other research groups. To the best of our knowledge, the ring reflector design achieved by integrating a cascaded 3-ring filter along with the Y-splitters is unique and novel in comparison to the ring reflectors reported by other research groups.

In future, the Si 3rd order ring reflector will be optimized further by carefully selecting co-prime integer multiples of the FSRs and by optimizing the κ values for every coupling region. Similarly, the Si₃N₄ ring reflector presented in the thesis will be optimized in future to develop a higher order ring reflector. Some iterations in the actual design will be carried out along with the changes required in the fabrication process flow to achieve the device dimensions with high precision. As we have encountered approximately ± 40 nm variation in the fabricated waveguide widths and the coupling regions of the RR. So, to mitigate them in the future, the bias of ± 40 nm and ± 80 nm will be applied to the design layout to compensate the variation in the performance attributes of the devices obtained due to changes in the n_{eff} and n_g of the waveguides. Also, in future simulations, the bends will also be included while considering optimum κ so as to include the effect of bending region. These photonic ring reflectors, once fabricated, will be promising for a wavelength channel selection system in a tunable laser. In a similar manner, iterations will be done on future designs of the small and the large Si₃N₄ RR so as to mitigate fabrication discrepancies and thus obtaining the desired FSR. The large RR, once fabricated with the exact waveguide dimensions and the coupling gap precision, will give a FSR matching the ITU channel grid spacing of 100 GHz. It has a potential application in realizing a CML operational in burst mode for TWDM in NG-PON2 systems.

APPENDIX I

Derivation for power equations of racetrack resonator

As discussed in Section 2.1, all mode amplitudes depend on the factor ' θ ' which is equal to $\omega L/c$. Where ' L ' is the circumference of the ring given by $L=2\pi r$. ' r ' is the ring radius measured from the ring center to the center of the waveguide, $c=c_0/n_{eff}$ is the phase velocity of the ring mode and $\omega=kc_0$ is the angular frequency, where c_0 refers to the vacuum speed of light. ' k ' is the vacuum wave number related to the wavelength ' λ ' by relation:

$$k = \frac{2\pi}{\lambda} \quad (\text{A I-1})$$

Taken from Rabus (2007)

Using this wave number, the effective refractive index ' n_{eff} ' can be introduced within the ring relations as:

$$\beta = \kappa \cdot n_{eff} = \frac{2\pi \cdot n_{eff}}{\lambda} \quad (\text{A I-2})$$

Taken from Rabus (2007)

where β is the propagation constant. Thus, the value of θ is then given by the relation:

$$\theta = \frac{\omega \cdot L}{c} = \frac{\kappa \cdot c_0 \cdot L}{c} = \kappa \cdot n_{eff} \cdot 2\pi r = \frac{2\pi \cdot n_{eff} \cdot 2\pi r}{\lambda} = 4\pi^2 n_{eff} \frac{r}{\lambda} \quad (\text{A I-3})$$

Taken from Rabus (2007)

Since, all the complex mode amplitudes E are normalized, so that their squared magnitude corresponds to the modal power. Thus the power transmission P_{t1} in the output waveguide is then given by:

$$P_{t1} = |E_{t1}|^2 = \frac{\alpha^2 + |t|^2 - 2\alpha|t|\cos(\theta + \varphi_t)}{1 + \alpha^2|t|^2 - 2\alpha|t|\cos(\theta + \varphi_t)} \quad (\text{A I-4})$$

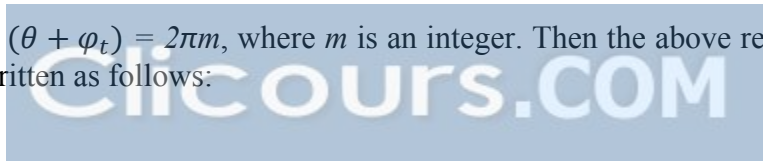
Taken from Rabus (2007)

where $t = |t| \cdot \exp(j\varphi_t)$, $|t|$ represent the coupling losses and φ_t represents the phase of the coupler. The circulating power P_{i2} in the ring is given by:

$$P_{i2} = |E_{i2}|^2 = \frac{\alpha^2(1-|t|^2)}{1 + \alpha^2|t|^2 - 2\alpha|t|\cos(\theta + \varphi_t)} \quad (\text{A I-5})$$

Taken from Rabus (2007)

On resonance, $(\theta + \varphi_t) = 2\pi m$, where m is an integer. Then the above relations of the notch filter can be written as follows:



$$P_{t1} = |E_{t1}|^2 = \frac{(\alpha - |t|)^2}{(1 - \alpha|t|)^2} \quad (\text{A I-6})$$

$$P_{i2} = |E_{i2}|^2 = \frac{\alpha^2(1 - |t|^2)}{(1 - \alpha|t|)^2} \quad (\text{A I-7})$$

Taken from Rabus (2007)

and at resonance, the output power from the drop waveguide in the 4-port add-drop filter is written as:

$$P_{i2} = |E_{i2}|^2 = \frac{(1 - |t_1|^2)(1 - |t_2|^2)\alpha}{(1 - \alpha|t_1 t_2|)^2} \quad (\text{A I-8})$$

Taken from Rabus (2007)

The through port mode amplitude E_{t1} will be zero at resonance for identical symmetrical couplers $t_1 = t_2$ at $\alpha = 1$, which shows that the wavelength at resonance is fully extracted by the resonator. The value of loss coefficient $\alpha = 1$ can only be achieved by implementing the gain incorporated inside the ring resonator to compensate the waveguide losses. The possibility of achieving the condition of output power from the through waveguide, $P_{t1} = 0$, is only by adjusting the coupling parameters t_1, t_2 to the loss coefficient α (i.e. $\alpha = |t_1|/|t_2|$)

The derivation of the FWHM or 3-dB bandwidth

Using the expression of the drop port eqn. (2.9) and the corresponding above eqn. of P_{i2} , we have:

$$\left| \frac{-\kappa_1^* \kappa_2 \alpha_{1/2} e^{j\theta_{1/2}}}{1 - t_1^* t_2^* \alpha e^{j\theta}} \right|^2 = \frac{1}{2} \frac{|\kappa_1|^2 |\kappa_2|^2 \alpha}{(1 - \alpha|t_1 t_2|)^2} \quad (\text{A I-9})$$

Taken from Rabus (2007)

Assuming that the coupling coefficients are real, lossless, and without a phase term then the above eqn. can be written as:

$$\frac{(\kappa_1 \kappa_2 \alpha_{1/2})^2}{1 - 2t_1 t_2 \alpha \cos(\theta) + (t_1 t_2 \alpha)^2} = \frac{1}{2} \frac{(\kappa_1 \kappa_2 \alpha_{1/2})^2}{(1 - t_1 t_2 \alpha)^2} \quad (\text{A I-10})$$

Taken from Rabus (2007)

Then,

$$2(1 - t_1 t_2 \alpha)^2 = 1 - 2t_1 t_2 \alpha \cos(\theta) + (t_1 t_2 \alpha)^2 \quad (\text{A I-11})$$

Taken from Rabus (2007)

For small θ , using the real part of the series expansion of the Euler formula $\cos(\theta) = 1 - \theta^2/2$ and so we have,

$$\theta^2 = \frac{(1 - t_1 t_2 \alpha)^2}{t_1 t_2 \alpha} \quad (\text{A I-12})$$

Taken from Rabus (2007)

Which can be further reduced to, $\theta = 1-t^2 / t$. In the wavelength domain it can then be written as:

$$2\delta\Delta = \frac{\lambda^2}{\pi L n_{eff}} \frac{1-t^2}{t} \quad (\text{A I-13})$$

Taken from Rabus (2007)

The expression which is commonly used can be obtained by assuming weak coupling and $\lambda \gg \delta\lambda$, then

$$FWHM = 2\delta\lambda = \frac{\kappa^2 \lambda^2}{\pi L n_{eff}} \quad (\text{A I-14})$$

Taken from Rabus (2007)

APPENDIX II

Derivation of transfer equations for 3rd order ring filter

In order to derive the transfer function for the through port for a serially coupled three ring resonator, different individual loop gains are considered. There are six individual loop gains and are expressed as (Chaichuay et al., 2009):

$$L_1^3 = t_1\sqrt{\alpha z^{-1}}t_2\sqrt{\alpha z^{-1}} = t_1t_2\sqrt{\alpha z^{-1}} \quad (\text{A II-1})$$

$$L_2^3 = t_2\sqrt{\alpha z^{-1}}t_3\sqrt{\alpha z^{-1}} = t_2t_3\sqrt{\alpha z^{-1}} \quad (\text{A II-2})$$

$$L_3^3 = t_3\sqrt{\alpha z^{-1}}t_4\sqrt{\alpha z^{-1}} = t_3t_4\sqrt{\alpha z^{-1}} \quad (\text{A II-3})$$

$$L_4^3 = t_1\sqrt{\alpha z^{-1}}(-\kappa_2)\sqrt{\alpha z^{-1}}t_3\sqrt{\alpha z^{-1}}(-\kappa_2)\sqrt{\alpha z^{-1}} = -t_1t_3\kappa_2^2(\alpha z^{-1})^2 \quad (\text{A II-4})$$

$$L_5^3 = t_2\sqrt{\alpha z^{-1}}(-\kappa_3)\sqrt{\alpha z^{-1}}t_4\sqrt{\alpha z^{-1}}(-\kappa_3)\sqrt{\alpha z^{-1}} = -t_2t_4\kappa_3^2(\alpha z^{-1})^2 \quad (\text{A II-5})$$

$$\begin{aligned} L_6^3 &= t_1\sqrt{\alpha z^{-1}}(-\kappa_2)\sqrt{\alpha z^{-1}}(-\kappa_3)\sqrt{\alpha z^{-1}}t_4\sqrt{\alpha z^{-1}}(-\kappa_3)\sqrt{\alpha z^{-1}}(-\kappa_2)\sqrt{\alpha z^{-1}} \\ &= t_1t_4\kappa_2^2\kappa_3^2(\alpha z^{-1})^3 \end{aligned} \quad (\text{A II-6})$$

There are five possible products of transmittance for two separate loops (i.e. the loops which have no node in common) given by (Chaichuay et al., 2009):

$$L_{12}^3 = t_1t_2^2t_3(\alpha z^{-1})^2 \quad (\text{A II-7})$$

$$L_{23}^3 = t_2t_3^2t_4(\alpha z^{-1})^2 \quad (\text{A II-8})$$

$$L_{13}^3 = t_1t_2t_3t_4(\alpha z^{-1})^2 \quad (\text{A II-9})$$

$$L_{34}^3 = -t_1t_3^2t_4\kappa_2^2(\alpha z^{-1})^3 \quad (\text{A II-10})$$

$$L_{15}^3 = -t_1t_2^2t_4\kappa_3^2(\alpha z^{-1})^3 \quad (\text{A II-11})$$

Also, there is one possible product of transmittance of three separate loops, given by (Chaichuay et al., 2009):

$$L_{123}^3 = t_1t_2^2t_3^2t_4(\alpha z^{-1})^3 \quad (\text{A II-12})$$

APPENDIX III

Derivation of relation between effective refractive index $n(r, \phi)$ and field function (ψ)

For a homogeneous microdisk resonator having radius R , the effective refractive index $n(r, \phi) = n$ if $r < R$ and inside the microdisk Eqs. 2.1 and 2.3 take the form

$$\frac{\partial^2 \psi}{\partial r^2} + \frac{1}{r} \frac{\partial \psi}{\partial r} + \frac{1}{r^2} \frac{\partial^2 \psi}{\partial \phi^2} + k^2 n^2 \psi(r, \phi) = 0 \quad (\text{A.III-1})$$

Taken from Dettmann (2008)

where ψ is either equal to Ez or H_z , depending upon the polarization. The surrounding refractive index is fixed to $n=1$. Separation of variables and physical conditions in the middle of the disk and at infinity lead to the field function ψ of the form:

$$\psi = \begin{cases} A_m j_m(knr) e^{im\phi}, & r < R \\ B_m H_m(kr) e^{im\phi}, & r > R \end{cases} \quad (\text{A.III-2})$$

Taken from Dettmann (2008)

where, J_m and H_m are Bessel and Hankel functions of the first kind respectively and m is the azimuthal modal index. Then the boundary conditions (continuity of the EM fields) at the point $r=R$ lead to a set of the independent transcendental equations for the microdisk resonances

$$J_m(k_{res}nR)H'_m(k_{res}R) - \beta J'_m(k_{res}nR)H_m(k_{res}R) = 0 \quad (\text{A III-3})$$

Taken from Dettmann (2008)

where $\beta=n$ for TM modes and $\beta=1/n$ for TE modes. The radial modal index 'q' is used to label different resonances with the same azimuthal index 'm'

On the basis of self joint extension theory (Zorbas, 1980) (Shigehara, 1994) (Sieber, 2007) it is shown that resonances of a homogeneous microdisk of radius R with a point scatterer of strength a located at the distance $d < R$ with the corresponding local coordinates (d, ϕ_d) are defined by the transcendental equation

$$0 = \frac{i\pi}{2} - \ln\left(\frac{k_{res}na}{2}\right) - \gamma - \frac{i\pi}{2} \sum_{m=0}^{\infty} \frac{D_m}{C_m} \epsilon_m J_m^2(k_{res}nd) \quad (\text{A III-4})$$

Taken from Dettmann (2008)

where $\gamma=0.5772$ is the Euler-Mascheroni constant, $\epsilon_m = 2$ if $m \neq 0$, $\epsilon_m=1$ if $m = 0$, and

$$D_m = H_m(k_{res}nR)H'_m(k_{res}R) - \beta H'_m(k_{res}nR)H_m(k_{res}R) \quad (\text{A III-5})$$

$$C_m = J_m(k_{res}nR)H'_m(k_{res}R) - \beta J'_m(k_{res}nR)H_m(k_{res}R) \quad (\text{A III-6})$$

Taken from Dettmann (2008)

The field function ψ is then of the form

$$\Psi = N \begin{cases} -\frac{i}{4} H_0(K_n |r - d|) + \frac{i}{4} \sum_{m=0}^{\infty} \frac{D_m}{C_m} \epsilon_m \cos[m(\phi - \phi_d)] J_m(knr_{<}) J_m(knr_{>}), & r < R \\ \frac{1}{2\pi k R} \sum_{m=0}^{\infty} \frac{1}{C_m} \epsilon_m \cos[m(\phi - \phi_d)] J_m(knd) H_m(kr), & r > R \end{cases} \quad (\text{A III-7})$$

Taken from Dettmann (2008)

where N is a normalization factor and $r_{<} (r_{>})$ is the smaller (larger) of r and d

APPENDIX IV

MATLAB script for computing optical response of ring-resonator

```
% RingResonator.m: Ring Resonator spectrum

function [Ethru, Edrop]=RingResonator (lambda, Filter_type, r, Lc, k)
% lambda: wavelength (can be a 1D array) in meters
% type: "all-pass" or "add-drop"
% r: radius
% Lc: coupler length

lambda=(1500:0.001:1600)*1e-9; % wavelength range
Filter_type='add-drop';
r=90e-6;
Lc=18.31e-6;
k=0.1696; t=sqrt(1-k^2); %coupling coefficients
neff = neff_lambda(lambda);

alpha_wg_dB=1; % optical loss of optical waveguide, in dB/cm
alpha_wg=-log(10^(-alpha_wg_dB/10));% converted to /cm
L_rt=Lc*2+2*pi*r;
phi_rt=(2*pi./lambda).*neff*L_rt; % beta = propagation constant
A=exp(-alpha_wg*100*L_rt); % round-trip optical power attenuation
alpha_av=-log(A)/L_rt; % average loss of the cavity
if (Filter_type=='all-pass')
Ethru=(-sqrt(A)+t*exp(-1i*phi_rt)) ./ (-sqrt(A)*conj(t)+exp(-1i*phi_rt));
Edrop=zeros(1,length(lambda));
elseif (Filter_type=='add-drop') % symmetrically coupled
Ethru=(t-conj(t)*sqrt(A)*exp(1i*phi_rt)) ./ (1-sqrt(A)*conj(t)^2*exp(1i*phi_rt));
Edrop=-conj(k)*k*sqrt(sqrt(A)*exp(1i*phi_rt)) ./ (1-sqrt(A)*conj(t)^2*exp(1i*phi_rt));
else
error(1, "The"Filter_type" has to be "all-pass" or "add-drop".\n");
end
plot (lambda, [abs(Ethru); abs(Edrop)])
hold on

function [neff]=neff_lambda(lambda)
neff = 1.5180 - 0.85*(lambda*1e-9-1.55); % neff of the used waveguide
```


APPENDIX V

MATLAB script for computing of cut-off thickness

Taken from (Gang, 2005)

```
nf=2.0458; %R.I. of Si3N4
nc=1.45; %R.I. of cladding (SiO2)
ns=1.45; %R.I. of substrate (SiO2)
m=0; %TE modes
lambda=1.55e-6; %wavelength
k0=2*pi/lambda;
beta=k0*nf;
A=sqrt((ns.^2-nc.^2)/(nf.^2-ns.^2));
tco=(lambda/(2*pi*sqrt(nf.^2-ns.^2)))*((m*pi)+atan(A)) %compute cutoff
```


BIBLIOGRAPHY

- 40-Gigabit-capable passive optical networks 2 (NG-PON2): Physical media dependent (PMD) layer specification (2014). *SERIES G: TRANSMISSION SYSTEMS AND MEDIA, DIGITAL SYSTEMS AND NETWORKS*. Retrieved from www.itu.int/rec/T-REC-G.989.2
- Abdulla, S. C., Kauppinen, L., Dijkstra, M., de Boer, M. J., Berenschot, E., Jansen, H. V., Krijnen, G. J. (2011). Tuning a racetrack ring resonator by an integrated dielectric MEMS cantilever. *Optics express*, 19(17), p.p. 15864-15878.
- Agrawal, G. P., & Olsson, N. A. (1989). Self-phase modulation and spectral broadening of optical pulses in semiconductor laser amplifiers. *IEEE Journal of quantum electronics*, 25(11), p.p. 2297-2306.
- Alonso-Ramos, C., Ortega-Monux, A., Molina-Fernández, I., Annoni, A., Melloni, A., Strain, M., Morichetti, F. (2014). *Silicon-on-insulator single channel-extraction filter for DWDM applications*. Paper presented at the Group IV Photonics (GFP), 2014 IEEE 11th International Conference on.
- Amatya, R., Holzwarth, C. W., Popovic, M., Gan, F., Smith, H., Kartner, F., & Ram, R. (2007). *Low power thermal tuning of second-order microring resonators*. Paper presented at the Lasers and Electro-Optics, 2007. CLEO 2007. Conference on.
- Apalkov, V., & Raikh, M. (2004). Directional emission from a microdisk resonator with a linear defect. *Physical Review B*, 70(19), 195317.
- Arbabi, A., Kang, Y. M., Lu, C.-Y., Chow, E., & Goddard, L. L. (2011). Realization of a narrowband single wavelength microring mirror. *Applied Physics Letters*, 99(9), 091105.
- Baehr-Jones, T., Pinguet, T., Guo-Qiang, P. L., Danziger, S., Prather, D., & Hochberg, M. (2012). Myths and rumours of silicon photonics. *Nature Photonics*, 6(4), 206.
- Barclay, P. E., Srinivasan, K., Painter, O., Lev, B., & Mabuchi, H. (2006). Integration of fiber-coupled high-Q Si N x microdisks with atom chips. *Applied Physics Letters*, 89(13), 131108.
- Barwicz, T., Popovic, M. A., Rakich, P. T., Watts, M. R., Haus, H. A., Ippen, E. P., & Smith, H. I. (2004). Microring-resonator-based add-drop filters in SiN: fabrication and analysis. *Optics express*, 12(7), p.p. 1437-1442.

- Barwicz, T., Popović, M. A., Watts, M. R., Rakich, P. T., Ippen, E. P., & Smith, H. I. (2006). Fabrication of add-drop filters based on frequency-matched microring resonators. *Journal of lightwave technology*, 24(5), 2207.
- Bauters, J. F., Heck, M. J., John, D., Dai, D., Tien, M.-C., Barton, J. S., Bowers, J. E. (2011). Ultra-low-loss high-aspect-ratio Si₃N₄ waveguides. *Optics express*, 19(4), p.p. 3163-3174.
- Binder, J., & Kohn, U. (1994). 10 gbit/s-dispersion optimized transmission at 1.55/spl mu/m wavelength on standard single mode fiber. *IEEE Photonics Technology Letters*, 6(4), p.p. 558-560.
- Boeck, R., Caverley, M., Chrostowski, L., & Jaeger, N. A. (2015). Grating-assisted silicon-on-insulator racetrack resonator reflector. *Optics express*, 23(20), p.p. 25509-25522.
- Boeck, R., Jaeger, N. A., Rouger, N., & Chrostowski, L. (2010). Series-coupled silicon racetrack resonators and the Vernier effect: theory and measurement. *Optics express*, 18(24), p.p. 25151-25157.
- Boeck, R., Shi, W., Chrostowski, L., & Jaeger, N. (2013). FSR-eliminated Vernier racetrack resonators using grating-assisted couplers. *IEEE Photonics Journal*, 5(5), p.p. 2202511-2202511.
- Bogaerts, W., De Heyn, P., Van Vaerenbergh, T., De Vos, K., Kumar Selvaraja, S., Claes, T., Baets, R. (2012). Silicon microring resonators. *Laser & Photonics Reviews*, 6(1), p.p. 47-73.
- Borselli, M., Johnson, T. J., & Painter, O. (2005). Beyond the Rayleigh scattering limit in high-Q silicon microdisks: theory and experiment. *Optics express*, 13(5), p.p. 1515-1530.
- Brière, J., Beaulieu, P.-O., Saidani, M., Nabki, F., & Menard, M. (2015). *Rotational MEMS mirror with latching arm for silicon photonics*. Paper presented at the MOEMS and Miniaturized Systems XIV.
- Briere, J., Elsayed, M. Y., Saidani, M., Bérard, M., Beaulieu, P.-O., Rabbani-Haghighi, H., Ménard, M. (2017). Rotating circular micro-platform with integrated waveguides and latching arm for reconfigurable integrated optics. *Micromachines*, 8(12), 354.
- Cai, H., & Poon, A. W. (2012). Optical trapping of microparticles using silicon nitride waveguide junctions and tapered-waveguide junctions on an optofluidic chip. *Lab on a chip*, 12(19),p.p. 3803-3809.
- Chae, C.-J., & Skafidas, E. (2013). *Microring-based wavelength-selective reflection/rejection filter with independently determined bandwidth and reflectance*. Paper presented at the Photonics Conference (IPC), 2013 IEEE.

- Chaichuay, C., Yupapin, P. P., & Saeung, P. (2009). The serially coupled multiple ring resonator filters and Vernier effect. *Optica Applicata*, 39(1).
- Chen, L., Doerr, C. R., Buhl, L., Baeyens, Y., & Aroca, R. A. (2011). Monolithically integrated 40-wavelength demultiplexer and photodetector array on silicon. *IEEE Photonics Technology Letters*, 23(13), p.p. 869-871.
- Cheng, X., Hong, J., Spring, A. M., & Yokoyama, S. (2017). Fabrication of a high-Q factor ring resonator using LSCVD deposited Si₃N₄ film. *Optical Materials Express*, 7(7), p.p. 2182-2187.
- Chimot, N., Joshi, S., Provost, J.-G., Mekhazni, K., Blache, F., Pommereau, F., Gay, M. (2016). Monolithic integration on InP of a DML and a ring resonator for future access networks. *IEEE Photonics Technology Letters*, 28(19), p.p. 2039-2042.
- Chrostowski, L., & Hochberg, M. (2015). *Silicon photonics design: from devices to systems*: Cambridge University Press.
- Chu, T., Fujioka, N., & Ishizaka, M. (2009). Compact, lower-power-consumption wavelength tunable laser fabricated with silicon photonic wire waveguide micro-ring resonators. *Optics express*, 17(16), p.p. 14063-14068.
- Chu, T., Fujioka, N., Tokushima, M., Nakamura, S., & Ishizaka, M. (2010). *Full C and L bands wavelength tunable laser module with silicon micro-ring resonators*. Paper presented at the OptoElectronics and Communications Conference (OECC), 2010 15th.
- Chung, Y., Kim, D.-G., & Dagli, N. (2006). Reflection properties of coupled-ring reflectors. *Journal of lightwave technology*, 24(4), p.p. 1865-1874.
- Cliche, J.-F., Painchaud, Y., Latrasse, C., Picard, M.-J., Alexandre, I., & Têtu, M. (2007). *Ultra-narrow Bragg grating for active semiconductor laser linewidth reduction through electrical feedback*. Paper presented at the Bragg Gratings, Photosensitivity, and Poling in Glass Waveguides.
- Cocorullo, G., Della Corte, F., & Rendina, I. (1999). Temperature dependence of the thermo-optic coefficient in crystalline silicon between room temperature and 550 K at the wavelength of 1523 nm. *Applied Physics Letters*, 74(22), p.p. 3338-3340.
- Dahlem, M. S., Holzwarth, C. W., Khilo, A., Kärtner, F. X., Smith, H. I., & Ippen, E. P. (2010). *Eleven-channel second-order silicon microring-resonator filterbank with tunable channel spacing*. Paper presented at the Conference on Lasers and Electro-Optics.
- Dai, D., Bauters, J., & Bowers, J. E. (2012). Passive technologies for future large-scale photonic integrated circuits on silicon: polarization handling, light non-reciprocity and loss reduction. *Light: Science & Applications*, 1(3), e1.

- De Heyn, P., De Coster, J., Verheyen, P., Lepage, G., Pantouvaki, M., Absil, P., Van Thourhout, D. (2013). Fabrication-tolerant four-channel wavelength-division-multiplexing filter based on collectively tuned Si microrings. *Journal of lightwave technology*, 31(16), p.p. 3085-3092.
- Dettmann, C., Morozov, G., Sieber, M., & Waalkens, H. (2008). *TM and TE directional modes of an optical microdisk resonator with a point scatterer*. Paper presented at the Transparent Optical Networks, 2008. ICTON 2008. 10th Anniversary International Conference on.
- Dinu, M., Quochi, F., & Garcia, H. (2003). Third-order nonlinearities in silicon at telecom wavelengths. *Applied Physics Letters*, 82(18), p.p. 2954-2956.
- do Nascimento, A., Manera, L., Diniz, J., Silva, A., dos Santos, M., Barea, L., & Frateschi, N. (2014). *Silicon nitride for nonlinear optics applications in the telecommunications C-band deposited by ECR-CVD*. Paper presented at the Microelectronics Technology and Devices (SBMicro), 2014 29th Symposium on.
- Dong, P., Qian, W., Liang, H., Shafiiha, R., Feng, N.-N., Feng, D., Asghari, M. (2010). Low power and compact reconfigurable multiplexing devices based on silicon microring resonators. *Optics express*, 18(10), p.p. 9852-9858.
- Emelett, S. J., & Soref, R. (2005). Design and simulation of silicon microring optical routing switches. *Journal of lightwave technology*, 23(4), p.p. 1800-1807.
- Epping, J. P., Hoekman, M., Mateman, R., Leinse, A., Heideman, R. G., van Rees, A., . . . Boller, K.-J. (2015). High confinement, high yield Si₃N₄ waveguides for nonlinear optical applications. *Optics express*, 23(2), p.p. 642-648.
- Errando-Herranz, C., Niklaus, F., Stemme, G., & Gylfason, K. B. (2015). Low-power microelectromechanically tunable silicon photonic ring resonator add-drop filter. *Optics Letters*, 40(15), p.p. 3556-3559.
- Fan, Y., Oldenbeuving, R. M., Klein, E. J., Lee, C. J., Song, H., Khan, M. R., Boller, K.-J. (2014). *A hybrid semiconductor-glass waveguide laser*. Paper presented at the Laser Sources and Applications II.
- Fegadolli, W. S., Vargas, G., Wang, X., Valini, F., Barea, L. A., Oliveira, J. E., . . . Panepucci, R. R. (2012). Reconfigurable silicon thermo-optical ring resonator switch based on Vernier effect control. *Optics express*, 20(13), p.p. 14722-14733.
- Feuer, M. D., Huang, S.-Y., Woodward, S. L., Coskun, O., & Boroditsky, M. (2003). Electronic dispersion compensation for a 10-Gb/s link using a directly modulated laser. *IEEE Photonics Technology Letters*, 15(12), p.p. 1788-1790.

- Gallet, A., Shen, A., Levaufre, G., Girard, N., Make, D., Provost, J., Olivier, S. (2016). *50km Error Free Transmission at 10Gb/s with an Integrated Hybrid III-V on Silicon Directly Modulated DFB Laser and Ring Resonator*. Paper presented at the ECOC 2016; 42nd European Conference on Optical Communication; Proceedings of.
- Gang, S. (2005). Polymer based optical waveguides. *Master's degree thesis, Universiti Teknologi Malaysia, Johor Bahru Google Scholar*.
- Giuntoni, I., Stolarek, D., Gajda, A., Winzer, G., Bruns, J., Tillack, B., Zimmermann, L. (2010). *Integrated drop-filter for dispersion compensation based on SOI rib waveguides*. Paper presented at the Optical Fiber Communication (OFC), collocated National Fiber Optic Engineers Conference, 2010 Conference on (OFC/NFOEC).
- Gmachl, C., Capasso, F., Narimanov, E., Nöckel, J. U., Stone, A. D., Faist, J., Cho, A. Y. (1998). High-power directional emission from microlasers with chaotic resonators. *Science*, 280(5369), p.p. 1556-1564.
- Goykhman, I., Desiatov, B., & Levy, U. (2010). Ultrathin silicon nitride microring resonator for biophotonic applications at 970 nm wavelength. *Applied Physics Letters*, 97(8), 081108.
- Grover, R., Ibrahim, T., Kanakaraju, S., Lucas, L., Calhoun, L., & Ho, P.-T. (2004). A tunable GaInAsP-InP optical microring notch filter. *IEEE Photonics Technology Letters*, 16(2), p.p. 467-469.
- Haavisto, J., & Pajer, G. (1980). Resonance effects in low-loss ring waveguides. *Optics Letters*, 5(12), p.p. 510-512.
- Hah, D., & Bordelon, J. (2015). *Design of mechanically tunable optical filters with microring resonators*. Paper presented at the Design, Test, Integration and Packaging of MEMS/MOEMS (DTIP), 2015 Symposium on.
- Hah, D., Bordelon, J., & Zhang, D. (2011). Mechanically tunable optical filters with a microring resonator. *Applied Optics*, 50(22), p.p. 4320-4327.
- Henry, C. H., Kazarinov, R., Lee, H., Orlowsky, K., & Katz, L. (1987). Low loss Si₃N₄-SiO₂ optical waveguides on Si. *Applied Optics*, 26(13), p.p. 2621-2624.
- Hosseini, E. S., Yegnanarayanan, S., Atabaki, A. H., Soltani, M., & Adibi, A. (2009). High quality planar silicon nitride microdisk resonators for integrated photonics in the visiblewavelength range. *Optics express*, 17(17), p.p. 14543-14551.
- Ikeda, K., Saperstein, R. E., Alic, N., & Fainman, Y. (2008). Thermal and Kerr nonlinear properties of plasma-deposited silicon nitride/silicon dioxide waveguides. *Optics express*, 16(17), p.p. 12987-12994.

- Ishizaka, M., & Yamazaki, H. (2006). Wavelength tunable laser using silica double ring resonators. *Electronics and Communications in Japan (Part II: Electronics)*, 89(3), p.p. 34-41.
- Jeon, M., Kim, J., Song, J. W., Lee, H., Choi, S., & Nelson, J. S. (2008). Tunable ring laser based on a semiconductor optical amplifier at 1300 nm using a simple wavelength selection filter. *Microwave and optical technology letters*, 50(5), p.p. 1317-1320.
- Jiang, G., Chen, R., Zhou, Q., Yang, J., Wang, M., & Jiang, X. (2011). Slab-modulated sidewall Bragg gratings in silicon-on-insulator ridge waveguides. *IEEE Photonics Technology Letters*, 23(1), p.p. 6-8.
- Jiang, W. C., Lu, X., Zhang, J., & Lin, Q. (2012). High-frequency silicon optomechanical oscillator with an ultralow threshold. *Optics express*, 20(14), p.p. 15991-15996.
- Jiang, X., Lin, Q., Rosenberg, J., Vahala, K., & Painter, O. (2009). High-Q double-disk microcavities for cavity optomechanics. *Optics express*, 17(23), p.p. 20911-20919.
- Johnson, T. J., Borselli, M., & Painter, O. (2006). Self-induced optical modulation of the transmission through a high-Q silicon microdisk resonator. *Optics express*, 14(2), p.p. 817-831.
- Jones, A. M., DeRose, C. T., Lentine, A. L., Trotter, D. C., Starbuck, A. L., & Norwood, R. A. (2013). Ultra-low crosstalk, CMOS compatible waveguide crossings for densely integrated photonic interconnection networks. *Optics express*, 21(10), p.p. 12002-12013.
- Jugessur, A., Dou, J., Aitchison, J., De La Rue, R., & Gnan, M. (2009). A photonic nano-Bragg grating device integrated with microfluidic channels for bio-sensing applications. *Microelectronic Engineering*, 86(4-6), p.p. 1488-1490.
- Kawasaki, B. S., Hill, K. O., Johnson, D. C., & Fujii, Y. (1978). Narrow-band Bragg reflectors in optical fibers. *Optics Letters*, 3(2), p.p. 66-68.
- Kazovsky, L. G., Shaw, W.-T., Gutierrez, D., Cheng, N., & Wong, S.-W. (2007). Next-generation optical access networks. *Journal of lightwave technology*, 25(11), p.p. 3428-3442.
- Kita, T., Nemoto, K., & Yamada, H. (2014). Silicon photonic wavelength-tunable laser diode with asymmetric Mach-Zehnder interferometer. *IEEE Journal of Selected Topics in Quantum Electronics*, 20(4), p.p. 344-349.
- Kohtoku, M., Kominato, T., Nasu, Y., & Shibata, T. (2005). New waveguide fabrication techniques for next generation plcs. *NTT Technical Review*, 3(7), p.p. 37-41.

- Koonath, P., Indukuri, T., & Jalali, B. (2006). Monolithic 3-D silicon photonics. *Journal of lightwave technology*, 24(4), p.p. 1796-1804.
- Lam, D., & Garside, B. K. (1981). Characterization of single-mode optical fiber filters. *Applied Optics*, 20(3), p.p. 440-445.
- Lee, H. S., Choi, C.-H., Beom-Hoan, O., Park, D.-G., Kang, B.-G., Kim, S.-H., Lee, E.-H. (2004). A nonunitary transfer matrix method for practical analysis of racetrack microresonator waveguide. *IEEE Photonics Technology Letters*, 16(4), p.p. 1086-1088.
- Levi, A., Slusher, R., McCall, S., Tanbun-Ek, T., Coblentz, D., & Pearton, S. (1992). Room temperature operation of microdisc lasers with submilliamp threshold current. *Electronics letters*, 28(11), p.p. 1010-1012.
- Levy, J. S., Gondarenko, A., Foster, M. A., Turner-Foster, A. C., Gaeta, A. L., & Lipson, M. (2010). CMOS-compatible multiple-wavelength oscillator for on-chip optical interconnects. *Nature Photonics*, 4(1), 37.
- Li, G., Liu, P., Jiang, X., Yang, C., Ma, J., Wu, H., & Xiao, M. (2015). High-Q silica microdisk optical resonators with large wedge angles on a silicon chip. *Photonics Research*, 3(5), p.p. 279-282.
- Li, X., Wan, Y., Hu, T., Yu, P., Yu, H., Yang, J., & Jiang, X. (2015). A tunable silicon ring reflector. *Journal of optics*, 44(1), p.p. 26-29.
- Lim, A. E.-J., Song, J., Fang, Q., Li, C., Tu, X., Duan, N., . . . Liow, T.-Y. (2014). Review of silicon photonics foundry efforts. *IEEE Journal of Selected Topics in Quantum Electronics*, 20(4), p.p. 405-416.
- Liu, J., & Kobayashi, T. (2010). Generation and amplification of tunable multicolored femtosecond laser pulses by using cascaded four-wave mixing in transparent bulk media. *Sensors*, 10(5), p.p. 4296-4341.
- Liu, Y., Ingham, J. D., Plumb, D., Pentyl, R. V., White, I. H., Robbins, D. J., . . . Ward, A. J. (2006). *Directly-modulated DS-DBR tunable laser for uncooled C-band WDM system*. Paper presented at the Optical Fiber Communication Conference.
- Luke, K., Dutt, A., Poitras, C. B., & Lipson, M. (2013). Overcoming Si₃N₄ film stress limitations for high quality factor ring resonators. *Optics express*, 21(19), p.p. 22829-22833.
- Marpaung, D., Morrison, B., Pant, R., Roeloffzen, C., Leinse, A., Hoekman, M., . . . Eggleton, B. J. (2013). Si₃N₄ ring resonator-based microwave photonic notch filter with an ultrahigh peak rejection. *Optics express*, 21(20), p.p. 23286-23294.

- Mason, S. J. (1956). Feedback theory: Further properties of signal flow graphs.
- Matsui, Y., Mahgerefteh, D., Zheng, X., Liao, C., Fan, Z. F., McCallion, K., & Tayebati, P. (2006). Chirp-managed directly modulated laser (CML). *IEEE Photonics Technology Letters*, 18(2), p.p. 385-387.
- Matsumoto, T., Suzuki, A., Takahashi, M., Watanabe, S., Ishii, S., Suzuki, K., Sakuma, N. (2010). *Narrow spectral linewidth full band tunable laser based on waveguide ring resonators with low power consumption*. Paper presented at the Optical Fiber Communication Conference.
- Meindl, J. D. (2003). Beyond Moore's law: The interconnect era. *Computing in Science & Engineering*, 5(1), p.p. 20-24.
- Mizuhara, O., Nguyen, T., Tzeng, L., & Yeates, P. (1995). 10 Gbit/s transmission experiment using direct modulation and including 8: 1 time-division-multiplex setup. *Electronics letters*, 31(8), p.p. 660-662.
- Mokhtari, M. R., & Baghban, H. (2015). *Wireless network interconnect concept based on dielectric ring resonators*. Paper presented at the Information and Knowledge Technology (IKT), 2015 7th Conference on.
- Morand, A., Zhang, Y., Martin, B., Huy, K. P., Amans, D., Benech, P., . . . Fédéli, J.-M. (2006). Ultra-compact microdisk resonator filters on SOI substrate. *Optics express*, 14(26), p.p. 12814-12821.
- Morton, P., Tanbun-Ek, T., Logan, R., Ackerman, D., Shtengel, G., Chand, N., Sciortino Jr, P. (1996). *High-speed, low chirp, directly modulated 1.55- μ m DFB laser sources for 10 Gbit/s local distribution*. Paper presented at the Optical Fiber Communication Conference.
- Moss, D. J., Morandotti, R., Gaeta, A. L., & Lipson, M. (2013). New CMOS-compatible platforms based on silicon nitride and Hydex for nonlinear optics. *Nature Photonics*, 7(8), 597.
- Oldenbeuving, R., Klein, E., Offerhaus, H. L., Lee, C. J., Song, H., & Boller, K. J. (2012). 25 kHz narrow spectral bandwidth of a wavelength tunable diode laser with a short waveguide-based external cavity. *Laser physics letters*, 10(1), 015804.
- Painchaud, Y., Paquet, C., & Guy, M. (2007). Optical tunable dispersion compensators based on thermally tuned fiber Bragg gratings. *Optics and Photonics News*, 18(9), p.p. 48-53.
- Paloczi, G. T., Scheuer, J., & Yariv, A. (2005). Compact microring-based wavelength-selective inline optical reflector. *IEEE Photonics Technology Letters*, 17(2), p.p. 390-392.

- Paschotta, D. R. Chirp. Zürich, Switzerland: RP Photonics Encyclopedia.
- Piels, M., Bauters, J. F., Davenport, M. L., Heck, M. J., & Bowers, J. E. (2014). Low-loss silicon nitride AWG demultiplexer heterogeneously integrated with hybrid III-V/silicon photodetectors. *Journal of lightwave technology*, 32(4), p.p. 817-823.
- Poon, J. K., Scheuer, J., & Yariv, A. (2004). Wavelength-selective reflector based on a circular array of coupled microring resonators. *IEEE Photonics Technology Letters*, 16(5), p.p. 1331-1333.
- Popovic, M. A., Barwicz, T., Dahlem, M. S., Gan, F., Holzwarth, C. W., Rakich, P. T., Krtner, F. X. (2007). *Tunable, fourth-order silicon microring-resonator add-drop filters*. Paper presented at the Optical Communication (ECOC), 2007 33rd European Conference and Exhibition of.
- Rabus, D. G. (2007). *Integrated ring resonators*: Springer.
- Ren, M., Cai, H., Chin, L. K., Huang, J., Gu, Y., Radhakrishnan, K., Liu, A. Q. (2016). An opto-mechanical coupled-ring reflector driven by optical force for lasing wavelength control. *Applied Physics Letters*, 108(8), 081106.
- Rochette, M., Guy, M., LaRochelle, S., Lauzon, J., & Trepanier, F. (1999). Gain equalization of EDFA's with Bragg gratings. *IEEE Photonics Technology Letters*, 11(5), p.p. 536-538.
- Sacher, W. D., Huang, Y., Lo, G.-Q., & Poon, J. K. (2015). Multilayer silicon nitride-on-silicon integrated photonic platforms and devices. *Journal of lightwave technology*, 33(4), p.p. 901-910.
- Sato, K., Kobayashi, N., Namiwaka, M., Yamamoto, K., Watanabe, S., Kita, T., Yamazaki, H. (2015). *Demonstration of silicon photonic hybrid ring-filter external cavity wavelength tunable lasers*. Paper presented at the Optical Communication (ECOC), 2015 European Conference on.
- Schwelb, O. (2007). The nature of spurious mode suppression in extended FSR microring multiplexers. *Optics communications*, 271(2), p.p. 424-429.
- Selvaraja, S. K., Jaenen, P., Bogaerts, W., Van Thourhout, D., Dumon, P., & Baets, R. (2009). Fabrication of photonic wire and crystal circuits in silicon-on-insulator using 193-nm optical lithography. *Journal of lightwave technology*, 27(18), p.p. 4076-4083.
- Shi, W., Vafaei, R., Torres, M. A. G., Jaeger, N. A., & Chrostowski, L. (2010). *Ring-resonator reflector with a waveguide crossing*. Paper presented at the Optical MEMS and Nanophotonics (OPT MEMS), 2010 International Conference on.

- Shi, W., Yun, H., Zhang, W., Lin, C., Chang, T. K., Wang, Y., Chrostowski, L. (2012). Ultra-compact, high-Q silicon microdisk reflectors. *Optics express*, 20(20), p.p. 21840-21846.
- Shigehara, T. (1994). Conditions for the appearance of wave chaos in quantum singular systems with a pointlike scatterer. *Physical Review E*, 50(6), 4357.
- Sieber, M. (2007). Wavefunctions, Green functions and expectation values in terms of spectral determinants. *Nonlinearity*, 20(11), 2721.
- Sodagar, M., Pourabolghasem, R., Eftekhari, A. A., & Adibi, A. (2014). High-efficiency and wideband interlayer grating couplers in multilayer Si/SiO₂/SiN platform for 3D integration of optical functionalities. *Optics express*, 22(14), p.p. 16767-16777.
- Soltani, M., Li, Q., Yegnanarayanan, S., & Adibi, A. (2010). Toward ultimate miniaturization of high Q silicon traveling-wave microresonators. *Optics express*, 18(19), p.p. 19541-19557.
- Soltani, M., Yegnanarayanan, S., & Adibi, A. (2007). Ultra-high Q planar silicon microdisk resonators for chip-scale silicon photonics. *Optics express*, 15(8), p.p. 4694-4704.
- Soref, R. (2006). The past, present, and future of silicon photonics. *IEEE Journal of Selected Topics in Quantum Electronics*, 12(6), p.p. 1678-1687.
- Spencer, D. T., Bauters, J. F., Heck, M. J., & Bowers, J. E. (2014). Integrated waveguide coupled Si₃N₄ resonators in the ultrahigh-Q regime. *Optica*, 1(3), p.p. 153-157.
- Srinivasan, K., Borselli, M., Johnson, T. J., Barclay, P. E., Painter, O., Stintz, A., & Krishna, S. (2005). Optical loss and lasing characteristics of high-quality-factor AlGaAs microdisk resonators with embedded quantum dots. *Applied Physics Letters*, 86(15), 151106.
- Stutius, W., & Streifer, W. (1977). Silicon nitride films on silicon for optical waveguides. *Applied Optics*, 16(12), p.p. 3218-3222.
- Sun, H., Chen, A., & Dalton, L. R. (2009). A reflective microring notch filter and sensor. *Optics express*, 17(13), p.p. 10731-10737.
- Sun, X., Zhang, X., & Tang, H. X. (2012). High-Q silicon optomechanical microdisk resonators at gigahertz frequencies. *Applied Physics Letters*, 100(17), 173116.
- Tien, M.-C., Bauters, J. F., Heck, M. J., Spencer, D. T., Blumenthal, D. J., & Bowers, J. E. (2011). Ultra-high quality factor planar Si₃N₄ ring resonators on Si substrates. *Optics express*, 19(14), p.p. 13551-13556.

- Tietgen, K. (1984). *Tunable integrated optical ring resonator*. Paper presented at the Topical Meeting Integrated Guided Wave Optics.
- Timotijevic, B., Mashanovich, G., Michaeli, A., Cohen, O., Passaro, V., Crnjanski, J., & Reed, G. (2009). Tailoring the spectral response of add/drop single and multiple resonators in silicon-on-insulator. *Chinese Optics Letters*, 7(4), p.p. 291-295.
- Van, V. (2007). Dual-mode microring reflection filters. *Journal of lightwave technology*, 25(10), p.p. 142-3150.
- Vargas, S., & Vazquez, C. (2014). Optical reconfigurable demultiplexer based on Bragg grating assisted ring resonators. *Optics express*, 22(16), p.p. 19156-19168.
- Wakaba, M., Iwai, N., Kiyota, K., Hasegawa, H., Kurobe, T., Kobayashi, G., Yokouchi, N. (2013). *High power operation at high temperature of AlGaInAs/InP widely tunable BH laser*. Paper presented at the OptoElectronics and Communications Conference and Photonics in Switching.
- Wang, C., & Yao, J. (2013). Fiber Bragg gratings for microwave photonics subsystems. *Optics express*, 21(19), p.p. 22868-22884.
- Wang, W., Zhang, A., Yang, K., Huang, Z., Feng, S., & Wang, Y. (2012). *Ultrapact SOI Microring Add-Drop Filter with Extra-Wide FSR for Silicon Photonic Application*. Paper presented at the Photonics and Optoelectronics (SOPO), 2012 Symposium on.
- Wang, X., Shi, W., Yun, H., Grist, S., Jaeger, N. A., & Chrostowski, L. (2012). Narrow-band waveguide Bragg gratings on SOI wafers with CMOS-compatible fabrication process. *Optics express*, 20(14), p.p. 15547-15558.
- Weber, H., & Ulrich, R. (1971). A Thin-Film Ring Laser. *Applied Physics Letters*, 19(2), p.p. 38-40.
- Wedding, B. (1992). New method for optical transmission beyond dispersion limit. *Electronics letters*, 28(14), p.p. 1298-1300.
- Wiersig, J., & Hentschel, M. (2006). Unidirectional light emission from high-Q modes in optical microcavities. *Physical Review A*, 73(3), 031802.
- Xia, F., Rooks, M., Sekaric, L., & Vlasov, Y. (2007). Ultra-compact high order ring resonator filters using submicron silicon photonic wires for on-chip optical interconnects. *Optics express*, 15(19), p.p. 11934-11941.
- Xu, Q., Schmidt, B., Pradhan, S., & Lipson, M. (2005). Micrometre-scale silicon electro-optic modulator. *nature*, 435(7040), 325.

- Yang, Y.-D., Li, Y., Huang, Y.-Z., & Poon, A. W. (2014). Silicon nitride three-mode division multiplexing and wavelength-division multiplexing using asymmetrical directional couplers and microring resonators. *Optics express*, 22(18), p.p. 22172-22183.
- Yariv, A. (2000). Universal relations for coupling of optical power between microresonators and dielectric waveguides. *Electronics letters*, 36(4), p.p. 321-322.
- Ymeti, A., Kanger, J. S., Greve, J., Besselink, G., Lambeck, P., Wijn, R., & Heideman, R. (2005). Integration of microfluidics with a four-channel integrated optical Young interferometer immunosensor. *Biosensors and Bioelectronics*, 20(7), p.p. 1417-1421.
- Yoffe, G., Nguyen, T., Heanue, J., & Pezeshki, B. (2012). *Efficient compact tunable laser for access networks using silicon ring resonators*. Paper presented at the Optical Fiber Communication Conference and Exposition (OFC/NFOEC), 2012 and the National Fiber Optic Engineers Conference.
- Yurtsever, G., Považay, B., Alex, A., Zabihian, B., Drexler, W., & Baets, R. (2014). Photonic integrated Mach-Zehnder interferometer with an on-chip reference arm for optical coherence tomography. *Biomedical optics express*, 5(4), p.p. 1050-1061.
- Zhang, Y., Yang, S., Lim, A. E.-J., Lo, G.-Q., Galland, C., Baehr-Jones, T., & Hochberg, M. (2013). A compact and low loss Y-junction for submicron silicon waveguide. *Optics express*, 21(1), p.p. 1310-1316.
- Zhou, L., & Poon, A. W. (2006). Silicon electro-optic modulators using pin diodes embedded 10-micron-diameter microdisk resonators. *Optics express*, 14(15), p.p. 6851-6857.
- Zorbas, J. (1980). Perturbation of self-adjoint operators by Dirac distributions. *Journal of Mathematical Physics*, 21(4), p.p. 840-847.